ABSTRACT

Title of Dissertation: TOWARD *IN SITU* MEASUREMENT OF LIQUID DENSITY USING OPTICAL KERR EFFECT SPECTROSCOPY

John S. Bender, Doctor of Philosophy, 2016

Dissertation directed by: Professor John T. Fourkas, Department of Chemistry and Biochemistry

Optical Kerr effect (OKE) spectroscopy is a widely used technique for probing the low-frequency, Raman-active dynamics of liquids. Although molecular simulations are an attractive tool for assigning liquid degrees of freedom to OKE spectra, the accurate modeling of the OKE and the motions that contribute to it rely on the use of a realistic and computationally tractable molecular polarizability model. Here we explore how the OKE spectrum of liquid benzene, and the underlying dynamics that determines its shape, are affected by the polarizability model employed. We test a molecular polarizability model that uses a point anisotropic molecular polarizability and three others that distribute the polarizability over the molecule. The simplest and most computationally efficient distributed polarizability model tested is found to be sufficient for the accurate simulation of the liquid polarizability dynamics.

The high-frequency portion of the OKE spectrum of benzene shifts to higher frequency with decreasing temperature at constant pressure. Molecular dynamics simulations of benzene are used to isolate the effects of temperature and density on the spectrum. The simulations show that, at constant density, the high-frequency portion of the spectrum shifts to lower frequency with decreasing temperature. In contrast, at constant temperature, the high-frequency portion of the spectrum shifts to higher frequency with increasing density. Line shape analyses of simulated spectra under isochoric and isothermal conditions shows that the effects of density and temperature are separable, suggesting that OKE spectroscopy is a viable technique for *in situ* measurement of the density of van der Waals liquids.

OKE spectroscopy is then used to investigate the density of benzene confined in nanoporous silica. The high-frequency portion of the OKE spectrum shifts to the blue with increasing confinement, which is consistent with densification. Molecular dynamics simulations show that the tumbling vibrational density of states of benzene confined in silica pores exhibit behavior similar to that of the OKE spectrum. The dependence of the structure of the simulated liquid with increasing confinement resembles that of the bulk liquid at constant temperature and increasing density, further supporting the premise that benzene is densified upon confinement in silica pores.

TOWARD *IN SITU* MEASUREMENT OF LIQUID DENSITY USING OPTICAL KERR EFFECT SPECTROSCOPY

by

John S. Bender

Dissertation submitted to the Faculty of the Graduate School of the
University of Maryland, College Park, in partial fulfillment
of the requirements for the degree of
Doctor of Philosophy
2016

Advisory Committee:
Professor John T. Fourkas, Chair
Professor Amy S. Mullin
Professor John D. Weeks
Professor Millard H. Alexander
Professor Mikhail A. Anisimov

Dedication

Dedicated to Hillary, Joshua, and Annabelle.

Acknowledgements

Several people have had a hand in producing the work contained in this thesis in one way or another. I would like to take the time to thank each of them in the next few paragraphs.

First, I would like to extend my deepest gratitude to my advisor, Prof. John T. Fourkas. John is the most diligent person I have ever worked with. Obviously, he is the genesis of the work that is conducted in the Fourkas Lab, but he encourages independent thought and is extremely receptive to his student's ideas. His understanding of chemistry and physics seems to be endless, and he is extremely patient when he is sharing his knowledge. Throughout my career at the University of Maryland, John has been most supportive, and I am more than happy to have been a member of his research group.

Second, I would like to thank my committee: Prof. Millard H. Alexander, Prof. Amy S. Mullin, Prof. John D. Weeks, and Prof. Mikhail A. Anisimov. I have a deep appreciation for the classes I've taken from them and the recommendations they've made on my behalf. I also cannot thank them enough for taking their time to read and comment on this thesis.

Third, I would like to thank Dr. Benoit Coasne. At times, Ben has been like a second advisor. He provided me with the tools to conduct molecular dynamics simulations, both conceptually and physically. His expertise in the simulation of liquids has been the source of refining the simulation work in this thesis.

Fourth, Dr. Chris A. Rivera was indispensible in molding my graduate career. Chris taught me to be meticulous and detail oriented in conducting experiments. He

helped me through several tumultuous periods when I was dealing with instrumental difficulties. He turned out to be a great friend as well, and I feel lucky to have met him.

Fifth, I would like to thank the members of the Fourkas Group, past and present, who have helped me throughout my time at the University of Maryland. Dr. Xiaoxiao He introduced me to the experimental methods we use to study liquids. She was someone I could freely discuss ideas with and was extremely helpful to me in the first few years of my graduate studies. Dr. Nikolaos Liaros has been a pleasure to work with, and his expertise in nonlinear spectroscopy is always well received. Samuel R. Cohen has been a great partner in my experimental work. Sam is an incredibly intelligent person, and I have no doubt he will be extremely successful in the study of liquids. To all of the other members of the Fourkas Group, I thank you from the bottom of my heart for being so easy to work with and providing me with a stimulating research environment.

Finally, I would like to extend my deepest gratitude to my family. My wife, Hillary, has been the most supportive person in my life. I will never be able to repay her for the help she has given me throughout our time together. Our children, Josh and Annabelle, are simultaneously the most challenging and most rewarding aspects of my life. Graduate school can become troublesome at times, and Josh and Annabelle have been instrumental in helping me put these troubles into perspective.

A great portion of the work presented here was funded through my National Science Foundation Graduate Research Fellowship.

Table of Contents

List of Tables

List of Figures

List of Abbreviations

AG	Antisymmetrized Gaussian
AMPT	Atomic-to-Molecular Polarizability Transformation
BL	Bucaro-Litovitz
CI	Collision-induced
CM	Collective Molecular
CMC	Canonical Monte Carlo
CMII	Collective Molecular/Interaction-induced
CPU	Central Processing Unit
DID	Dipole/Induced Dipole
DLS	Depolarized Light Scattering
GCMC	Grand Canonical Monte Carlo
IAD	Interacting Anisotropic Distributed
II	Interaction-induced
IID	Interacting Isotropic Distributed
KDP	Potassium Dihydrogen Phosphate
MD	Molecular Dynamics
NID	Non-interacting Distributed
NVE	Microcanonical Ensemble
NVT	Canonical Ensemble
OHD	Optically-Heterodyne-Detected
OKE	Optical Kerr Effect
PAP	Point Anisotropic Polarizability

R	Reorientational
RCI	Reorientational/Collision-induced
RSD	Reduced Spectral Density
SANS	Small Angle Neutron Scattering
TCF	Time Correlation Function
TEOS	Tetraethyl Orthosilicate
VDOS	Vibrational Density of States

Chapter 1: Introduction

1.1 *Motivation and Background*

The dynamics and structure of liquids are major areas of study throughout the fields of chemistry, physics, biology, materials sciences, and geological sciences. The microscopic properties of a liquid determine its macroscopic properties. The macroscopic property that this thesis addresses is the density of a liquid. Specifically, the work presented is focused on using experiments and molecular dynamics (MD) simulations to determine whether optical Kerr effect (OKE) spectroscopy[1-4] can be used to measure the density of a liquid noninvasively by relating the microscopic intermolecular dynamics encoded in the OKE spectrum to the thermodynamic state of the liquid. Although this technique is not likely to replace the traditional methods of measuring liquid density in bulk samples, it will provide access to thermodynamic states that are inherently difficult to study using those methods.

OKE spectroscopy has been used to study a multitude of liquid systems, including simple,[5] confined,[6] ionic,[7-9] supercooled,[10-13] and nematic liquids.[14,15] This technique, which provides a broad range of information on the rotational diffusive, intramolecular, and intermolecular dynamics of liquids, owes its popularity to its ease of implementation and the quality of data it provides. OKE spectroscopy is a pump/probe spectroscopy in which the time dependence of induced birefringence in a liquid is monitored. The resulting birefringence decay can be analyzed directly to measure the orientational correlation time (which is typically a few picoseconds or more) for a liquid, which can

provide information on molecular shape and the degree of molecular ordering within a liquid. The intramolecular and intermolecular dynamics are considerably more complex and occur on a timescale of a few picoseconds. These dynamics are often best represented in the frequency domain. McMorrow and Lotshaw[16,17] provided a framework for transforming the time-domain OKE birefringence decay into the frequency domain. The resulting spectral density is equivalent to the Bose-Einstein-corrected, low-frequency, depolarized Raman spectrum. It is common to remove the rotational diffusion dynamics from the birefringence decay during the transformation process, resulting in what is known as the reduced spectral density (RSD), which is encoded with the intermolecular dynamics of the liquid.

OKE spectroscopy provides a wealth of information pertaining to the molecular dynamics of a liquid. However, interpretation of the intermolecular contributions to the OKE RSD is difficult. The difficulty lies in the overlapping nature of the response functions that give rise to the spectrum. As of yet, there is no experimentally approachable method to separate these responses. However, MD simulations offer the opportunity to probe the separate contributions to the OKE spectrum, giving insight into the interpretation of experimental data. Calculation of the RSD depends on the many-body polarizability, which depends on intermolecular distances in the liquid in question. Therefore, the OKE spectrum and its individual polarizability contributions can be calculated with relative ease from MD simulation trajectories. Additionally, MD simulations offer complete control over the thermodynamic state of the system. For example, the density of a liquid can be easily controlled independently of the temperature, allowing the effects of temperature and density to be separated in the OKE

spectrum. MD simulations of OKE spectroscopy have been used to investigate a variety of systems, including simple liquids,[18-22] binary mixtures,[23] confined liquids,[24] and ionic liquids.[7,9]

The molecular polarizability model employed to calculate the OKE response functions and spectra has a significant impact on their resultant accuracy.[20,21,25-28] Traditionally, a point molecular polarizability model (in which the molecular polarizability is placed at the center of mass of the molecule) is employed.[21,22,29,30] Alternatively, a distributed molecular polarizability can be used in which the molecular polarizability is spread about the molecule, usually at atomic sites.[18,23,28,31,32] The impact that each of these models has on the many-body polarizability is a rich area of study, and distributed models have been shown to be more accurate in calculating OKE spectra.[28,31,32] Although a distributed polarizability model seems to be more realistic, the degree to which the model needs to be spread across the molecule to calculate the OKE spectrum accurately is still not completely understood. In Chapter 4, I use four different models of the polarizability of benzene to calculate its OKE RSD.[31] The models represent four different distributions of the polarizability. I also explore the necessity of intramolecular interactions and their impact on the accuracy of the calculated spectrum. The molecular polarizability depends on the model of the interactions between the polarizability sites. The interaction between two polarizability sites is normally modeled within the dipole/induced dipole (DID) approximation.[33] It is well known that within the DID model, as two point polarizabilities approach each other at short distances, the polarizability calculated with this interaction tensor can become unrealistically large.[20,34] Approaches have been developed to amend the interaction tensor to alleviate this

problem.[34-36] Thole introduced a model that spreads the interaction tensor out in space based on an assumed charge distribution.[34,35] Birge *et al.* took the Thole model a step further by modeling the charge distribution based on molecular orbital shapes. Both of these approaches have been shown to reproduce the molecular polarizability accurately. I have adopted the approach of Thole in developing two of the models of benzene investigated here, and I benchmark the accuracy of the spectra calculated using these models in Chapter 4.

OKE spectroscopy has also been used to investigate the intermolecular dynamics of liquids as a function of thermodynamic variables.[8,10,11,15,37-42] For example, in simple liquids, the high-frequency edge of the OKE RSD shifts to the blue when the liquid being investigated is cooled. This phenomenon is a result of the stiffening of the intermolecular potential as the density of the liquid increases.[39,43-46] As the potential stiffens, the librational frequencies in the liquid increase, resulting in the shift to higher frequency. However, a decreased temperature will decrease the accessibility of the librational motions associated with the higher energy states in the intermolecular potential. Therefore, temperature and density exert opposing effects on the high-frequency components of the OKE RSD.[47]

The effects of temperature and density on low-frequency Raman spectra have been investigated using experiment[40,48-50] and simulation.[26,40,51] These studies have shown that density indeed affects the high-frequency components of the low-frequency Raman spectrum to a greater extent than does temperature. In principle, it should be possible to calibrate the OKE RSD to measure the density of a liquid given a constant pressure. In Chapter 5, I use OKE spectroscopy and MD simulations to show that this idea is indeed

possible. Using benzene as a representative system, we show that the high-frequency components of the experimental spectra and simulated spectra shift in a nearly identical fashion as a function of both density and temperature, demonstrating the comparability of the experimental and simulated data. For benzene, these components are dominated by librational dynamics.[22,31,52] Additionally, using popular empirical fitting functions,[8,39,45,52-56] we demonstrate that the effects of temperature and density are separable in the high-frequency components of the OKE RSD.

OKE spectroscopy has been used previously to study the dynamics of liquids confined in nanoporous silica sol-gels.[38,57-61] Confinement on length scales comparable to the size of a molecule has pronounced effects on the molecular dynamics of liquids.[62-66] OKE experiments have shown that the orientational dynamics of simple liquids become heterogeneous upon confinement at the molecular scale. These experiments have also shown that the diffusive dynamics are also slowed relative to those in the bulk.

In addition to the dynamics of confined liquids, an active area of research is focused on determining the density of these systems.[67-71] There is only one experimental method available to determine the density of a confined liquid. Small-angle neutron scattering (SANS) measurements can be used for the indirect determination of the density of a liquid by monitoring the neutron scattering properties of the confining matrix before and after impregnation with the liquid to be studied.[69] Based on the results in Chapter 5,[47] I use OKE spectroscopy to determine the density of benzene confined in nanoporous silica in Chapter 6. I show that high-frequency components of the OKE RSD shift to higher frequency with increasing confinement, and that this behavior is consistent with densification. Using MD simulations of confined benzene, I show that the vibrational

density of states (VDOS) for molecular tumbling exhibits comparable behavior with increasing confinement. These data are used to estimate the density of the confined liquid, which increases with increasing pore curvature.

To extract information from OKE RSDs, the spectra are often fit to empirical functions. The so-called Bucaro-Litovitz[72] (BL) function is often used to fit the low-frequency side of the spectrum. This function was developed to fit the spectra for monatomic fluids. The antisymmetrized Gaussian[73] (AG) function is often used to fit the high-frequency side of the RSD. In van der Waals liquids, the AG function is usually used to describe librational character. The dilemma with these empirical fits is that they are not unique,[74] and the parameters extracted from them can become unrealistic due to the interplay between the two functions. In Chapter 7, I compare the individual components of the functions with the polarizability contributions of the simulated spectrum for benzene. Based on this comparison, I propose the physically-based constraint of the amplitude of the AG function. The constraint of this parameter is then shown to provide the expected behavior for the temperature evolution of the RSD for two simple liquids.

1.2 *Outline*

This thesis sets out to determine if OKE spectroscopy can be developed to measure the density of liquids. The OKE RSD is known to depend on the temperature and density of the liquid being studied, but it is unclear the relative effect that each of these thermodynamic variables has on the spectrum. MD simulations are performed in tandem with experiment to explore the possibility of using OKE spectroscopy as a method for *in situ* measurement of liquid density. In addition to this main objective, the

local structure of the liquid being studied is connected with its RSD and its underlying polarizability components. The density of a confined liquid is investigated using OKE spectroscopy. Liquid benzene was used as a representative simple liquid. The outline of the thesis is as follows:

- Chapter 2: The theory of optical Kerr effect spectroscopy is described for both simulations and experiment.
- Chapter 3: The OHD-OKE spectrometer is described.
- Chapter 4: Polarizability models are assessed for the accurate calculation of the OKE RSD for benzene. Four polarizability models are investigated. The simplest of three distributed polarizability models is found to accurately capture the polarizability dynamics of liquid benzene. The atomic-to-molecular polarizability transformation approxitmation [Hu et al. *J. Phys. Chem. B* **2008**, 112, 7837−7849.] is benchmarked for each of these polarizability models, and it shows a significant impact on the speed of computation of the liquid polarizability.
- Chapter 5: The relative effects of temperature and density on the OKE RSD for benzene are investigated. MD simulations are used to isolate these effects, and it is shown that density has a greater impact on the high-frequency components than does temperature. Temperature-dependent OKE experiments show that the high-frequency edge of the RSD shifts in a manner that is nearly identical to the simulated spectrum. Empirical fits to the simulated OKE RSDs show that the effects of temperature and density are separable in the extracted fit parameters.
- Chapter 6: The density of benzene confined in nanoporous silica sol-gels is investigated using OKE spectroscopy and MD simulations. The high-frequency

components of the OKE RSD shift to the blue upon confinement. This shift is consistent with densification. The VDOS from molecular tumbling calculated from MD trajectories exhibit similar behavior to the experimental spectra. The structure of the simulated confined liquid is shown to be consistent with densification.

- Chapter 7: The Bucaro-Litovitz and antisymmetrized Gaussian functions are compared to the polarizability components of the simulated spectrum of benzene. Based on these comparisons, the amplitude of the antisymmetrized Gaussian function is constrained when fitting temperature dependent RSDs for 1,3,5-trifluorobenzene and hexafluorobenzene. The constrained fits show trends in the extracted parameters that adhere to expectation, contrary to a previous study.
- Chapter 8: Conclusions and Future Work

1.3 *References*

(1) Fayer, M. D. *Ultrafast Infrared and Raman Spectroscopy*; Marcel Dekker: New York, NY, 2001; Vol. 26.

(2) Righini, R. Ultrafast Optical Kerr-Effect in Liquids and Solids. *Science* **1993**, *262*, 1386-1390.

(3) Smith, N. A.; Meech, S. R. Optically-Heterodyne-Detected Optical Kerr Effect (OHD-OKE): Applications in Condensed Phase Dynamics. *Int. Rev. Phys. Chem.* **2002**, *21*, 75-100.

(4) Kinoshita, S.; Kai, Y.; Ariyoshi, T.; Shimada, Y. Low Frequency Modes Probed by Time-Domain Optical Kerr Effect Spectroscopy. *Int. J. Mod Phys B* **1996**, *10*, 1229-1272.

(5) Zhong, Q.; Fourkas, J. T. Optical Kerr Effect Spectroscopy of Simple Liquids. *J. Phys. Chem. B* **2008**, *112*, 15529-15539.

(6) Farrer, R. A.; Fourkas, J. T. Orientational Dynamics of Liquids Confined in Nanoporous Sol-Gel Glasses Studied by Optical Kerr Effect Spectroscopy. *Acc. Chem. Res.* **2003**, *36*, 605-612.

(7) Bardak, F.; Xiao, D.; Hines, L. G.; Son, P.; Bartsch, R. A.; Quitevis, E. L.; Yang, P.; Voth, G. A. Nanostructural Organization in Acetonitrile/Ionic Liquid Mixtures: Molecular Dynamics Simulations and Optical Kerr Effect Spectroscopy. *Chemphyschem* **2012**, *13*, 1687-1700.

(8) Xiao, D.; Rajian, J. R.; Cady, A.; Li, S.; Bartsch, R. A.; Quitevis, E. L. Nanostructural Organization and Anion Effects on the Temperature Dependence of the Optical Kerr Effect Spectra of Ionic Liquids. *J. Phys. Chem. B* **2007**, *111*, 4669-4677.

(9) Yang, P.; Voth, G. A.; Xiao, D.; Hines, L. G.; Bartsch, R. A.; Quitevis, E. L. Nanostructural Organization in Carbon Disulfide/Ionic Liquid Mixtures: Molecular Dynamics Simulations and Optical Kerr Effect Spectroscopy. *J. Chem. Phys.* **2011**, *135*.

(10) Ricci, M.; Wiebel, S.; Bartolini, P.; Taschin, A.; Torre, R. Time-Resolved Optical Kerr Effect Experiments on Supercooled Benzene and Test of Mode-Coupling Theory. *Philos. Mag.* **2004**, *84*, 1491-1498.

(11) Taschin, A.; Bartolini, P.; Eramo, R.; Righini, R.; Torre, R. Evidence of Two Distinct Local Structures of Water from Ambient to Supercooled Conditions. *Nat. Commun.* **2013**, *4*, 2401.

(12) Cang, H.; Novikov, V. N.; Fayer, M. D. Logarithmic Decay of the Orientational Correlation Function in Supercooled Liquids on the Ps to Ns Time Scale. *J. Chem. Phys.* **2003**, *118*, 2800-2807.

(13) Hinze, G.; Brace, D. D.; Gottke, S. D.; Fayer, M. D. A Detailed Test of Mode-Coupling Theory on all Time Scales: Time Domain Studies of Structural Relaxation in a Supercooled Liquid. *J. Chem. Phys.* **2000**, *113*, 3723-3733.

(14) Cang, H.; Li, J.; Fayer, M. D. Short Time Dynamics in the Isotropic Phase of Liquid Crystals: The Aspect Ratio and the Power Law Decay. *Chem. Phys. Lett.* **2002**, *366*, 82-87.

(15) Sokolowsky, K. P.; Bailey, H. E.; Fayer, M. D. Length Scales and Structural Dynamics in Nematogen Pseudonematic Domains Measured with 2D IR Vibrational Echoes and Optical Kerr Effect Experiments. *J. Phys. Chem. B* **2014**, *118*, 7856-7868.

(16) McMorrow, D.; Lotshaw, W. T. The Frequency Response of Condensed-Phase Media to Femtosecond Optical Pulses: Spectral-Filter Effects. *Chem. Phys. Lett.* **1990**, *174*, 85-94.

(17) McMorrow, D.; Lotshaw, W. T. Intermolecular Dynamics in Acetonitrile Probed with Femtosecond Fourier-Transform Raman-Spectroscopy. *J. Phys. Chem.* **1991**, *95*, 10395-10406.

(18) Elola, M. D.; Ladanyi, B. M. Molecular Dynamics Study of Polarizability Anisotropy Relaxation in Aromatic Liquids and Its Connection with Local Structure. *J. Phys. Chem. B* **2006**, *110*, 15525-15541.

(19) Geiger, L. C.; Ladanyi, B. M. Higher-Order Interaction-Induced Effects on Rayleigh Light-Scattering by Molecular Liquids. *J. Chem. Phys.* **1987**, *87*, 191-202.

(20) Paolantoni, M.; Ladanyi, B. M. Polarizability Anisotropy Relaxation in Liquid Ethanol: A Molecular Dynamics Study. *J. Chem. Phys.* **2002**, *117*, 3856-3873.

(21) Geiger, L. C.; Ladanyi, B. M. Molecular-Dynamics Simulation Study of Nonlinear Optical-Response of Fluids. *Chem. Phys. Lett.* **1989**, *159*, 413-420.

(22) Ryu, S.; Stratt, R. M. A Case Study in the Nolecular Interpretation of Optical Kerr Effect Spectra: Instantaneous-Normal-Mode Analysis of the OKE Spectrum of Liquid Benzene. *J. Phys. Chem. B* **2004**, *108*, 6782-6795.

(23) Elola, M. D.; Ladanyi, B. M.; Scodinu, A.; Loughnane, B. J.; Fourkas, J. T. Effects of Molecular Association on Polarizability Relaxation in Liquid Mixtures of Benzene and Hexafluorobenzene. *J. Phys. Chem. B* **2005**, *109*, 24085-24099.

(24) Milischuk, A. A.; Ladanyi, B. M. Polarizability Anisotropy Relaxation in Nanoconfinement: Molecular Simulation Study of Acetonitrile in Silica Pores. *J. Phys. Chem. B* **2013**, *117*, 15729-15740.

(25) Elola, M. D.; Ladanyi, B. M. Polarizability Response in Polar Solvents: Molecular-Dynamics Simulations of Acetonitrile and Chloroform. *J. Chem. Phys.* **2005**, *122*, 224506.

(26) Ladanyi, B. M. Molecular-Dynamics Study of Rayleigh Light-Scattering from Molecular Fluids. *J. Chem. Phys.* **1983**, *78*, 2189-2203.

(27) Ladanyi, B. M.; Liang, Y. Q. Interaction-Induced Contributions to Polarizability Anisotropy Relaxation in Polar Liquids. *J. Chem. Phys.* **1995**, *103*, 6325-6332.

(28) Murry, R. L.; Fourkas, J. T.; Keyes, T. Nonresonant Intermolecular Spectroscopy Beyond the Placzek Approximation. I. Third-Order Spectroscopy. *J. Chem. Phys.* **1998**, *109*, 2814-2825.

(29) Tao, G. H.; Stratt, R. M. Why Does the Intermolecular Dynamics of Liquid Biphenyl So Closely Resemble that of Liquid Benzene? - Molecular Dynamics Simulation of the Optical-Kerr-Effect Spectra. *J. Phys. Chem. B* **2006**, *110*, 976-987.

(30) Frenkel, D.; Mctague, J. P. Molecular-Dynamics Studies of Orientational and Collision-Induced Light-Scattering in Molecular Fluids. *J. Chem. Phys.* **1980**, *72*, 2801-2818.

(31) Bender, J. S.; Coasne, B.; Fourkas, J. T. Assessing Polarizability Models for the Simulation of Low-Frequency Raman Spectra of Benzene. *J. Phys. Chem. B* **2015**, *119*, 9345-9358.

(32) Ladanyi, B. M.; Levinger, N. Molecular-Dynamics Study of Light-Scattering from Molecular Fluids. *Abstr. Pap. Am. Chem. S.* **1983**, *185*, 110-Phys.

(33) Applequist, J.; Carl, J. R.; Fung, K.-K. Atom Dipole Interaction Model for Molecular Polarizability. Application to Polyatomic Molecules and Determination of Atom Polarizabilities. *J. Am. Chem. Soc.* **1972**, *94*, 2952-2960.

(34) Thole, B. T. Molecular Polarizabilities Calculated with a Modified Dipole Interaction. *Chem. Phys.* **1981**, *59*, 341-350.

(35) van Duijnen, P. T.; Swart, M. Molecular and Atomic Polarizabilities: Thole's Model Revisited. *J. Phys. Chem. A* **1998**, *102*, 2399-2407.

(36) Birge, R. R.; Schick, G. A.; Bocian, D. F. Calculation of Molecular Polarizabilities Using a Semiclassical Slater-Type Orbital-Point Dipole Interaction (STOPDI) Model. *J. Chem. Phys.* **1983**, *79*, 2256-2264.

(37) Winkler, K.; Lindner, J.; Bürsing, H.; Vöhringer, P. Ultrafast Raman-Induced Kerr-Effect of Water: Single Molecule Versus Collective Motions. *J. Chem. Phys.* **2000**, *113*, 4674-4682.

(38) Loughnane, B. J.; Scodinu, A.; Fourkas, J. T. Temperature-Dependent Optical Kerr Effect Spectroscopy of Chloroform in Restricted Geometries. *Chem. Phys.* **2000**, *253*, 323-330.

(39) Loughnane, B. J.; Scodinu, A.; Fourkas, J. T. Temperature-Dependent Optical Kerr Effect Spectroscopy of Aromatic Liquids. *J. Phys. Chem. B* **2006**, *110*, 5708-5720.

(40) Kohler, B.; Nelson, K. A. Femtosecond Impulsive Stimulated Light Scattering from Liquid Carbon Disulfide at High Pressure: Experiment and Computer Simulation. *J. Phys. Chem.* **1992**, *96*, 6532-6538.

(41) Ishizumi, A.; Kasami, M.; Mishina, T.; Yamamoto, S.; Nakahara, J. Optical Kerr Effect in Carbon Disulfide Under High Pressure. *High Pressure Res.* **2003**, *23*, 201-204.

(42) Ishizumi, A.; Yamamoto, S.; Nakahara, J. Pressure Dependence of Low-Frequency Light Scattering in Carbon Disulfide. *J. Lumin.* **2001**, *94–95*, 687-690.

(43) Ruhman, S.; Kohler, B.; Joly, A. G.; Nelson, K. A. Intermolecular Vibrational Motion in CS_2 Liquid at $165 \leqslant T \geqslant 300$ K Observed by Femtosecond Time-Resolved Impulsive Stimulated Scattering. *Chem. Phys. Lett.* **1987**, *141*, 16-24.

(44) Farrer, R. A.; Loughnane, B. J.; Deschenes, L. A.; Fourkas, J. T. Level-Dependent Damping in Intermolecular Vibrations: Linear Spectroscopy. *J. Chem. Phys.* **1997**, *106*, 6901-6915.

(45) Ricci, M.; Bartolini, P.; Chelli, R.; Cardini, G.; Califano, S.; Righini, R. The Fast Dynamics of Benzene in the Liquid Phase - Part I. Optical Kerr Effect Experimental Investigation. *Phys. Chem. Chem. Phys.* **2001**, *3*, 2795-2802.

(46) Smith, N. A.; Meech, S. R. Ultrafast Dynamics of Polar Monosubstituted Benzene Liquids Studied by the Femtosecond Optical Kerr Effect. *J. Phys. Chem. A* **2000**, *104*, 4223-4235.

(47) Bender, J. S.; Cohen, S. R.; He, X.; Fourkas, J. T.; Coasne, B. Toward in Situ Measurement of the Density of Liquid Benzene Using Optical Kerr Effect Spectroscopy. *J. Phys. Chem. B* **2016**, *120*, 9103-9114.

(48) Hegemann, B.; Baker, K.; Jonas, J. Temperature and Density Effects on the Collision-Induced Depolarized Rayleigh Line-Shapes of Liquid Carbon-Disulfide. *J. Chem. Phys.* **1984**, *80*, 570-571.

(49) Hegemann, B.; Jonas, J. Separation of Temperature and Density Effects on Collision-Induced Rayleigh and Raman Line-Shapes of Liquid Carbon-Disulfide. *J. Chem. Phys.* **1985**, *82*, 2845-2855.

(50) Fleury, P. A.; Daniels, W. B.; Worlock, J. M. Density and Temperature Dependence of Intermolecular Light Scattering in Simple Fluids. *Phys. Rev. Lett.* **1971**, *27*, 1493-1496.

(51) Ladanyi, B. M.; Barreau, A.; Dumon, B. Density and Temperature Dependence of Spectral Moments in Depolarized Light Scattering by Rare Gases. *Mol. Phys.* **1992**, *77*, 735-767.

(52) Manfred, K.; He, X. X.; Fourkas, J. T. Assessing the Role of Moment of Inertia in Optical Kerr Effect Spectroscopy. *J. Phys. Chem. B* **2010**, *114*, 12096-12103.

(53) Neelakandan, M.; Pant, D.; Quitevis, E. L. Reorientational and Intermolecular Dynamics in Binary Liquid Mixtures of Hexafluorobenzene and Benzene: Femtosecond Optical Kerr Effect Measurements. *Chem. Phys. Lett.* **1997**, *265*, 283-292.

(54) Heisler, I. A.; Meech, S. R. Low-Frequency Isotropic and Anisotropic Raman Spectra of Aromatic Liquids. *J. Chem. Phys.* **2010**, *132*, 174503.

(55) Smith, N. A.; Lin, S. J.; Meech, S. R.; Shirota, H.; Yoshihara, K. Ultrafast Dynamics of Liquid Anilines Studied by the Optical Kerr Effect. *J. Phys. Chem. A* **1997**, *101*, 9578-9586.

(56) Shirota, H.; Fujisawa, T.; Fukazawa, H.; Nishikawa, K. Ultrafast Dynamics in Aprotic Molecular Liquids: A Femtosecond Raman-Induced Kerr Effect Spectroscopic Study. *Bull. Chem. Soc. Jpn.* **2009**, *82*, 1347-1366.

(57) Farrer, R. A.; Loughnane, B. J.; Fourkas, J. T. Dynamics of Confined Carbon Disulfide from 165 to 310 K. *J. Phys. Chem. A* **1997**, *101*, 4005-4010.

(58) Loughnane, B. J.; Farrer, R. A.; Scodinu, A.; Fourkas, J. T. Dynamics of a Wetting Liquid in Nanopores: An Optical Kerr Effect Study of the Dynamics of Acetonitrile Confined in Sol-Gel Glasses. *J. Chem. Phys.* **1999**, *111*, 5116-5123.

(59) Loughnane, B. J.; Fourkas, J. T. Geometric Effects in the Dynamics of a Nonwetting Liquid in Microconfinement: An Optical Kerr Effect Study of Methyl Iodide in Nanporous Glasses. *J. Phys. Chem. B* **1998**, *102*, 10288-10294.

(60) Scodinu, A.; Fourkas, J. T. Comparison of the Orientational Dynamics of Water Confined in Hydrophobic and Hydrophilic Nanopores. *J. Phys. Chem. B* **2002**, *106*, 10292-10295.

(61) Zhu, X.; Farrer, R. A.; Fourkas, J. T. Ultrafast Orientational Dynamics of Nanoconfined Benzene. *J. Phys. Chem. B* **2005**, *109*, 12724-12730.

(62) Drake, J. M.; Klafter, J.; Kopelman, R.; Awschalom, D. D. *Dynamics in Small Confining Systems*; Materials Research Society: Pittsburgh, PA, 1993; Vol. 290.

(63) Drake, J. M.; Klafter, J.; Kopelman, R.; Troian, S. M. *Dynamics in Small Confining Systems II*; Materials Research Society: Pittsburgh, PA, 1995; Vol. 366.

(64) Drake, J. M.; Klafter, J.; Kopelman, R. *Dynamics in Small Confining Systems III*; Materials Research Society: Pittsburgh, PA, 1997; Vol. 464.

(65) Drake, J. M.; Grest, G. S.; Klafter, J.; Kopelman, R. *Dynamics in Small Confining Systems IV*; Materials Research Society: Warrendale, PA, 1999; Vol. 543.

(66) Drake, J. M.; Klafter, J.; Levitz, P. E.; Overney, R. M.; Urbakh, M. *Dynamics in Small Confining Systems V*; Cambridge University Press, 2014.

(67) Liu, D. Z.; Zhang, Y.; Chen, C. C.; Mou, C. Y.; Poole, P. H.; Chen, S. H. Observation of the Density Minimum in Deeply Supercooled Confined Water. *P. Natl. Acad. Sci. USA* **2007**, *104*, 9570-9574.

(68) Liu, D. Z.; Zhang, Y.; Liu, Y.; Wu, J. L.; Chen, C. C.; Mou, C. Y.; Chen, S. H. Density Measurement of 1-D Confined Water by Small Angle Neutron Scattering Method: Pore Size and Hydration Level Dependences. *J. Phys. Chem. B* **2008**, *112*, 4309-4312.

(69) Morineau, D.; Guégan, R.; Xia, Y.; Alba-Simionesco, C. Structure of Liquid and Glassy Methanol Confined in Cylindrical Pores. *J. Chem. Phys.* **2004**, *121*, 1466-1473.

(70) Morineau, D.; Xia, Y.; Alba-Simionesco, C. Finite-Size and Surface Effects on the Glass Transition of Liquid Toluene Confined in Cylindrical Mesopores. *J. Chem. Phys.* **2002**, *117*, 8966-8972.

(71) Xia, Y.; Dosseh, G.; Morineau, D.; Alba-Simionesco, C. Phase Diagram and Glass Transition of Confined Benzene. *J. Phys. Chem. B* **2006**, *110*, 19735-19744.

(72) Bucaro, J. A.; Litovitz, T. A. Rayleigh Scattering: Collisional Motions in Liquids. *J. Chem. Phys.* **1971**, *54*, 3846-3853.

(73) Chang, Y. J.; Castner, E. W. Intermolecular Dynamics of Substituted Benzene and Cyclohexane Liquids, Studied by Femtosecond Nonlinear-Optical Polarization Spectroscopy. *J. Phys. Chem.* **1996**, *100*, 3330-3343.

(74) Hunt, N. T.; Jaye, A. A.; Meech, S. R. Ultrafast Dynamics in Complex Fluids Observed Through the Ultrafast Optically-Heterodyne-Detected Optical-Kerr-Effect (OHD-OKE). *Phys. Chem. Chem. Phys.* **2007**, *9*, 2167-2180.

Chapter 2: Theory

2.1 *Calculating the Simulated Reduced Spectral Density*

2.1.1 *Many-Body Polarizability*

The Optical Kerr effect (OKE) spectrum is dependent on fluctuations of the many-body polarizability of a liquid. To calculate the many-body polarizability, we must first develop a model of the polarizability of an individual molecule. In the dipole/induced-dipole (DID) approximation, the polarizability $\overleftrightarrow{\boldsymbol{\pi}}_i$ of site *i* within a molecule with *n* sites contains a component that is the result of the gas-phase polarizability of the site and a component that arises from interactions of this site with each of the *n* - 1 remaining sites. Thus,

$$\overleftrightarrow{\boldsymbol{\pi}}_i = \overleftrightarrow{\boldsymbol{\alpha}}_i - \overleftrightarrow{\boldsymbol{\alpha}}_i \sum_{j\neq i}^{n} \overleftrightarrow{\boldsymbol{T}}_{ij} \overleftrightarrow{\boldsymbol{\pi}}_j, \tag{2.1}$$

where $\overleftrightarrow{\boldsymbol{\alpha}}_i$ is the polarizability tensor of site *i*

$$\overleftrightarrow{\boldsymbol{\alpha}}_i = \left(\alpha - \frac{\gamma}{3}\right)\overleftrightarrow{\mathbf{1}} + \gamma\hat{\boldsymbol{\Omega}}\hat{\boldsymbol{\Omega}} \tag{2.2}$$

and $\overleftrightarrow{\boldsymbol{T}}_{ij}$ is the dipole-field interaction tensor between sites *i* and *j*

$$\overleftrightarrow{\boldsymbol{T}}_{ij} = \frac{\overleftrightarrow{\mathbf{1}}}{r_{ij}^3} - \frac{3\hat{\boldsymbol{r}}\hat{\boldsymbol{r}}}{r_{ij}^5}. \tag{2.3}$$

Here, $\overleftrightarrow{\mathbf{1}}$ is the unit tensor, α and γ are the isotropic and anisotropic components of the site polarizability tensor, respectively, $\hat{\boldsymbol{\Omega}}$ is the unit vector along the principal symmetry axis, and $\hat{\boldsymbol{r}}$ is the vector of length r_{ij} connecting sites *i* and *j*. For an axially symmetric molecule and assuming that each site has the same axial symmetry as the molecule, the

anisotropic component γ is the tensor component perpendicular to the principal symmetry axis subtracted from the tensor component along this axis.

For molecules with moderate polarizabilities, eq 2.1 can be solved by approximating $\overleftrightarrow{\pi}_j$ as $\overleftrightarrow{\alpha}_j$ and then iterating.[1,2] Alternatively, to solve for a molecule of n polarizable sites, eq 2.1 can be rearranged to find the $3n \times 3n$ matrix representation of the site interactions

$$\overleftrightarrow{\boldsymbol{\alpha}}_i^{-1}\overleftrightarrow{\boldsymbol{\pi}}_i + \sum_{j\neq i}^{n} \overleftrightarrow{\boldsymbol{T}}_{ij}\overleftrightarrow{\boldsymbol{\pi}}_j = \overleftrightarrow{\mathbf{1}}. \tag{2.4}$$

Following this matrix equation, the so-called relay matrix is produced:

$$\overleftrightarrow{\boldsymbol{R}} = \overleftrightarrow{\boldsymbol{\alpha}}_i^{-1} + \overleftrightarrow{\boldsymbol{T}}_{ij}$$

$$= \begin{bmatrix} \overleftrightarrow{\boldsymbol{\alpha}}_1^{-1} & 0 & \cdots & 0 \\ 0 & \overleftrightarrow{\boldsymbol{\alpha}}_2^{-1} & \cdots & 0 \\ \vdots & \vdots & \ddots & \vdots \\ 0 & 0 & \cdots & \overleftrightarrow{\boldsymbol{\alpha}}_n^{-1} \end{bmatrix} + \begin{bmatrix} 0 & \overleftrightarrow{\boldsymbol{T}}_{12} & \cdots & \overleftrightarrow{\boldsymbol{T}}_{1n} \\ \overleftrightarrow{\boldsymbol{T}}_{21} & 0 & \cdots & \overleftrightarrow{\boldsymbol{T}}_{2n} \\ \vdots & \vdots & \ddots & \vdots \\ \overleftrightarrow{\boldsymbol{T}}_{n1} & \overleftrightarrow{\boldsymbol{T}}_{n2} & \cdots & 0 \end{bmatrix}$$

$$= \begin{bmatrix} \overleftrightarrow{\boldsymbol{\alpha}}_1^{-1} & \overleftrightarrow{\boldsymbol{T}}_{12} & \cdots & \overleftrightarrow{\boldsymbol{T}}_{1n} \\ \overleftrightarrow{\boldsymbol{T}}_{21} & \overleftrightarrow{\boldsymbol{\alpha}}_2^{-1} & \cdots & \overleftrightarrow{\boldsymbol{T}}_{2n} \\ \vdots & \vdots & \ddots & \vdots \\ \overleftrightarrow{\boldsymbol{T}}_{n1} & \overleftrightarrow{\boldsymbol{T}}_{n2} & \cdots & \overleftrightarrow{\boldsymbol{\alpha}}_n^{-1} \end{bmatrix}. \tag{2.5}$$

Here, each term in the matrix, which contains the inverse of site polarizabilities on the diagonal and the interaction tensor in the off-diagonal elements, is a 3×3 block of the Cartesian components of the respective terms. Inversion of the relay matrix yields the linear response A_{ij} of the molecule to a uniform electric field, and this response contains the polarizability of the molecule to all orders

$$\overleftrightarrow{\boldsymbol{R}}^{-1} = \overleftrightarrow{\boldsymbol{A}}_{ij} = \left[\overleftrightarrow{\boldsymbol{\alpha}}_i^{-1} + \overleftrightarrow{\boldsymbol{T}}_{ij}\right]^{-1} = \begin{bmatrix} \overleftrightarrow{\boldsymbol{A}}_{11} & \overleftrightarrow{\boldsymbol{A}}_{12} & \cdots & \overleftrightarrow{\boldsymbol{A}}_{1n} \\ \overleftrightarrow{\boldsymbol{A}}_{21} & \overleftrightarrow{\boldsymbol{A}}_{22} & \cdots & \overleftrightarrow{\boldsymbol{A}}_{2n} \\ \vdots & \vdots & \ddots & \vdots \\ \overleftrightarrow{\boldsymbol{A}}_{n1} & \overleftrightarrow{\boldsymbol{A}}_{n2} & \cdots & \overleftrightarrow{\boldsymbol{A}}_{nn} \end{bmatrix}. \tag{2.6}$$

Both $\overleftrightarrow{\boldsymbol{\alpha}}_i^{-1}$ and $\overleftrightarrow{\boldsymbol{T}}_{ij}$ are symmetric tensors, making $\overleftrightarrow{\boldsymbol{R}}$, and therefore $\overleftrightarrow{\boldsymbol{A}}_{ij}$, symmetric as well. Contracting $\overleftrightarrow{\boldsymbol{A}}_{ij}$ along the corresponding Cartesian components yields the 3 × 3 collective polarizability tensor $\overleftrightarrow{\boldsymbol{\pi}}$ of the molecule:

$$\overleftrightarrow{\boldsymbol{\pi}} = \sum_i^n \sum_j^n \overleftrightarrow{\boldsymbol{A}}_{ij}. \tag{2.7}$$

This method of calculating the polarizability requires no iteration and no approximation of the polarizability of any of the molecular sites.

The many-body polarizability, $\overleftrightarrow{\boldsymbol{\Pi}}$, of a liquid containing N molecules can be calculated in the same manner as for the molecular polarizability $\overleftrightarrow{\boldsymbol{\pi}}$ by solving eqs 2.5 and 2.6, taking into account the Nn sites of $\overleftrightarrow{\boldsymbol{\Pi}}$. The purely reorientational collective molecular (CM) contribution ($\overleftrightarrow{\boldsymbol{\Pi}}^{CM}$) to $\overleftrightarrow{\boldsymbol{\Pi}}$ can be calculated by disregarding the intermolecular interactions when constructing the relay matrix. Thus, for molecules *p* and *q*, we have

$$\overleftrightarrow{\boldsymbol{\alpha}}_i^{-1} \overleftrightarrow{\boldsymbol{\pi}}_i + \sum_{j \neq i}^{Nn} \overleftrightarrow{\boldsymbol{T}}_{ij} \overleftrightarrow{\boldsymbol{\pi}}_j \delta_{pq} = \overleftrightarrow{\mathbf{1}}\,, \tag{2.8}$$

and the collective molecular relay matrix becomes

$$\overleftrightarrow{\boldsymbol{R}}^{CM} = \overleftrightarrow{\boldsymbol{\alpha}}_i^{-1} + \overleftrightarrow{\boldsymbol{T}}_{ij} \delta_{pq}\,, \tag{2.9}$$

where δ_{pq} is the Kronecker delta function. Inverting $\overleftrightarrow{\boldsymbol{R}}^{CM}$ and contracting the resulting response map gives $\overleftrightarrow{\boldsymbol{\Pi}}^{CM}$

$$\overleftrightarrow{\boldsymbol{A}}_{ij}^{CM} = \overleftrightarrow{\boldsymbol{R}}^{CM^{-1}} \tag{2.10}$$

and

$$\overleftrightarrow{\boldsymbol{\Pi}}^{CM} = \sum_i^{Nn} \sum_j^{Nn} \overleftrightarrow{\boldsymbol{A}}_{ij}^{CM}. \tag{2.11}$$

The many-body polarizability of a liquid is the sum of the collective molecular component and an interaction-induced (II) component $\left(\overleftrightarrow{\boldsymbol{\Pi}}^{II}\right)$, which can be calculated via

$$\overleftrightarrow{\boldsymbol{\Pi}} = \overleftrightarrow{\boldsymbol{\Pi}}^{CM} + \overleftrightarrow{\boldsymbol{\Pi}}^{II} \tag{2.12}$$

or, equivalently,

$$\overleftrightarrow{\boldsymbol{\Pi}}^{II} = \overleftrightarrow{\boldsymbol{\Pi}} - \overleftrightarrow{\boldsymbol{\Pi}}^{CM} \, . \tag{2.13}$$

$\overleftrightarrow{\boldsymbol{\Pi}}^{II}$ is influenced by both the orientational and translational dynamics in the liquid, making it difficult to separate the spectral contribution of each type of motion. It is therefore common practice to project $\overleftrightarrow{\boldsymbol{\Pi}}^{II}$ onto $\overleftrightarrow{\boldsymbol{\Pi}}^{CM}$ to isolate the reorientaional contribution to the polarizability.[3-9] The projection coefficient *P* is defined as

$$P = \frac{\langle \overleftrightarrow{\boldsymbol{\Pi}}^{CM} \overleftrightarrow{\boldsymbol{\Pi}}^{II} \rangle}{\langle \overleftrightarrow{\boldsymbol{\Pi}}^{CM} \overleftrightarrow{\boldsymbol{\Pi}}^{CM} \rangle} \, . \tag{2.14}$$

The resulting re-partitioning of $\overleftrightarrow{\boldsymbol{\Pi}}$ reveals a reorientational component $\left(\overleftrightarrow{\boldsymbol{\Pi}}^{R}\right)$ and what is termed the collision-induced (CI) component $\left(\overleftrightarrow{\boldsymbol{\Pi}}^{CI}\right)$, which gives rise to any dynamics whose influence on the many-body polarizability is orthogonal to the influence of reorientation

$$\overleftrightarrow{\boldsymbol{\Pi}} = (1 + P)\overleftrightarrow{\boldsymbol{\Pi}}^{CM} + \left(\overleftrightarrow{\boldsymbol{\Pi}}^{II} - P\overleftrightarrow{\boldsymbol{\Pi}}^{CM}\right) = \overleftrightarrow{\boldsymbol{\Pi}}^{R} + \overleftrightarrow{\boldsymbol{\Pi}}^{CI} \, . \tag{2.15}$$

The contributions to isotropic spectra can be derived from the traces of these many-body polarizability tensors, and the contributions to depolarized spectra can be derived from their traceless portions.[10]

2.1.2 *Time Correlation Functions and the Reduced Spectral Density*

For the most commonly implemented form of OKE spectroscopy and depolarized light scattering, the dynamics of interest are the result of fluctuations in the polarizability anisotropy.[11] These fluctuations are encoded on the time correlation function (TCF) of an off-diagonal element of the many-body polarizability, which is given by

$$C_{xy}(t) = \frac{1}{I^2} \langle \overleftrightarrow{\boldsymbol{\Pi}}_{xy}(0) \overleftrightarrow{\boldsymbol{\Pi}}_{xy}(t) \rangle \, , \tag{2.16}$$

where I^2 is the depolarized light scattering intensity for a non interacting system composed of *N* molecules. For a pure liquid, I^2 is given by

$$I^2 = N\Gamma^2/15\ , \tag{2.17}$$

where Γ is the isolated-molecule polarizability anisotropy.

Insertion of eq 2.12 into $C_{xy}(t)$ yields the three contributions to the many-body polarizability TCF: $C_{xy}^{CM}(t)$, $C_{xy}^{II}(t)$, and $C_{xy}^{CMII}(t)$. The first of these contributions is the autocorrelation of the CM component of the polarizability and is purely reorientational. The second contribution is the autocorrelation of the II component of the polarizability and contains the dynamic information pertaining to translation as well as reorientation. The third of these contributions is the cross-correlation between the first two contributions. It is clear that this separation of the three contributions to the polarizability TCF does not differentiate between the different mechanisms of relaxation. Additionally, $C_{xy}^{CMII}(t)$ has almost the same magnitude as $C_{xy}^{CM}(t)$ and decays at a similar rate.[3,9,11,12] It is therefore common to insert eq 2.15 into $C_{xy}(t)$ to separate the reorientational dynamics from all other dynamics that decay orthogonally to reorientation. This insertion yields three different TCFs: $C_{xy}^{R}(t)$, $C_{xy}^{CI}(t)$, and $C_{xy}^{RCI}(t)$. The first of these functions is again purely reorientational, and the second is commonly termed the CI component, although it is unclear if reorientation is completely removed through this projection scheme. The third contribution is again the cross-correlation between the R and CI components, which is much smaller than $C_{xy}^{CMII}(t)$ in magnitude.[5,13]

The OKE response tracks the liquid intermolecular dynamics through the third-order depolarized nuclear response function $R_{nuc}^{(3)}(t)$, which is calculated by taking the negative time derivative of the many-body polarizability TCF

$$R_{nuc}^{(3)}(t) = -\frac{1}{k_B T}\dot{C}_{xy}(t), \tag{2.18}$$

where k_B is the Boltzmann constant and T is temperature. $R_{nuc}^{(3)}(t)$ can be partitioned in the same manner as the TCF, and each of the components of the response is characterized by a peak at early time and a decaying long-time tail. The nuclear response arises from the Raman-active molecular dynamics of the liquid, including diffusive reorientation, which decays with a time scale of picoseconds or more and is generally described by one or more exponentials.[14]

Transforming $R_{nuc}^{(3)}(t)$ into the frequency domain and taking the imaginary portion of the transform produces the depolarized, Bose-Einstein-corrected, low-frequency Raman spectrum, which is also known as the spectral density

$$I(\tilde{\nu}) = Im\mathcal{F}\left[R_{nuc}^{(3)}(t)\right], \tag{2.19}$$

where $\mathcal{F}$ denotes a Fourier transform. The long-time diffusive dynamics are characterized by a sharp peak at low frequency. To remove this peak, the contribution of orientational diffusion is subtracted from$R_{xy}^{(3)}(t)$ before transforming the response, yielding the RSD. The RSD is written as

$$I^*(\tilde{\nu}) = Im\mathcal{F}\left[R_{nuc}^{(3)}(t) - \left(e^{-\tau/\tau_c}\left(1 - e^{-\tau/\tau_{rise}}\right)\right)\right], \tag{2.20}$$

where τ_{rise}, which is generally assumed to be 200 fs or less, is the rise time of the orientationally induced birefringence. The RSD arises from both collective molecular and interaction-induced polarizability fluctuations, giving insight into the intermolecular and intramolecular interactions and dynamics within the liquid. The simulated RSD is calculated with the LabVIEW program presented in Appendix A.

2.2 *Theory of Optical Kerr Effect Experiments*

2.2.1 *OHD-OKE Spectroscopy*

Ultrafast OKE spectroscopy is a third-order, non-resonant, pump-probe technique, wherein ultrafast laser pulses are used to excite and subsequently monitor optically anisotropic liquids.[15,16] When an initially isotropic liquid is exposed to an intense, linearly polarized pump pulse, a transient birefringence is induced within the liquid by driving the molecular axis of maximum polarizability of each molecule toward the polarization axis of the pulse. A weaker, time-delayed probe pulse, which is linearly polarized at some angle relative to the polarization axis of the pump pulse, is depolarized by the induced birefringence of the liquid. By placing a polarizer, which is crossed with the initial polarization axis of the probe pulse, after the excited liquid, the depolarized response can be monitored by measuring the intensity of the transmitted light with a detector. The OKE signal intensity is given by

$$I_{OKE} = \left| E_{OKE} e^{-i\omega t} \right|^2 , \tag{2.21}$$

where E_{OKE} is the amplitude of the electric field corresponding to the depolarized response, ω is the carrier frequency of the laser pulse, and t is the delay between the pump and probe pulses. This experimental configuration is known as homodyne detection and because it is the intensity that is measured, the measured signal is proportional to the squared magnitude of the third-order depolarized response.

The most commonly implemented OKE experimental geometry is an optically-heterodyne-detected (OHD) scheme (Figure 2.1). The pump pulse is polarized at 45° relative to the vertically polarized probe pulse. An “analyzer polarizer” is set to pass horizontally polarized light and is placed after the liquid sample. To heterodyne the

signal, a local oscillator is introduced by placing a quarter-wave plate in the probe beam path between the liquid sample and the first polarizer. The quarter-wave plate has its fast axis aligned with the polarization axis of the first polarizer. The local oscillator is then implemented by rotating the first polarizer in the probe beam path by 1-2°, which is termed the heterodyne angle, allowing a constant leakage of the probe beam through the "analyzer polarizer". The local oscillator field can be written

$$E_{LO} = E_p e^{-i\omega t} e^{i\pi/2}, \tag{2.22}$$

where E_p is the amplitude of the probe pulse field. The local oscillator is in quadrature with the remaining probe beam and mixes in phase with the OKE signal field. The OHD signal intensity is then written

$$I_{OHD}^{+} = \left|E_{OKE} e^{-i\omega t} + E_p e^{-i\omega t} e^{i\pi/2}\right|^2 = I_{OKE} + 2E_{OKE}E_p + I_{LO}. \tag{2.23}$$

To make the signal field linear in the depolarized response, the homodyne and local oscillator contributions to the signal are removed. I_{LO} is the largest term in this equation and is independent of time. By chopping the pump and probe beams and using a differential pre-amplifier, this term can be removed completely from the detected signal. I_{OKE} is removed from the signal by rotating the heterodyne angle in the opposite direction. The phase of the local oscillator is correspondingly adjusted by 180°. The resulting detected OHD intensity is then written

$$I_{OHD}^{-} = I_{OKE} - 2E_{OKE}E_p + I_{LO}. \tag{2.24}$$

Thus, by collecting two OHD-OKE birefringence decays at opposing heterodyne angles, the homodyne contribution to the signal is removed by subtracting the negative homodyne angle decay from the positive heterodyne angle decay. The resulting intensity is linearly proportional to the OKE signal field and is amplified by the local oscillator field. The OKE signal field is sensitive to the third-order response function, $R^{(3)}_{xyxy}(t)$, and OHD-OKE spectroscopy allows this response to be measured directly.[16-20]

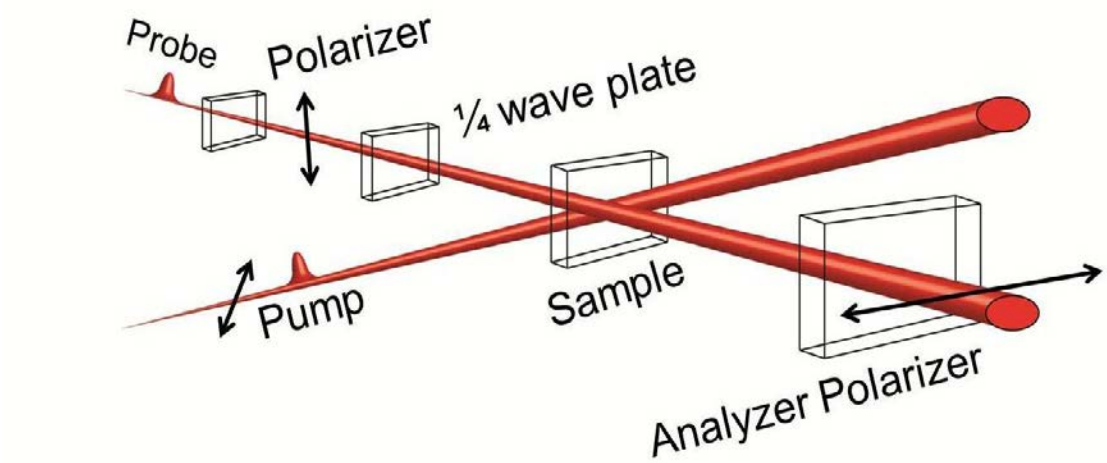

Figure 2.1 Schematic representation of OHD-OKE spectroscopy geometry.

2.2.2 *Fourier Transform Deconvolution*

Using well-established Fourier-transform deconvolution methods,[19,21] $R^{(3)}_{xyxy}(t)$ can be converted into the depolarized, Bose-Einstein-corrected, low-frequency Raman spectrum. The heterodyned signal $S(\tau)$ is a convolution of $R^{(3)}_{xyxy}(t)$ and the second-order autocorrelation of a transform-limited laser pulse, $G^{(2)}(t)$:

$$S(\tau) \propto \int_{-\infty}^{\infty} dt G^{(2)}(t) R^{(3)}_{xyxy}(t-\tau)\,. \tag{2.25}$$

Here, τ is the delay between the pump and probe pulses. Figure 2.2 shows a representative heterodyned decay and the laser pulse shape used to excite the liquid. This

figure shows that the initial peak in the OHD-OKE decay tracks the shape of the laser pulse. The effects of laser pulses of finite duration can be removed from $S(\tau)$ by performing a laser pulse autocorrelation measurement and taking advantage of the Fourier-transform convolution theorem, which states that the transform of the convolution of integrable functions is given by the product of the Fourier transforms of each function.[22] Therefore,

$$\mathcal{F}\left[R^{(3)}_{xyxy}(t)\right] = \frac{\mathcal{F}[S(\tau)]}{\mathcal{F}\left[G^{(2)}(\tau)\right]}, \tag{2.26}$$

where $\mathcal{F}$ denotes a Fourier transform. Back-transforming $\mathcal{F}\left[R^{(3)}_{xyxy}(t)\right]$ then gives the transient birefringent response, which contains information regarding the collective polarizability dynamics of the liquid.

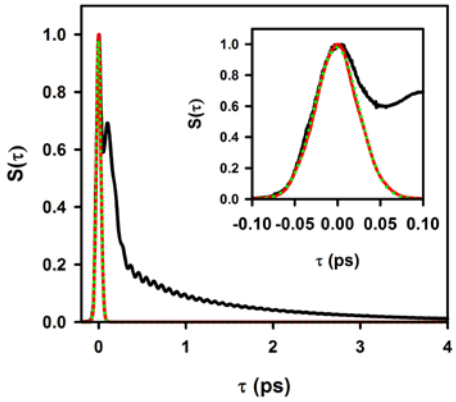

Figure 2.2 Representative OHD-OKE decay for acetonitrile (black) and the excitation pulse shape (red) with a Gaussian fit (green dotted). The inset shows the initial peak of the decay and the effect of the laser pulse shape.

$R^{(3)}_{xyxy}(t)$ is the sum of an electronic response, $R^{(3)}_{el}(t)$, and a nuclear response, $R^{(3)}_{nuc}(t)$.[17,18,23] The nuclear response is the negative time derivative of the many-body

polarizability TCF.[7] To good approximation, $R_{el}(t)$ is a delta function centered about $t = 0$, and its transform is therefore a real constant. Because $R_{el}(t)$ arises from the hyperpolarizability of the liquid and conveys no useful information on dynamics, this contribution is typically removed from $R^{(3)}_{xyxy}(t)$ by back-transforming only the imaginary portion of $\mathcal{F}\left[R^{(3)}_{xyxy}(t)\right]$ (which is also known as the spectral density) to generate the nuclear response.

The nuclear response arises from the Raman-active dynamics of the liquid. On a time scale of picoseconds or more, these dynamics are dominated by collective orientational diffusion. Orientational diffusion typically behaves hydrodynamically in simple liquids, with its contribution to the OKE decay usually taking the form of one or more exponentials.[14] In the case of a single-exponential orientational diffusion decay with time constant τ_{OD}, the diffusive dynamics can be removed from the nuclear response by subtracting a function of the form $e^{-t/\tau_{OD}}\left[1 - e^{-t/\tau_{rise}}\right]$. Here, τ_{rise}, which is generally assumed to be 200 fs or less, is the rise time of the orientational anisotropy induced by the pump pulse. The RSD, $I^*(\tilde{\nu})$, is defined as

$$I^*(\tilde{\nu}) = Im\mathcal{F}\left[R_{nuc}(t) - A\left(e^{-t/\tau_{OD}}\left(1 - e^{-t/\tau_{rise}}\right)\right)\right], \tag{2.27}$$

where *A* is the amplitude of the contribution of diffusive orientation to the decay. Like the simulated spectrum, $I^*(\tilde{\nu})$ arises from both rotational fluctuations and collective II polarizability fluctuations. Figure 2.3 shows a representative RSD for acetonitrile. The peak at ~380 cm^{-1} is a Raman-active bending mode, and the remaining spectrum is the intermolecular contribution arising from librations, II fluctuations, and the cross-term between these components.

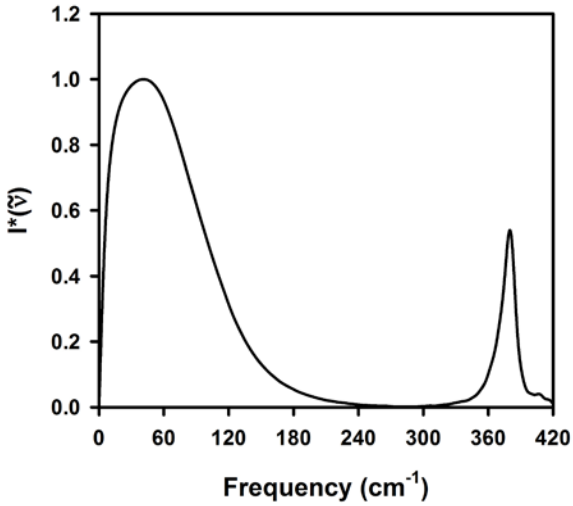

Figure 2.3 RSD for acetonitrile.

2.3 *Polarizability Anisotropy Relaxation Mechanisms*

As has been alluded to in the previous sections, there are several mechanisms by which the induced polarizability anisotropy in OKE spectroscopy decays. The first of these is rotational/orientational diffusion. Orientational diffusion dominates the birefringence decay at long times from approximately 3 ps on. This decay is generally exponential, and in the frequency domain, this simple mechanism appears as a sharp peak at low frequencies. The intramolecular vibrations appear as oscillations in the birefringence decay, and these vibrations generally decay within a few picoseconds (See Figure 2.2). In the frequency domain, intramolecular vibrations appear as sharp peaks in the spectrum. In addition to these two relaxation mechanisms, intermolecular interactions contribute to birefringence response.

The first of the intermolecular mechanisms is libration. Libration is an intermolecular vibration that is the result of hindered rotations as a molecule reorients within its local intermolecular potential. Repulsive intermolecular interactions result in a rocking motion of the molecule as it ricochets off of the molecules making up its nearest

neighbors. In simple liquids, libration contributes across the entire low-frequency Raman spectrum and is the dominant component of the OKE RSD at high frequencies.[4,13,24]

The interaction-induced term in the polarizability of a liquid also contributes to the decay of the birefringence response. The II contribution to polarizability anisotropy relaxation arises from dipole/induced-dipole interactions between molecules. These interactions are dependent on the intermolecular distances and the direction of an applied field. As a molecule moves relative to its surrounding neighbors, its polarizability fluctuates through these interactions. Reorientation and translation contribute to the II component of the polarizability anisotropy decay. For liquids such as benzene, when a distributed polarizability model is employed, simulations have shown that the II contribution to the birefringence decay is significantly smaller than the purely reorientational component.[13] Furthermore, translation is a relatively small contributor to the II polarizability relaxation.

A cross-term between the reorientational and II mechanisms also contributes to the polarizability anisotropy decay. The term is often negative and similar in amplitude to the reorientational component. It decays at a similar rate as the reorientational component as well.

2.4 *References*

(1) Geiger, L. C.; Ladanyi, B. M. Higher-Order Interaction-Induced Effects on Rayleigh Light-Scattering by Molecular Liquids. *J. Chem. Phys.* **1987**, *87*, 191-202.

(2) Birge, R. R.; Schick, G. A.; Bocian, D. F. Calculation of Molecular Polarizabilities Using a Semiclassical Slater-Type Orbital-Point Dipole Interaction (STOPDI) Model. *J. Chem. Phys.* **1983**, *79*, 2256-2264.

(3) Elola, M. D.; Ladanyi, B. M.; Scodinu, A.; Loughnane, B. J.; Fourkas, J. T. Effects of Molecular Association on Polarizability Relaxation in Liquid Mixtures of Benzene and Hexafluorobenzene. *J. Phys. Chem. B* **2005**, *109*, 24085-24099.

(4) Ryu, S.; Stratt, R. M. A Case Study in the Nolecular Interpretation of Optical Kerr Effect Spectra: Instantaneous-Normal-Mode Analysis of the OKE Spectrum of Liquid Benzene. *J. Phys. Chem. B* **2004**, *108*, 6782-6795.

(5) Elola, M. D.; Ladanyi, B. M. Molecular Dynamics Study of Polarizability Anisotropy Relaxation in Aromatic Liquids and Its Connection with Local Structure. *J. Phys. Chem. B* **2006**, *110*, 15525-15541.

(6) Hu, Z. H.; Huang, X. H.; Annapureddy, H. V. R.; Margulis, C. J. Molecular Dynamics Study of the Temperature-Dependent Optical Kerr Effect Spectra and Intermolecular Dynamics of Room Temperature Ionic Liquid 1-Methoxyethylpyridinium Dicyanoamide. *J. Phys. Chem. B* **2008**, *112*, 7837-7849.

(7) Geiger, L. C.; Ladanyi, B. M. Molecular-Dynamics Simulation Study of Nonlinear Optical-Response of Fluids. *Chem. Phys. Lett.* **1989**, *159*, 413-420.

(8) Frenkel, D.; Mctague, J. P. Molecular-Dynamics Studies of Orientational and Collision-Induced Light-Scattering in Molecular Fluids. *J. Chem. Phys.* **1980**, *72*, 2801-2818.

(9) Paolantoni, M.; Ladanyi, B. M. Polarizability Anisotropy Relaxation in Liquid Ethanol: A Molecular Dynamics Study. *J. Chem. Phys.* **2002**, *117*, 3856-3873.

(10) Murry, R. L.; Fourkas, J. T. Polarization Selectivity of Nonresonant Spectroscopies in Isotropic Media. *J. Chem. Phys.* **1997**, *107*, 9726-9740.

(11) Ladanyi, B. M. Molecular-Dynamics Study of Rayleigh Light-Scattering from Molecular Fluids. *J. Chem. Phys.* **1983**, *78*, 2189-2203.

(12) Ladanyi, B. M.; Liang, Y. Q. Interaction-Induced Contributions to Polarizability Anisotropy Relaxation in Polar Liquids. *J. Chem. Phys.* **1995**, *103*, 6325-6332.

(13) Bender, J. S.; Coasne, B.; Fourkas, J. T. Assessing Polarizability Models for the Simulation of Low-Frequency Raman Spectra of Benzene. *J. Phys. Chem. B* **2015**, *119*, 9345-9358.

(14) Berne, B. J.; Pecora, R. *Dynamic Light Scattering*; Wiley: New York, NY, 1976.

(15) Shen, Y.-R. *Principles of Nonlinear Optics*; Wiley-Interscience: New York, NY, 1984.

(16) Fayer, M. D. *Ultrafast Infrared and Raman Spectroscopy*; Marcel Dekker: New York, NY, 2001; Vol. 26.

(17) Zhong, Q.; Fourkas, J. T. Optical Kerr Effect Spectroscopy of Simple Liquids. *J. Phys. Chem. B* **2008**, *112*, 15529-15539.

(18) Righini, R. Ultrafast Optical Kerr-Effect in Liquids and Solids. *Science* **1993**, *262*, 1386-1390.

(19) McMorrow, D.; Lotshaw, W. T. Intermolecular Dynamics in Acetonitrile Probed with Femtosecond Fourier-Transform Raman-Spectroscopy. *J. Phys. Chem.* **1991**, *95*, 10395-10406.

(20) Mcmorrow, D.; Lotshaw, W. T. Evidence for Low-Frequency (~15 Cm^{-1}) Collective Modes in Benzene and Pyridine Liquids. *Chem. Phys. Lett.* **1993**, *201*, 369-376.

(21) McMorrow, D.; Lotshaw, W. T. The Frequency Response of Condensed-Phase Media to Femtosecond Optical Pulses: Spectral-Filter Effects. *Chem. Phys. Lett.* **1990**, *174*, 85-94.

(22) Bracewell, R. N. *The Fourier Transform and Its Applications*; McGraw Hill: New York, NY, 2000.

(23) Hunt, N. T.; Jaye, A. A.; Meech, S. R. Ultrafast Dynamics in Complex Fluids Observed Through the Ultrafast Optically-Heterodyne-Detected Optical-Kerr-Effect (OHD-OKE). *Phys. Chem. Chem. Phys.* **2007**, *9*, 2167-2180.

(24) Murry, R. L.; Fourkas, J. T.; Keyes, T. Nonresonant Intermolecular Spectroscopy Beyond the Placzek Approximation. I. Third-Order Spectroscopy. *J. Chem. Phys.* **1998**, *109*, 2814-2825.

Chapter 3: Experimental Apparatus

3.1 *Introduction*

One of the advantages of optically-heterodyne-detected optical Kerr effect (OHD-OKE) spectroscopy is the simplicity of the design of the spectrometer. The advent of the OHD-OKE geometry of McMorrow and Lotshaw increased the signal-to-noise ratio of the technique significantly.[1,2] The most common experimental geometry is based on their design. Our implementation of this design is presented here.

3.2 *OHD-OKE Spectrometer*

Figure 3.1 shows a schematic of our OHD-OKE spectrometer. A 4.3-W portion of the output of a continuous-wave, solid-state, 532-nm laser (Coherent Verdi 12) is used to pump a 76-MHz, mode-locked Ti:sapphire oscillator (KMLabs TS) to produce ~380 mW of average output power (5 nJ per pulse). The Ti:sapphire spectrum is centered at ~810 nm with a 25 nm full-width-at-half-maximum spectral bandwidth. The laser beam is reflected multiple times between a pair of negatively-chirped mirrors and then passes through an external prism compressor to produce nearly-transform-limited Gaussian pulses with ~44 fs duration (within ~14% of the transform limit) at the sample position.

The laser output is split into pump and probe beams, each of which passes through a different ring on a chopper wheel. The pump-beam polarization is set to vertical using a half-wave plate and a polarizer. The beam is then focused into the sample with an achromatic lens. After passing through the sample, the pump beam is frequency-doubled with a KDP crystal. The second-harmonic signal is collected with a photodiode,

which is connected to a lock-in amplifier (Stanford Research Systems SR810) referenced to the chopping frequency of the pump beam. The frequency-doubled pump-beam intensity is used to compensate for long-term drift in laser intensity, as this signal has the same nonlinearity as the heterodyne-detected OKE signal.

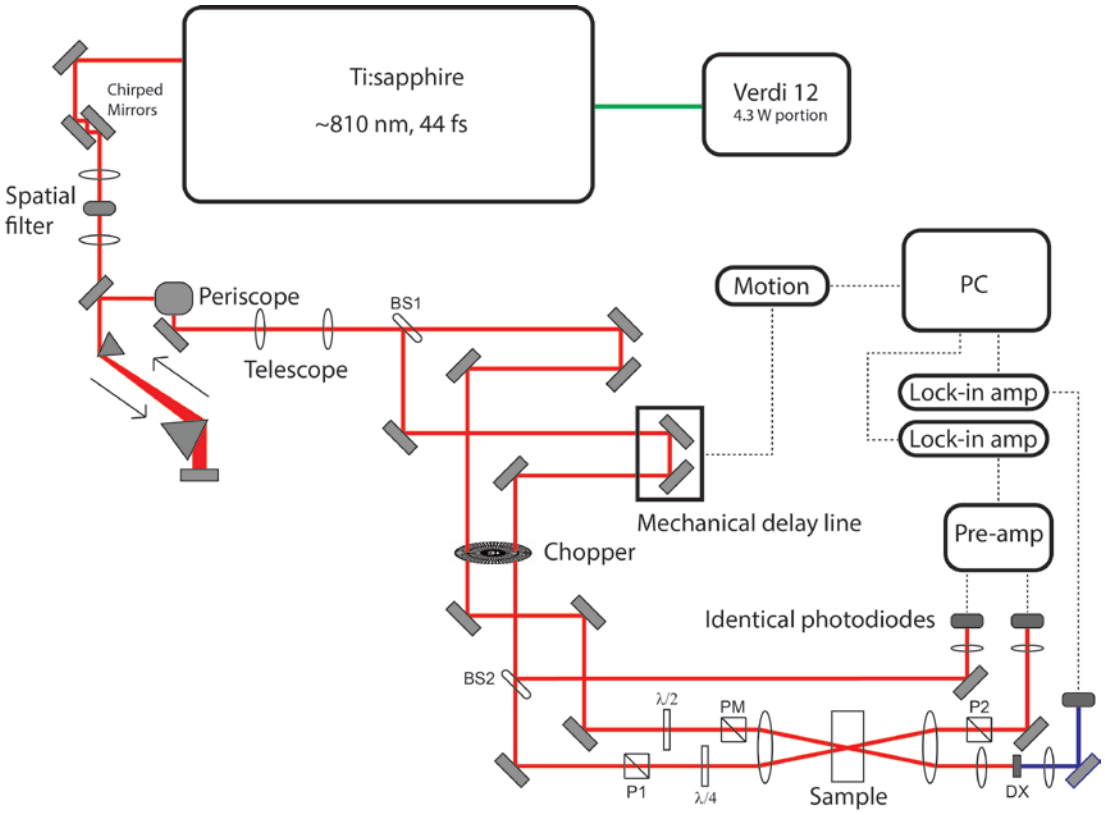

Figure 3.1 Schematic of OHD-OKE spectrometer. BS1, BS2 = 9:1 ratio beamsplitter; P1, PM = Identical Glan-Laser Polarizers; P2 = Glan-Thompson polarizer; DX = KDP doubling crystal

After traversing a mechanical delay line, the probe beam is sent through a polarizer set to pass light polarized at 45° relative to the pump polarization. The probe beam is then passed through a quarter-wave plate that has its fast axis set along the probe polarization angle. The achromatic lens is used to focus the probe beam at the same position in the sample as the pump beam. After the sample, the probe beam is re-

collimated and passes through an analyzer polarizer that is set to transmit light polarized at -45° relative to the pump polarization. To implement optical heterodyne detection, the first polarizer in the probe beam path is rotated by ±2° to allow a local oscillator to mix in-phase with the signal field and in-quadrature with the remaining probe. A low-noise, amplified photodiode is used to detect the leakage through the analyzer polarizer. The photodiode signal is then sent to an analog pre-amplifier (Stanford Research Systems SR560).

To remove the constant local-oscillator intensity contribution to the signal, a small portion of the probe beam is picked off and used as a reference beam. The reference intensity is used to set the intensity of the local oscillator at opposing heterodyne angles in the absence of the pump beam. The reference beam is collected using an amplified photodiode identical to the one that collects the OKE signal. The photodiode signal is sent to the same analog pre-amplifier, where the local oscillator intensity is subtracted from the collected signal. The output of the pre-amplifier (sum of heterodyne and homodyne signal) is sent to a lock-in amplifier referenced to the sum of the pump and probe chopping frequencies. LabVIEW programs are used to control the delay line and to collect data.[3] To remove the homodyne contribution to the signal, the difference between scans at opposite heterodyne angles is calculated and averaged to form a single data set.

3.3 *References*

(1) McMorrow, D.; Lotshaw, W. T. The Frequency Response of Condensed-Phase Media to Femtosecond Optical Pulses: Spectral-Filter Effects. *Chem. Phys. Lett.* **1990**, *174*, 85-94.

(2) McMorrow, D.; Lotshaw, W. T. Intermolecular Dynamics in Acetonitrile Probed with Femtosecond Fourier-Transform Raman-Spectroscopy. *J. Phys. Chem.* **1991**, *95*, 10395-10406.

(3) Zhong, Q. Optical Kerr Effect Spectroscopy of Simple Liquids, University of Maryland, 2009.

Chapter 4: Assessing Polarizability Models for the Simulation of Low-Frequency Raman Spectra of Benzene

Adapted from: Bender, J.S.; Coasne, B.; Fourkas, J.T. *J. Phys. Chem. B*, **2015**, *119(29)*, 9345-9358.
Research designed and conducted by: John S. Bender
Authored by: John S. Bender

4.1 *Introduction*

Optical Kerr effect (OKE) spectroscopy is a powerful and popular technique for probing the orientational, intramolecular, and intermolecular dynamics of simple and complex liquids.[1-3] Time-domain, depolarized OKE spectroscopy monitors the dynamics of molecules by using one ultrafast pulse to induce birefringence in the sample and a subsequent ultrafast pulse to measure the decay of the anisotropy in the refractive index. The time-dependent response, which arises from diffusive reorientation and Raman-active intramolecular and intermolecular modes, can be separated from the instrument response using a Fourier-transform deconvolution technique.[4] This transformation yields the Bose-Einstein-corrected, low-frequency Raman spectrum. Diffusive reorientation can also be removed from the deconvolved birefringence response, producing the so-called reduced spectral density (RSD).

It is difficult to interpret the OKE RSD in a detailed manner, due to its characteristic broad shape that typically has few distinct features. This problem is further exacerbated by the fact that the RSD contains contributions resulting from collective molecular (CM) and interaction-induced (II) scattering, as well as cross terms between them.[5,6] Empirical functions have been used for fitting RSDs as a means of extracting dynamic information,[7-9] but there is no rigorous connection between these functions and either the scattering mechanisms or the microscopic motions of molecular liquids.

Molecular simulation of OKE spectra offers a complementary approach that allows the individual contributions to the response to be analyzed independently. Although simulations can provide insight into the nature of the contributions to the OKE spectrum, the properties of simulated spectra depend on the choice of both the molecular polarizability model and the molecular potential model. For example, Elola and Ladanyi[10] have calculated the OKE spectrum of chloroform and acetonitrile with two different polarizability models: a point polarizability placed at the center of mass of the molecule, and a distributed model with point polarizabilities placed at multiple sites on the molecule. The differences in the shape and breadth of the spectra are substantial for the two models, and the distributed model yields better agreement with the experimental data.[10] Chellie *et al.*[11] calculated the OKE spectrum of benzene using Lennard-Jones[12] and Buckingham-type[11] potentials, and found that although the spectra covered the same frequency range, the structure of the spectrum is impacted substantially by the choice of the potential.

The low-frequency Raman spectrum of benzene has been studied extensively in both the time and frequency domains through experiments[8,9,13-24] and molecular simulations.[11,18,25-28] McMorrow and Lotshaw observed the broad, flattened shape of the benzene OKE spectrum in 1993, and on a preliminary basis concluded that the spectral features are a result of collective modes arising from molecular aggregates.[21] Ricci *et al.*[9] later concluded that the spectral shape arises mostly from librations within the solvent "cage," and is much more collective in nature. The inherent difficulty in assigning these spectral features has been the inspiration for simulations that allow for analysis of the spectral shape in a more definitive manner.

Ryu and Stratt[25] performed an in-depth analysis of the benzene OKE spectrum using instantaneous normal modes.[29,30] They found that the spectrum arises largely from hindered rotational modes, but that the interaction-induced portion of the spectrum at low frequency is dominated by hindered translations. In contrast, Elola and Ladanyi[26] found, in a study employing molecular dynamics (MD) simulations and Steele theory,[31] that the description of the interaction-induced portion of the spectrum depends on the polarizability model used. In particular, a point molecular polarizability model emphasized hindered translational dynamics much more than did a distributed polarizability model.[26] The experimental results of Loughnane *et al.* also suggest that it is unlikely that hindered translations contribute significantly to the depolarized OKE spectrum of benzene.[13]

In simulating OKE spectra, there is an inevitable trade-off between the accuracy of the simulated spectrum and the computational effort required. On one hand, the more distributed the polarizability within a molecule, the more realistic the simulated spectrum is likely to be. On the other hand, a greater degree of polarizability distribution makes the calculation of the many-body polarizability less efficient due to a more time-consuming matrix inversion (*vide infra*), reducing the degree of convergence within a fixed computational time. The distributed polarizability model that has been explored previously for benzene is not necessarily realistic, in that the polarizable sites within a molecule are not allowed to interact with one another.[26] Intuitively, one might expect that an interaction with a dipole on one end of a highly polarizable, conjugated molecule such as benzene would be felt across the entire molecule. Therefore, here we develop two different completely distributed models in which all sites within a molecule are allowed

to interact. In one model the sites are isotropic, and in the other they are anisotropic. We benchmark distributed models against a point molecular polarizability model.

Our computations of the many-body polarizability of liquid benzene are performed using an all-orders approach that is exact within the dipole/induced-dipole (DID) approximation. This approach requires the inversion of a large matrix,[6] which is computationally expensive. Hu *et al.* developed an approximation to the full-inversion approach called the atomic to molecular polarizability transformation (AMPT).[32] This method focuses on atomistic DID interactions between pairs of molecules, and provides considerably greater computational efficiency than does the full-inversion method because the matrices involved are considerably smaller. We also test this method against full inversion for the distributed models explored here.

Finally, as discussed above, the accuracy of the computed OKE spectrum depends on the quality of the molecular force field employed. Because the many-body polarizability depends on both dynamics and structure, it is important to test the different molecular polarizability models using a force field that captures both aspects of the liquid. We have therefore chosen to use the model developed by Bonnaud *et al.*,[33] which not only captures dynamic aspects of the liquid well but also gives a highly faithful reproduction of the liquid structure. The use of the same realistic force field to describe benzene allows us to assess the effect of the different molecular polarizability models and their different inherent approximations (point anisotropic polarizability, noninteracting distributed polarizability, interacting isotropic distributed polarizability, and interacting anisotropic distributed polarizability).

4.2 *Theory*

4.2.1 *Many-Body Polarizability*

The many-body polarizability for liquid benzene is calculated in the manner outlined in Chapter 2, Section 2.1. For this study, the liquid is composed of *N* molecules, each with *n* polarizable sites. We also develop two models of the molecular polarizability of benzene.

The interaction tensor in eq 2.3 treats the interacting sites as points and can cause the calculated polarizability to become unrealistically large at short distances. A number of approaches have been proposed to account for this shortcoming.[32,34-36] Here we follow the approach of Thole, who developed a field tensor in which one of the interacting sites is smeared out in space.[34,35] The Thole interaction tensor damps the interactions at short distances and prevents polarizability singularities in the event that two or more sites make contact during a simulation. This modified interaction tensor is derived from a hydrogenic charge distribution and takes the form

$$\overleftrightarrow{\boldsymbol{T}}_{ij(kl)} = \frac{\delta_{kl}}{r_{ij}^3}\left[1 - \left(\frac{a^2u_{ij}^2}{2} + au_{ij} + 1\right)e^{-au_{ij}}\right] - \frac{3r_{ijk}r_{ijl}}{r_{ij}^5}\left[1 - \left(\frac{a^3u_{ij}^3}{6} + \frac{a^2u_{ij}^2}{2} + au_{ij} + 1\right)e^{-au_{ij}}\right], \quad (4.1)$$

where δ_{kl} is the Kronecker delta function, r_{ijk} and r_{ijl} are the *k* and *l* components of the vector connecting sites *i* and *j* ($k, l \in x, y, z$), u_{ij} is the scaled distance between sites *i* and *j*, and a is a screening parameter that dictates the degree to which the interacting dipole is distributed. The scaled distance takes the form

$$u_{ij} = r_{ij}/\left(\alpha_i\alpha_j\right)^{1/6}, \quad (4.2)$$

where α_i and α_j are the isotropic components of the polarizabilities of sites *i* and *j*.

For a liquid, the inversion of the relay matrix can become burdensome, as the number of elements of the tensor scales with the square of the number of sites Nn in the liquid. For this reason, here we also test the AMPT approximation developed by Hu *et al.*[32] The AMPT algorithm reduces the size of the collective polarizability tensor drastically, and thereby decreases the memory requirements for the computation of the many-body polarizability and its components. The process effectively divides the $3Nn \times 3Nn$ site interaction matrix of the liquid into intramolecular and intermolecular atomic interaction blocks for each pair of molecules. These blocks are solved independently for all pairs of molecular interactions and contracted. The full relay matrix is then recast in the molecular form to reduce its size from $3Nn \times 3Nn$ to $3N \times 3N$. This procedure provides computationally efficient inversion of the relay matrix with little loss of accuracy and, in fact, yields exact results for a two-molecule interaction. In effect, two-molecule interactions are treated at the atomic level, whereas interactions among three or more molecules are treated at the molecular level.

4.2.2 *Time Correlation Functions and Reduced Spectral Density*

The many-body polarizability time correlation function (TCF) can be written in terms of the orientational average (i.e., making use of the entire polarizability tensor) of an off-diagonal element of the tensor and the depolarized light scattering intensity:[10,18,26,27,37]

$$C_{xy}(t) = \frac{1}{2N\Gamma^2}\left[3PP\left(\overleftrightarrow{\mathbf{\Pi}}(0), \overleftrightarrow{\mathbf{\Pi}}(t)\right) - Tr\left(\overleftrightarrow{\mathbf{\Pi}}(0)\right) Tr\left(\overleftrightarrow{\mathbf{\Pi}}(t)\right)\right]. \qquad (4.3)$$

Here, Γ is the molecular polarizability anisotropy, $Tr(\vec{\vec{X}})$ represents the trace of $\vec{\vec{X}}$ and $PP(\vec{\vec{X}},\vec{\vec{Y}})$ represents the pair-wise product of $\vec{\vec{X}}$ and $\vec{\vec{Y}}$, which is given by

$$PP(\vec{\vec{X}},\vec{\vec{Y}}) = \sum_{ij} \vec{\vec{X}}_{ij}\vec{\vec{Y}}_{ij} \ . \tag{4.4}$$

Inserting eq 2.12 into eq 4.3 gives rise to the three terms in the depolarized, collective polarizability TCF: the CM and II autocorrelation functions and the cross-correlation function between these contributions

$$\begin{aligned} C_{xy}(t) &= C_{xy}^{CM}(t) + C_{xy}^{II}(t) + C_{xy}^{CMII}(t) \\ &= \frac{1}{2N\Gamma^2}\left[3PP\left(\vec{\vec{\Pi}}^{CM}(0),\vec{\vec{\Pi}}^{CM}(t)\right) - Tr\left(\vec{\vec{\Pi}}^{CM}(0)\right)Tr\left(\vec{\vec{\Pi}}^{CM}(t)\right)\right] \\ &+ \frac{1}{2N\Gamma^2}\left[3PP\left(\vec{\vec{\Pi}}^{II}(0),\vec{\vec{\Pi}}^{II}(t)\right) - Tr\left(\vec{\vec{\Pi}}^{II}(0)\right)Tr\left(\vec{\vec{\Pi}}^{II}(t)\right)\right] \\ &+ \frac{1}{N\Gamma^2}\left[3PP\left(\vec{\vec{\Pi}}^{CM}(0),\vec{\vec{\Pi}}^{II}(t)\right) - Tr\left(\vec{\vec{\Pi}}^{CM}(0)\right)Tr\left(\vec{\vec{\Pi}}^{II}(t)\right)\right]. \end{aligned} \tag{4.5}$$

For benzene, the collective molecular and interaction-induced functions are both positive, with the former having typically a much larger amplitude. The cross term is typically negative, with an amplitude that is similar to that of the collective molecular function.

Correspondingly, insertion of eq 2.15 into eq 4.3 reveals the reorientational and collision-induced autocorrelations and their cross-correlation

$$\begin{aligned} C_{xy}(t) &= C_{xy}^{R}(t) + C_{xy}^{CI}(t) + C_{xy}^{RCI}(t) \\ &= \frac{1}{2N\Gamma^2}\left[3PP\left(\vec{\vec{\Pi}}^{R}(0),\vec{\vec{\Pi}}^{R}(t)\right) - Tr\left(\vec{\vec{\Pi}}^{R}(0)\right)Tr\left(\vec{\vec{\Pi}}^{R}(t)\right)\right] \\ &+ \frac{1}{2N\Gamma^2}\left[3PP\left(\vec{\vec{\Pi}}^{CI}(0),\vec{\vec{\Pi}}^{CI}(t)\right) - Tr\left(\vec{\vec{\Pi}}^{CI}(0)\right)Tr\left(\vec{\vec{\Pi}}^{CI}(t)\right)\right] \\ &+ \frac{1}{N\Gamma^2}\left[3PP\left(\vec{\vec{\Pi}}^{R}(0),\vec{\vec{\Pi}}^{CI}(t)\right) - Tr\left(\vec{\vec{\Pi}}^{R}(0)\right)Tr\left(\vec{\vec{\Pi}}^{CI}(t)\right)\right]. \end{aligned} \tag{4.6}$$

These functions are similar to the functions in eq 4.5. However, the cross term in eq 4.6 is typically much smaller in amplitude than that in eq 4.5, presumably because of the

orthogonal nature of the reorientational and collision-induced terms. As shown below, the reorientational function mirrors $C_{xy}(t)$, suggesting that reorientation dominates the dynamics of liquid benzene.

We can also calculate a depolarized, single-molecule polarizability TCF via

$$C_{xy}^{SM}(t) = \frac{1}{2N\Gamma^2}\sum_{\ell}\left[3PP\left(\overleftrightarrow{\boldsymbol{\pi}}_{\ell}(0), \overleftrightarrow{\boldsymbol{\pi}}_{\ell}(t)\right) - Tr\left(\overleftrightarrow{\boldsymbol{\pi}}_{\ell}(0)\right)Tr\left(\overleftrightarrow{\boldsymbol{\pi}}_{\ell}(t)\right)\right], \qquad (4.7)$$

where the sum is over all molecules ℓ. This TCF does not contain the pair contributions that are in $C_{xy}^{CM}(t)$. Thus, whereas $C_{xy}^{CM}(t)$ decays at long time with the collective orientational correlation time, τ_c, $C_{xy}^{SM}(t)$ decays at long time with the single-molecule orientational correlation time, τ_s.

The RSD for liquid benzene is then calculated according to Chapter 2, Section 2.1, Subsection 2.1.2 using eqs 4.5 and 4.6.

4.3 *Computational and Simulation Details*

4.3.1 *Polarizability Model Parameters*

Here we examine the behavior of the low-frequency Raman spectrum of benzene using four different molecular polarizability models. In each model, the isotropic (A) and anisotropic (Γ) components of the molecular polarizability are 10.39 Å^3 and -5.62 Å^3, respectively, corresponding to the experimental values for an isolated molecule measured at 632.8 nm.[38]

Figure 4.1 depicts these models schematically. The first model employs a single point anisotropic polarizability (PAP) placed at the center of mass of the molecule. The remaining three models each feature six polarizability sites placed at the carbon centers for the empirical molecule, for which the C-C bond length is 1.40 Å. The non-interacting

distributed (NID) model, which was developed by Mossa *et al.*, evenly distributes the molecular polarizability among the six carbon atom sites of the benzene molecule (i.e. $\overleftrightarrow{\boldsymbol{\alpha}}_i = \overleftrightarrow{\boldsymbol{\pi}}/6$).[39] The PAP and NID models both use the DID interaction tensor (eq 2.3), and neither model takes into account the site interactions within a molecule.

The other two models are distributed models that take both intramolecular and intermolecular interactions into account, thereby distributing the molecular polarizability to a greater extent (in the sense that a dipole induced on one end of a molecule will have an effect on the opposite end of the molecule). Both models use the modified Thole interaction tensor (eq 4.1), smearing one of two interacting sites in space. In the interacting isotropic distributed (IID) model each of the six polarizability sites is isotropic. To determine the appropriate parameters for this model, we calculated the gas-phase polarizability of each site $\overleftrightarrow{\boldsymbol{\alpha}}_i$ and the screening parameter a of the interaction tensor by fitting the Thole model to the isotropic and anisotropic components of the experimental polarizability of an isolated molecule. The initial fitting values were taken as the sum of the polarizability values for carbon and hydrogen determined by van Duijnen and Swart,[35] in which the isotropic polarizabilities are 1.3030 $Å^3$ and 0.5140 $Å^3$ for carbon and hydrogen, respectively. The initial screening constant was 1.9088. The final fitted parameters are 2.2619 $Å^3$ for the isotropic polarizability of each site and 2.2451 for the screening constant. The calculated molecular polarizability is within 0.1% of the experimental value.

In the interacting anisotropic distributed (IAD) model, each site polarizability is anisotropic, with one value in the plane of the molecule and another value perpendicular to that plane. The polarizability of each site was fit to the experimental value in the same manner as in the IID model, and the screening constant was held at 1.9088. The initial fitting values for the polarizability sites were taken from the value of an isolated CH group as determined within the Thole model. The final fitted parameters are 2.2280 $Å^3$ and -0.4960 $Å^3$ for the isotropic and anisotropic components of the polarizability, respectively. The calculated molecular polarizability is within 0.1% of the experimental value.

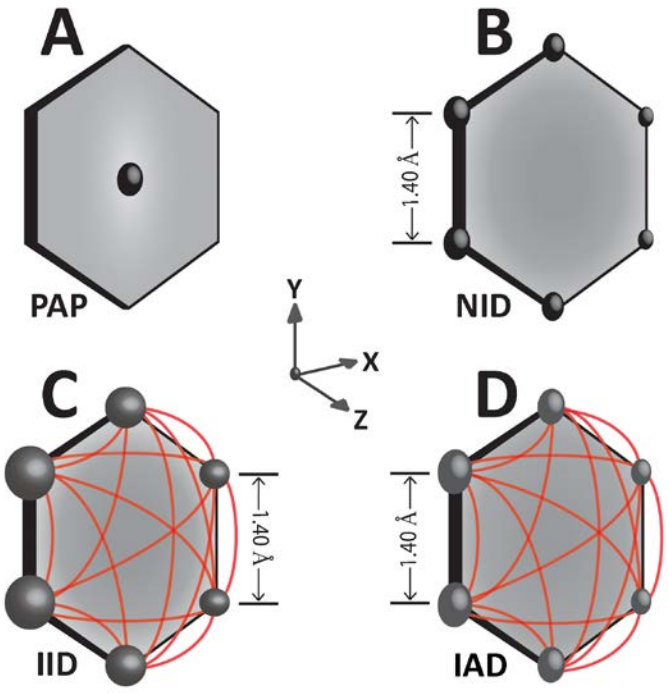

Figure 4.1 Schematic depiction of the four molecular polarizability models tested. (A) In the point anisotropic polarizability model, an anisotropic point polarizability is placed at the center of mass of benzene. (B) In the non-interacting distributed model, anisotropic point polarizabilities are placed on each carbon site, but do not interact with one another. (C) In the interacting isotropic distributed model, isotropic polarizabilities are placed at each carbon site. (D) In the interacting anisotropic distributed model, anisotropic polarizabilities are placed at each carbon site. Red lines denote DID interactions between polarizable sites.

4.3.2 *Molecular Potential*

The different molecular polarizability models were tested using MD trajectories obtained using the 9-site, anisotropic united-atom model for benzene developed by Bonnaud *et al.*, the parameters for which are listed in Table 4.1.[33] This model contains six sites for the CH groups of the benzene ring, which are offset from the actual carbon sites. Two additional, negatively charged sites are placed on either side of the ring to mimic the π-electron system of the molecule, and one positively charged site is placed at the center of the ring to balance the negative charges. These nine sites interact through the potential

$$U = 4\epsilon\left[\left(\frac{\sigma}{r_{ij}}\right)^{12} - \left(\frac{\sigma}{r_{ij}}\right)^{6}\right] + \frac{1}{4\pi\epsilon_0}\sum_{i\neq j}\frac{q_i q_j}{r_{ij}}, \tag{4.8}$$

where ϵ and σ are the Lennard-Jones parameters for the potential well depth and characteristic site radius, ϵ_0 is the permittivity of free space, and q_i and q_j are the charges on sites *i* and *j*, respectively. There are no torsional, bending, or stretching energies included in the potential because the six CH sites are unified and the benzene ring is treated as rigid.

Table 4.1 Intermolecular potential parameters for benzene

r(CH-CH)	1.715 Å
q(z = 0.0 Å)[a]	+8.130e
q(z = ±0.4 Å)[a]	-4.065e
σ_{CH}	3.361 Å
ε_{CH}/k_B	75.6 K

[a]Along the axis normal to the benzene ring

4.3.3 *MD Simulations*

182 benzene molecules were placed in a simulation box measuring 30 Å on each side, corresponding to a liquid density of 0.874 g/cm^3. MD simulations of benzene were performed with DLPOLY V2[40] using the potential in eq 4.8, and the Verlet Leapfrog

algorithm[41] was used to integrate the equations of motion every 5 fs. Periodic boundary conditions were employed with a cutoff distance of 15 Å for the Lennard-Jones interactions, and Ewald summation was used to evaluate the long-range electrostatic intermolecular forces.[41] The simulation was equilibrated at 293 K in the NVT ensemble for 100 ps using a Nosé-Hoover thermostat[42] with a relaxation constant of 10 fs. After the equilibration period, the simulation was performed at 293 K in the NVE ensemble with no thermostat, and configurations were stored at every time step out to 2 ns to ensure sufficient convergence of the calculated quantities.

4.3.4 *Collective Polarizability TCF and RSD Analysis*

Starting at 2.5 ps, we fit the simulated collective polarizability TCFs to one exponential function, corresponding to the decay arising from orientational diffusion. This decay was then removed from the OKE nuclear response functions in the same manner as described in section 2.1.2, assuming a rise time of 200 fs. After Fourier transformation of the response functions, the resultant RSDs were smoothed using a Savitzky-Golay filter.[43]

4.4 *Results*

4.4.1 *Collective Molecular and Interaction-Induced Correlation Functions*

To assess the role of the polarizability model in the simulated RSD of benzene, we begin with the depolarized TCFs for this liquid. The TCFs corresponding to the terms in eq 4.5 are shown in Figure 4.2. The functions for the PAP, NID, IID, and IAD models are shown in panels A, B, C, and D, respectively.

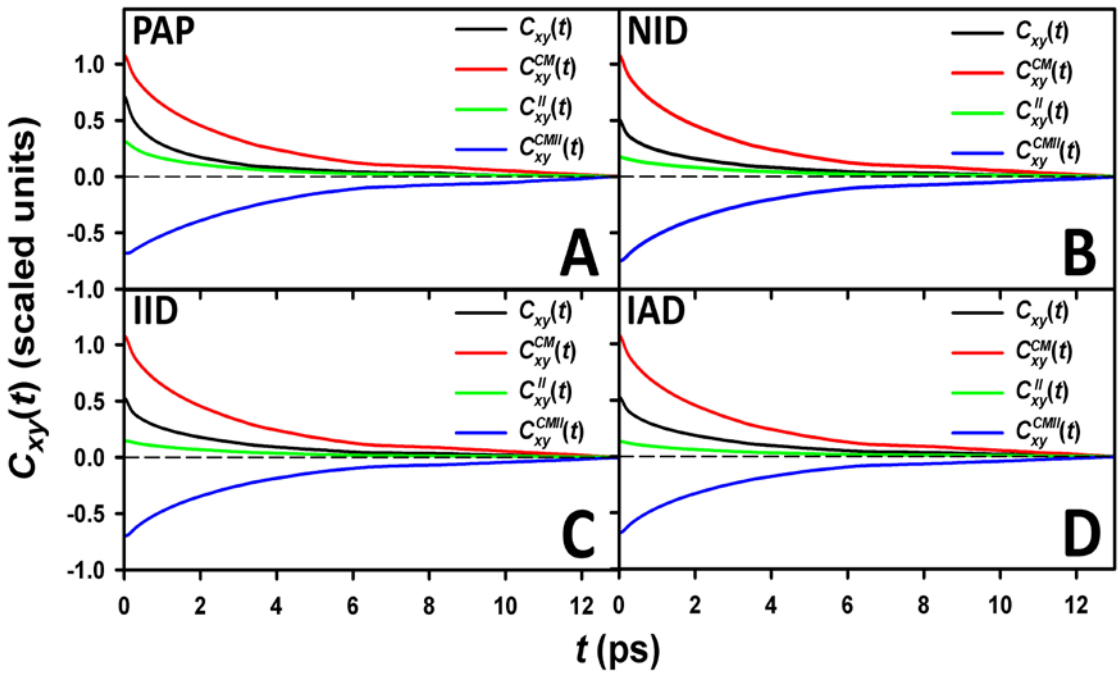

Figure 4.2 Full (black), collective molecular (red), interaction-induced (green), and cross-term (blue) depolarized, many-body polarizability TCFs for (A) the point anisotropic polarizability, (B) the non-interacting distributed polarizability, (C) the interacting isotropic distributed polarizability, and (D) the interacting anisotropic distributed polarizability models of liquid benzene.

$C_{xy}(t)$ has the largest amplitude in the PAP model. The magnitudes of $C_{xy}(t)$ in the remaining three models are roughly equal to each other and are ~77% as large as the PAP TCF. $C_{xy}^{CM}(t)$ is the dominant component of $C_{xy}(t)$. This collective molecular contribution is identical for each of the four models, reflecting its purely additive nature. $C_{xy}^{II}(t)$ makes a significant contribution to $C_{xy}(t)$ in each of the four models. However, the amplitude of the interaction- induced function decreases as the polarizability becomes more distributed. $C_{xy}^{CMII}(t)$ is negative for each of the models, with an amplitude that is similar to that of the collective molecular contribution, suggesting that the dynamics contained in the interaction-induced and collective molecular contributions are correlated. As the polarizability becomes more distributed, the cross-correlation amplitude decreases in a manner similar to that of the interaction-induced functions.

The TCFs show the typical long-time exponential character of the OKE decay for benzene. Table 4.2 shows the fit parameters for the diffusive contributions to $C_{xy}(t)$, $C_{xy}^{CM}(t)$, and $C_{xy}^{II}(t)$. The time constant for all of the orientational decays is on the order of 3.2 ps, which is in good agreement with the experimental decay time.[9,15]

Table 4.2 Amplitudes (A) and Time Constants (τ) from Exponential Fits to the Diffusive Portion of the Total, Collective Molecular, and Interaction-Induced Polarizability TCFs[a]

	$C_{xy}(t)$		$C_{xy}^{CM}(t)$		$C_{xy}^{II}(t)$	
	A	**τ (ps)**	***A***	**τ (ps)**	***A***	**τ (ps)**
PAP	0.295(6)	3.23(8)	0.839(2)	3.20(1)	0.311(2)	0.222(1)
NID	0.291(2)	3.17(7)	0.839(2)	3.20(1)	0.211(1)	0.1506(5)
IID	0.324(2)	3.17(7)	0.839(2)	3.20(1)	0.178(1)	0.1268(4)
IAD	0.343(2)	3.17(7)	0.839(2)	3.20(1)	0.161(1)	0.1149(4)

[a]Numbers in parentheses are uncertainties in the last digit.

4.4.2 *Collective Molecular and Interaction-Induced Response Functions*

The depolarized OKE response functions calculated using the four polarizability models are shown in Figure 4.3. $R_{xy}(t)$, $R_{xy}^{CM}(t)$, $R_{xy}^{II}(t)$, and $R_{xy}^{CMII}(t)$ are shown in panels A, B, C, and D, respectively. The response functions have been scaled to the maximum value of $R_{xy}(t)$ for the PAP model. $R_{xy}(t)$ peaks at ~100 fs, with the PAP response function having the highest amplitude. The amplitude of the initial peak decreases as the polarizability becomes more distributed. The PAP response function is also considerably broader than the other three response functions. At ~250 fs the trend in intensity reverses for the three distributed models, as is evident from the inset of Figure 4.3A.

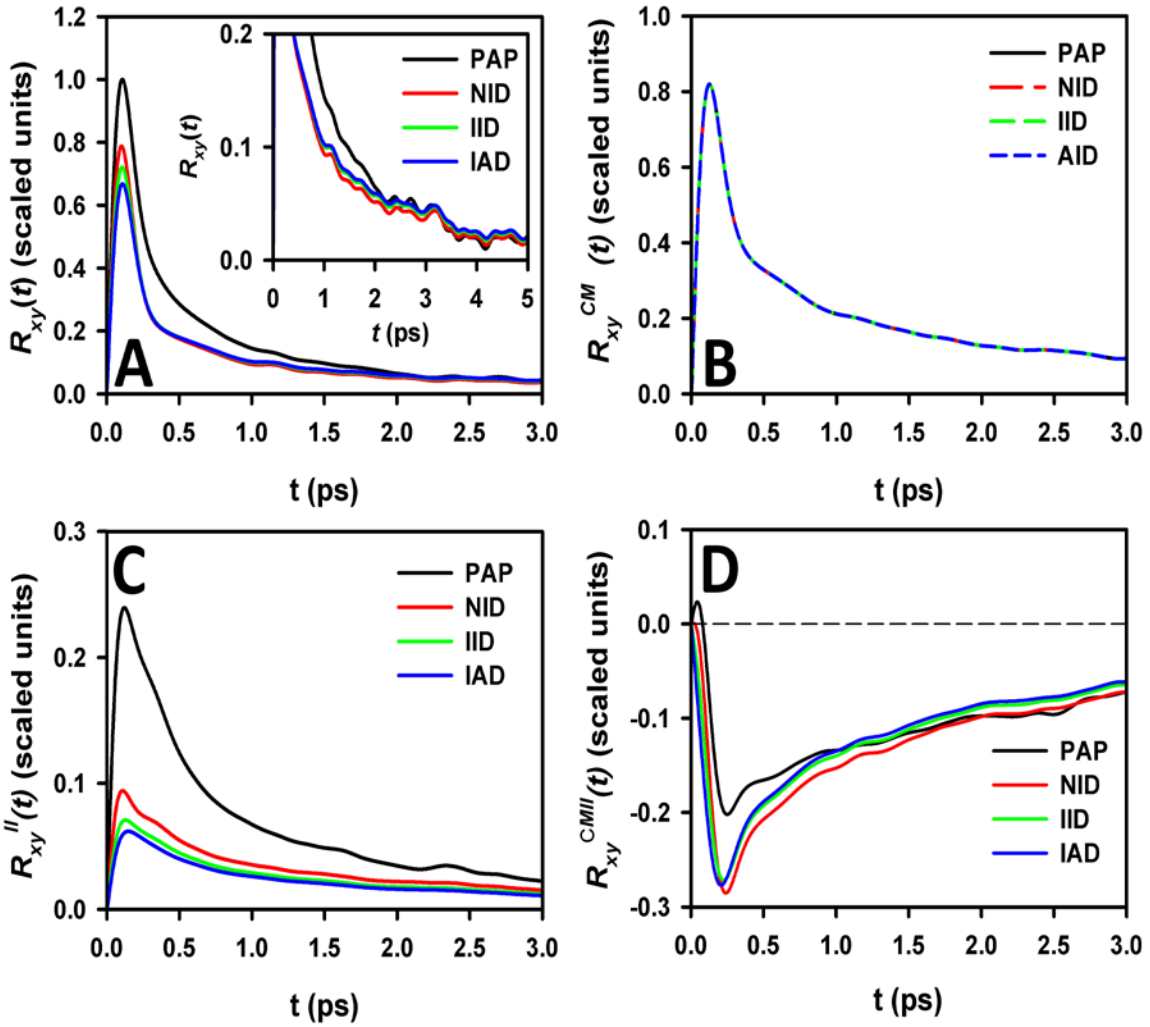

Figure 4.3 Depolarized response functions for the point anisotropic polarizability (black), the non-interacting distributed polarizability (red), the interacting isotropic distributed polarizability (green), and the interacting anisotropic distributed polarizability (blue) models of liquid benzene. (A) Full, (B) collective molecular, (C) interaction-induced, and (D) cross-term response functions. The inset is a zoom-in of the tails of the full response functions.

$R_{xy}^{II}(t)$ peaks at ~100 fs for each polarizability model, and the amplitudes of the peaks and the subsequent diffusive decays decrease as the polarizability becomes more distributed. The height of $R_{xy}^{II}(t)$ for the PAP model is more than double that for the distributed models, which accounts for the difference in the shape of $R_{xy}(t)$ between the PAP model and the distributed models. $R_{xy}^{CM}(t)$ (Figure 4.3B) is identical within the four

models, indicating that the differences in the diffusive portion of $R_{xy}(t)$ arise from $R_{xy}^{CMII}(t)$.

$R_{xy}^{CMII}(t)$ can exhibit complex behavior at times shorter than ~200 fs. The function calculated with the PAP model shows a positive peak at 40 fs. The NID model also shows a smaller peak at 15 fs. The IID and IAD models show no positive peak and the negative portion of the response moves to earlier times as the polarizability model becomes more distributed.

The magnitude of the cross-correlation response functions calculated with the three distributed models is ~38% greater than the magnitude for the PAP function, despite the fact that the interaction-induced contribution in the PAP model is considerably larger than for any of the distributed models. $R_{xy}^{CMII}(t)$ for the three distributed models exhibits the same long-time diffusive behavior as does $R_{xy}(t)$, and the amplitudes of the $R_{xy}^{CMII}(t)$ diffusive tails are substantially larger than those of $R_{xy}^{II}(t)$. These details indicate that the trend in the magnitude diffusive tail of $R_{xy}(t)$ with increasing degree of distribution of the polarizability is the result of the cross-correlation of the orientational dynamics contained within $R_{xy}^{CM}(t)$ and $R_{xy}^{II}(t)$.

4.4.3 *Collective and Interaction-Induced RSDs*

The RSDs corresponding to the decomposed response functions are shown in Figure 4.4. Each RSD has been scaled to the maximum value of the total polarizability $I^*(\bar{\nu})$ for the PAP model. The full RSDs are shown in Figure 4.4A. The peak magnitude of $I^*(\bar{\nu})$ for the PAP model is ~50% greater than the peak magnitudes for the remaining three models. The PAP RSD has a triangular shape, peaking at 9 cm^{-1}, whereas the RSDs

of the distributed models have a flatter shape that is more similar to that of the experimental spectrum. The collective molecular RSDs, which are identical to one another, are shown in Figure 4.4B.

The inset of Figure 4.4A shows the same RSDs after scaling to minimize the differences from 75 cm^{-1} to 250 cm^{-1}. It is evident from Figure 4.4A that increasing the degree of distribution of the polarizability model decreases the overall magnitude of the RSD. The inset also reveals that the low-frequency shoulder of the RSD becomes somewhat more prominent as the polarizability becomes more distributed. The interaction-induced portions of the RSDs, which are plotted in Figure 4.4C, show the same trend in overall magnitude as do the total RSDs. The interaction-induced portion of the PAP RSD is over 50% larger than those for the distributed models, which is the major source of the difference in shape of the total RSD for the PAP model. The inset of Figure 4.4C shows the interaction-induced portion of the RSDs scaled as in the inset to Figure 4.4A. All of the interaction-induced contributions have similar shapes, and it is evident that the greater sharpness of the peak in the interaction-induced RSDs for the more distributed polarizability models accounts for the behavior seen in the inset of Figure 4.4A.

Figure 4.4D shows the cross-correlation between the collective molecular and interaction-induced portions of the RSDs for the different polarizability models. The PAP RSD has a small positive peak at 4.5 cm^{-1}, whereas the interaction-induced RSDs for the distributed models do not. The distributed models exhibit the typical behavior for the cross-correlation RSD, being negative at low frequencies and becoming positive at higher frequencies before tending to zero. For each model there is a small, broad, positive-going

peak at ~100 cm^{-1}. The amplitude of this peak decreases as the polarizability becomes more distributed. The data in the inset further support the idea that the interaction-induced contribution is responsible for the low-frequency shoulder seen in the total spectra.

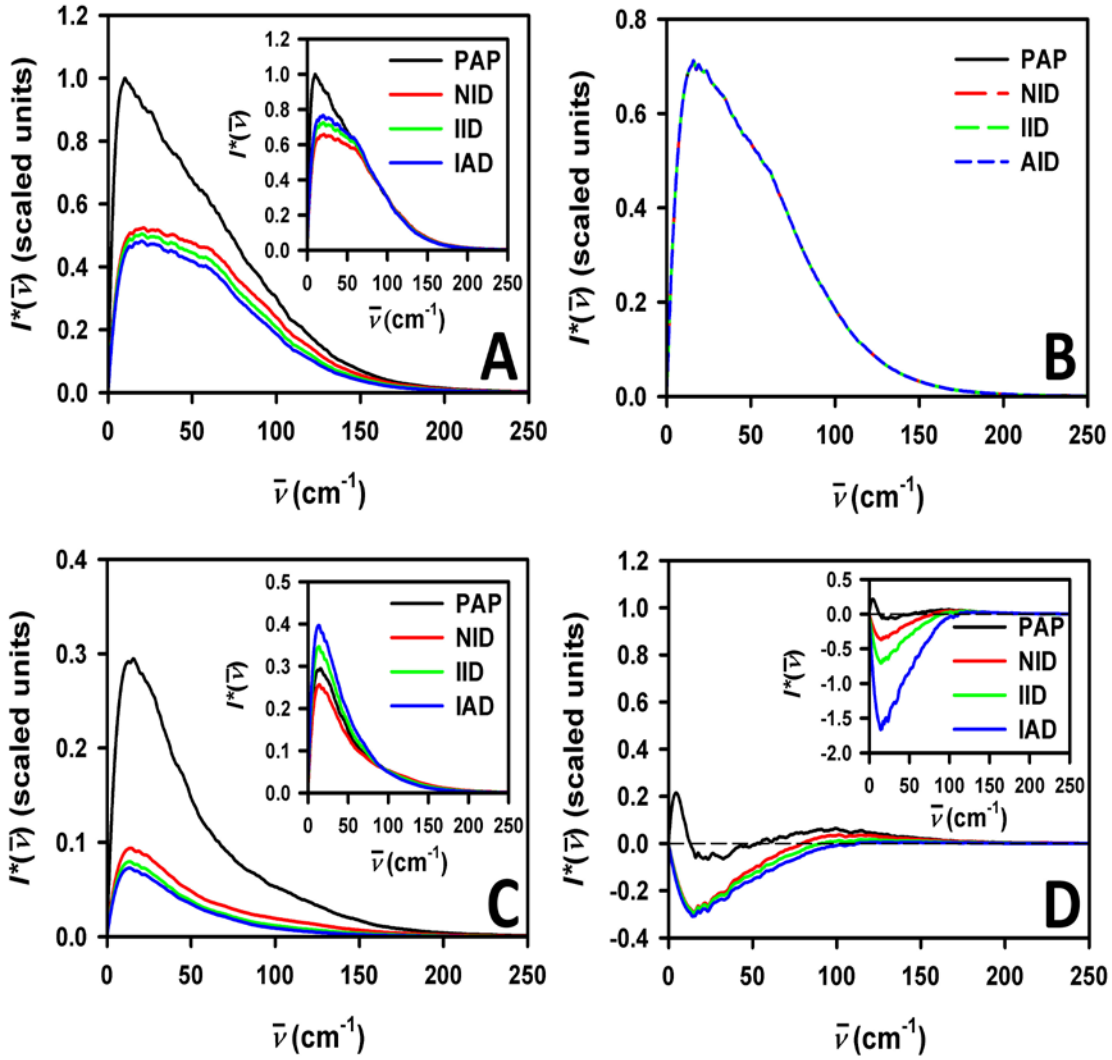

Figure 4.4 Depolarized RSDs for the point anisotropic polarizability (black), the non-interacting distributed polarizability (red), the interacting isotropic distributed polarizability (green), and the interacting anisotropic distributed polarizability (blue) models of liquid benzene. (A) Full, (B) collective molecular, (C) interaction-induced, and (D) cross-term RSDs. The RSDs in the insets are scaled for the best match from 75 cm^{-1} to 250 cm^{-1}.

4.4.4 *Reorientational and Collision-Induced Correlation Functions*

The projected depolarized TCFs corresponding to eq 4.6 are shown in Figure 4.5. The functions for the PAP, NID, IID, and IAD models are shown in panels A, B, C, and D, respectively. $C_{xy}^{R}(t)$ is the major component of the TCFs, and closely tracks $C_{xy}(t)$. The $C_{xy}^{R}(t)$ diffusive decay constants are the same for each model. $C_{xy}^{CI}(t)$ contributes to $C_{xy}(t)$ at early times, but this TCF decays much faster than does $C_{xy}^{R}(t)$. The amplitude of $C_{xy}^{CI}(t)$ is small for each polarizability model. The PAP collision-induced TCF has the largest amplitude, and the amplitude of this portion of the TCF decreases as the polarizability becomes more distributed. $C_{xy}^{RCI}(t)$ follows the same amplitude trend as does the collision-induced function, but decays more slowly with time. The amplitudes of the cross-term TCFs are small, indicating that the reorientational and collision-induced contributions are not highly correlated.

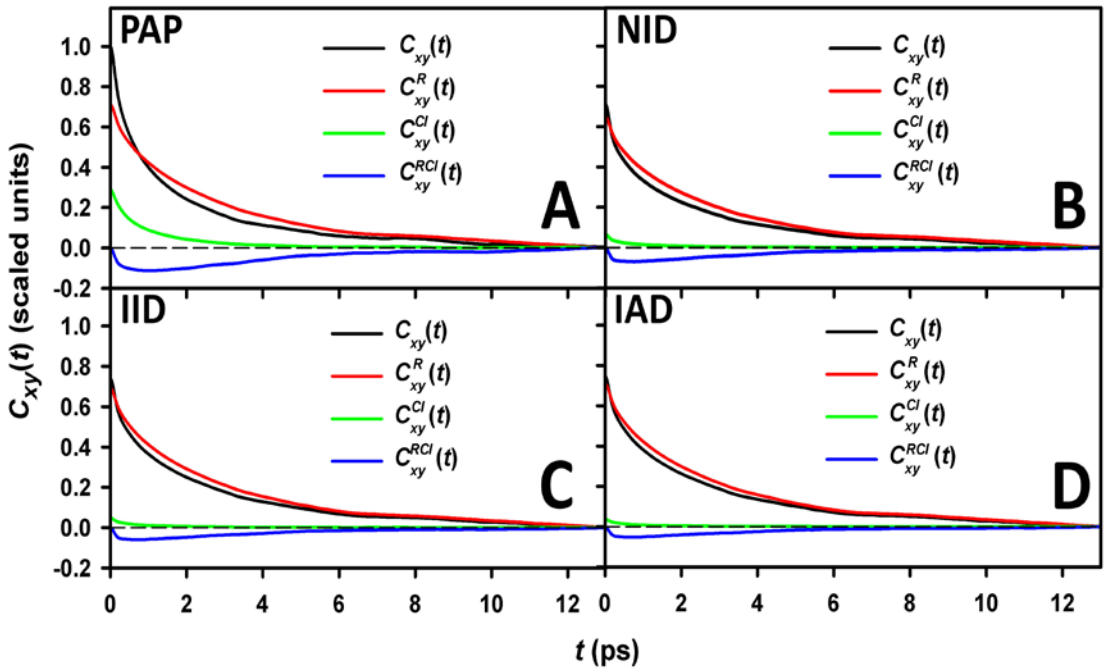

Figure 4.5 Full (black), reorientational (red), collision-induced (green), and cross-term (blue) depolarized, many-body polarizability TCFs for (A) the point anisotropic polarizability, (B) the non-interacting distributed polarizability, (C) the interacting isotropic distributed polarizability, and (D) the interacting anisotropic distributed polarizability models of liquid benzene.

The TCFs were fit to a single-exponential function for the subsequent removal of any diffusive contributions to the TCFs. Table 4.3 shows the fit parameters for the diffusive contributions to $C_{xy}(t)$, $C_{xy}^{R}(t)$, and $C_{xy}^{CI}(t)$.

Table 4.3 Amplitudes (A) and Time Constants (τ) from Exponential Fits to the Diffusive Portion of the Total, Reorientational, and Collision-Induced TCFs[a]

	$C_{xy}(t)$		$C_{xy}^{R}(t)$		$C_{xy}^{CI}(t)$	
	A	**τ (ps)**	**A**	**τ (ps)**	**A**	**τ (ps)**
PAP	0.295(6)	3.23(8)	0.396(2)	3.18(4)	0.083(3)	1.88(6)
NID	0.291(2)	3.17(7)	0.360(1)	3.18(3)	0.017(1)	1.8(2)
IID	0.324(2)	3.17(7)	0.385(2)	3.18(3)	0.013(1)	1.8(2)
IAD	0.343(2)	3.17(7)	0.395(2)	3.18(4)	0.010(1)	1.7(2)

[a]Numbers in parentheses are uncertainties in the last digit

4.4.5 *Reorientational and Collision-Induced Response Functions*

The projected depolarized OKE response functions calculated using the four polarizability models are shown in Figure 4.6. $R_{xy}(t)$, $R_{xy}^{R}(t)$, $R_{xy}^{CI}(t)$, and $R_{xy}^{RCI}(t)$ are shown in panels A, B, C, and D, respectively. $R_{xy}(t)$ was discussed in Section 4.4.2, but is shown again for convenience to compare/contrast the contributions of the collision-induced and cross-term responses to the total response. $R_{xy}^{R}(t)$ for the four models is shown in Figure 4.6B. The response functions have been scaled to the maximum value of $R_{xy}(t)$ for the PAP model.

$R_{xy}^{CI}(t)$ peaks at ~100 fs for all of the models, and the amplitude of the peak decreases as the polarizability becomes more distributed. The peak amplitude of the PAP response is more than 50% greater than those of the NID, IID, and IAD models. The shape of the PAP response is considerably different from those of the distributed models,

and the difference in shape of the collision-induced responses is the major contributor to the difference in shape of the total polarizability responses.

$R_{xy}^{RCI}(t)$ also peaks at ~100 fs for each model and displays the same trend in amplitude as does $R_{xy}^{CI}(t)$. The shapes of these portions of the response are comparable. These similarities, combined with the similarity of the reorientational responses for each polarizability model, indicate that the major differences in the dynamics captured by each of the polarizability models can be related to collision-induced effects.

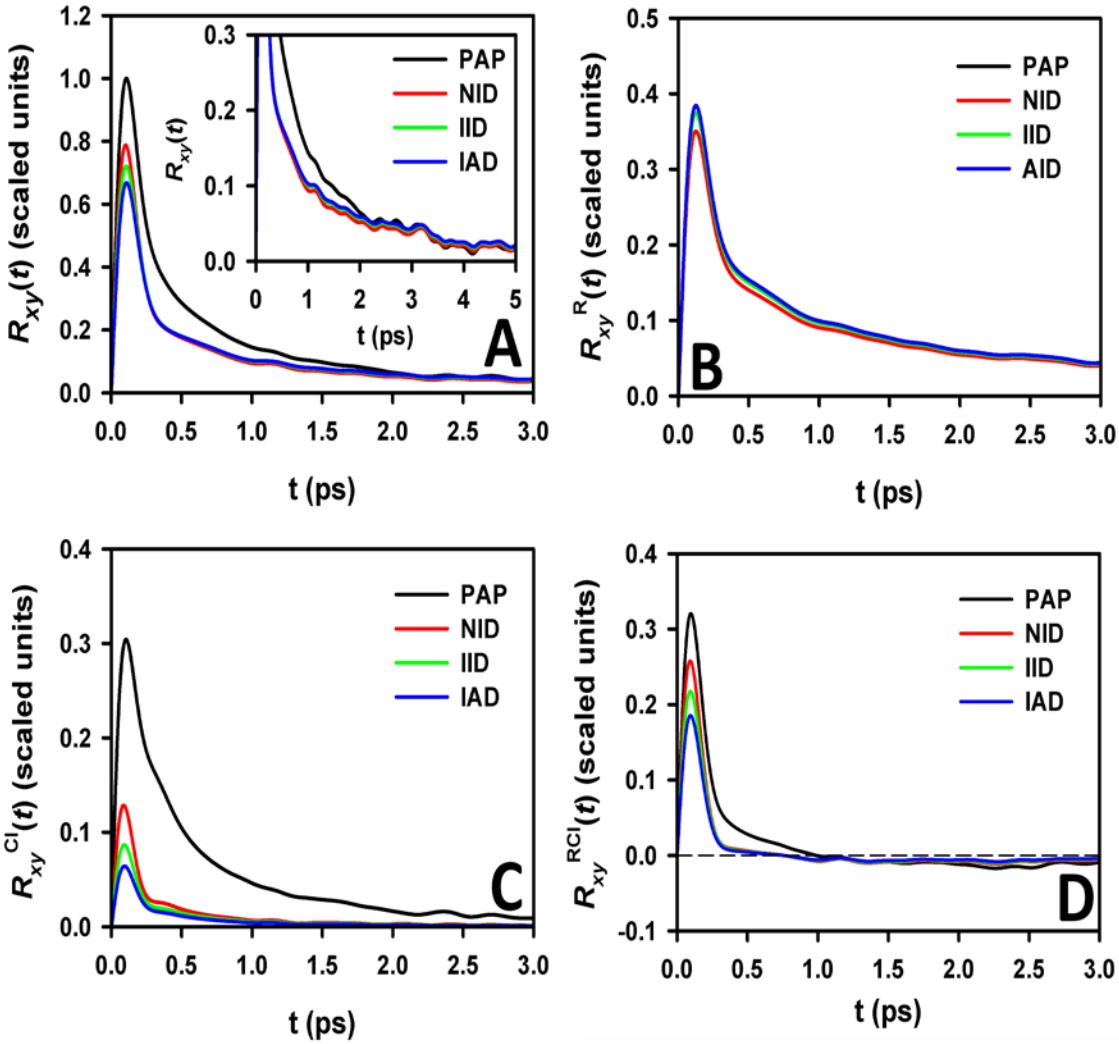

Figure 4.6 Depolarized response functions for the point anisotropic polarizability (black), the non-interacting distributed polarizability (red), the interacting isotropic distributed polarizability (green), and the interacting anisotropic distributed polarizability (blue) models of liquid benzene. (A) Full, (B) reorientational, (C) collision-induced, and (D) cross-term response functions. The inset is a zoom-in of the tails of the full response functions.

4.4.6 *Reorientational and Collision-Induced RSDs*

The RSDs of the projected response functions are shown in Figure 4.7. The total, reorientational, collision-induced, and the cross-term RSDs are shown in panels A, B, C, and D, respectively. Each RSD has been scaled to the maximum amplitude of the PAP total polarizability RSD. Figure 4.7A shows the total polarizability RSDs, which were discussed in Section 4.4.3 and are shown here again for convenience.

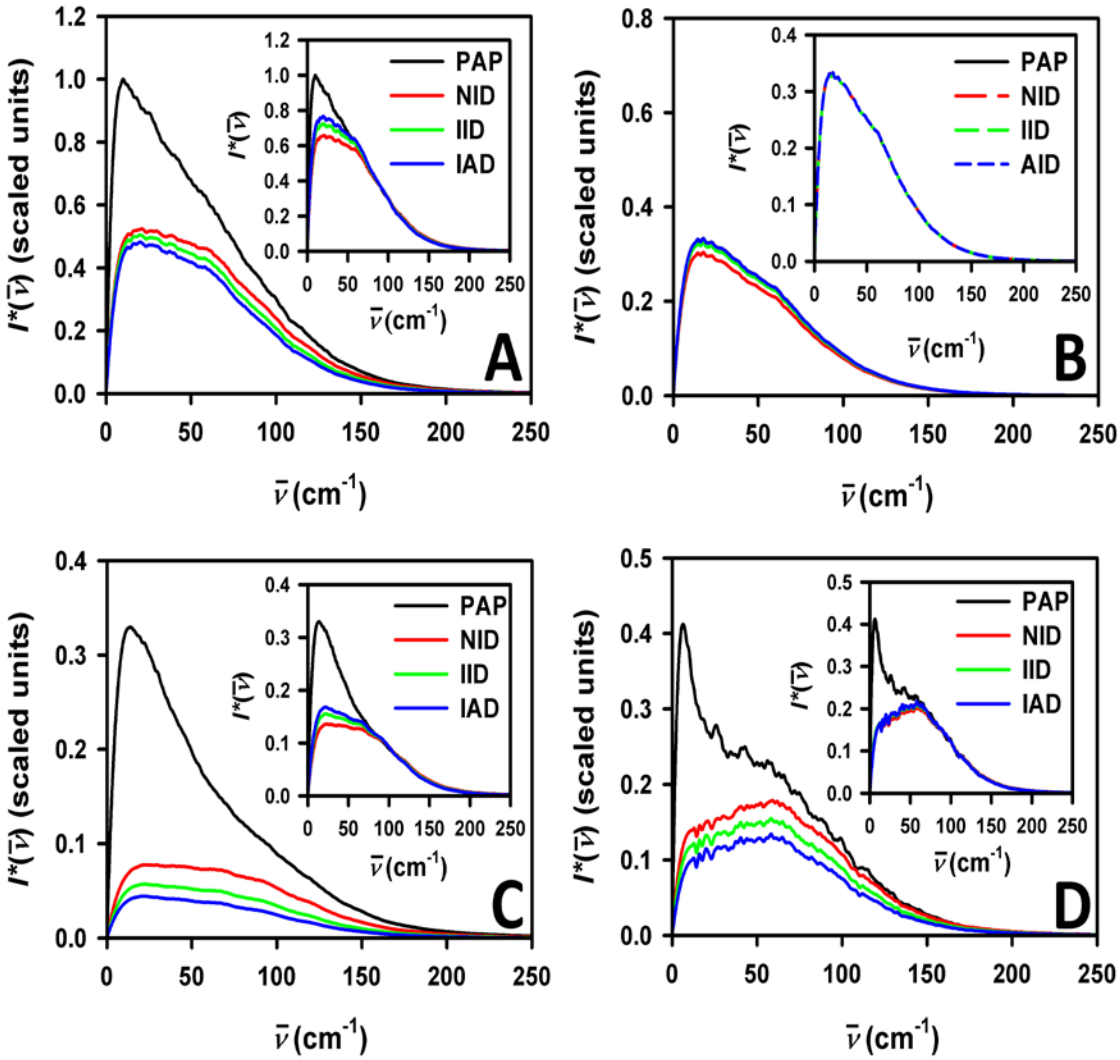

Figure 4.7 Depolarized RSDs for the point anisotropic polarizability (black), the non-interacting distributed polarizability (red), the interacting isotropic distributed polarizability (green), and the interacting anisotropic distributed polarizability (blue) models of liquid benzene. (A) Full, (B) reorientational, (C) collision-induced, and (D) cross-term RSDs. The RSDs in the insets are scaled for the best match from 75 cm^{-1} to 250 cm^{-1}.

Figure 4.7C shows the collision-induced portions of the RSDs. Here again the PAP spectrum is remarkably different from the spectra of the remaining three models. The PAP RSD has a magnitude that is more than three times greater than that of the NID, IID, and IAD RSDs. The PAP collision-induced RSD peaks at 14.4 cm^{-1}, whereas the remaining three spectra are broad and take on a flattened shape. The amplitude of the collision-induced contribution to the RSD decreases with increasing distribution of the polarizability. The inset in Figure 4.7C shows the scaled RSDs, highlighting the disparity in spectral shape. The NID collision-induced RSD has the most flattened shape, and the trend seen in the scaled total polarizability spectrum is the same.

The collision-induced/reorientational cross correlation spectra are shown in Figure 4.7D. The same trend in magnitude is found: the PAP spectrum has the highest amplitude, and the amplitude decreases as the polarizability becomes more distributed. The RSD for the PAP model is again shaped differently than the three other RSDs, with a peak at 6.7 cm^{-1}. The NID, IID, and IAD RSDs lack this peak. Otherwise, the RSDs for the distributed models have exactly the same shape, as shown in the inset of Figure 4.7D.

4.4.7 *AMPT Approximation*

Hu *et al.* have shown that for an ionic liquid, the AMPT approximation does an excellent job of reproducing $C_{xy}(t)$ and $R_{xy}(t)$ as calculated with full inversion, slightly underestimating the former quantity and slightly overestimating the latter.[32] However, they did not test how well the AMPT approximation reproduces spectra computed with the full-inversion method. In addition, benzene differs considerably from an ionic liquid, and so it is worthwhile to explore how well the AMPT approximation works for a liquid composed of neutral molecules.

To test the AMPT approximation against the full-inversion method for speed and accuracy, the analysis presented in Sections 4.4.1 through 4.4.6 was performed once more for each distributed model, this time using the AMPT algorithm. The calculated quantities are essentially identical whether the full-inversion method or the AMPT approximation is used. For instance, Figure 4.8 shows the total polarizability NID RSDs simulated using the full-inversion method (black) and the AMPT approximation (red). The RSDs exhibit the same spectral shape (shown in the inset); however, the AMPT RSD has a slightly larger amplitude. This amplitude difference most likely results from the fact that the AMPT method calculates the site-to-site polarizability interactions only in molecular pairs, excluding site-to-site many-body effects among three or more molecules.

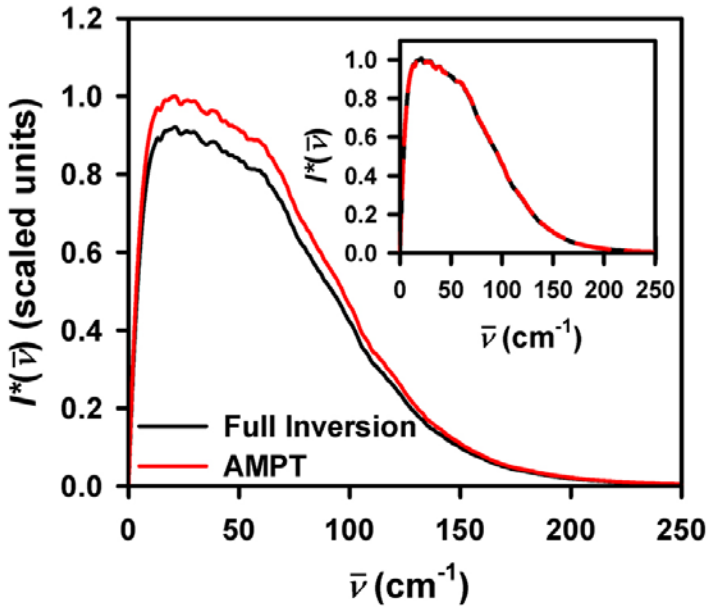

Figure 4.8 Comparison of the depolarized RSD calculated with the non-interacting distributed model with full inversion (black) and with the AMPT approximation (red). The RSDs in the inset have been scaled in amplitude to minimize their root-mean-square differences.

Table 4.4 shows the system CPU times for the calculation of the liquid polarizability of one MD simulation configuration for each of the polarizability models using both the full-inversion and AMPT methods. As expected, the PAP model is the

fastest. The AMPT method is about five times faster than the full-inversion method when the NID model is used, and is three times faster when the IID model is used. The IAD model is the slowest in both the full-inversion and AMPT methods.

Table 4.4 System CPU Times (t) for Polarizability Calculation for a Single Configuration[a]

	Full-Inversion	AMPT
	t **(s)**	***t*** **(s)**
PAP	0.050(6)	N/A
NID	14.3(2)	2.9(1)
IID	15.0(2)	4.1(1)
IAD	15.1(2)	11.0(1)

[a]Numbers in parentheses are uncertainties in the last digit.

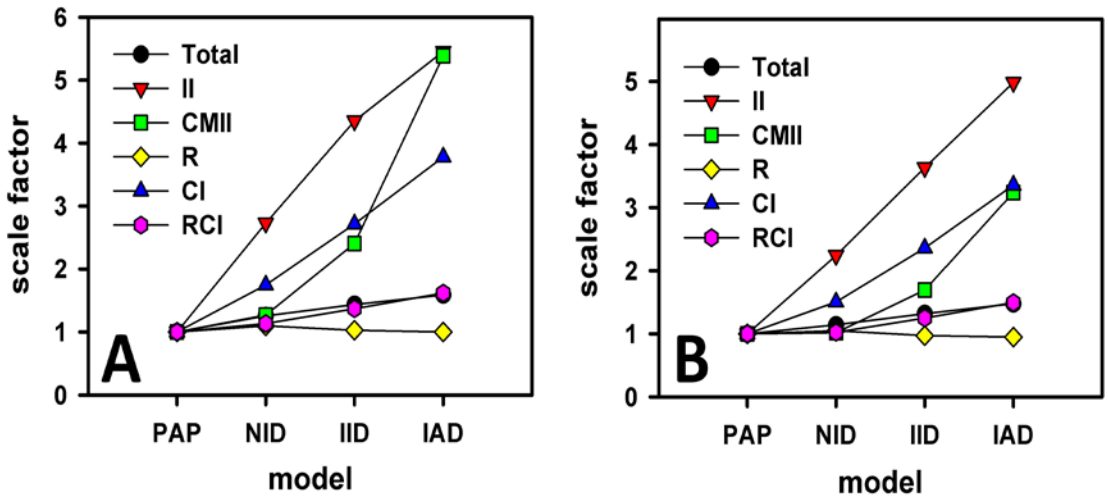

Figure 4.9 Scaling factors that best match the RSDs from 75 cm^{-1} to 250 cm^{-1} for (A) full inversion and the (B) AMPT approximation for each of the models examined here.

Figure 4.9 shows the scaling factors of the insets of Figures 4.4 and 4.7 for both the full-inversion and AMPT methods of calculating the polarizability. Again, the AMPT method gives essentially the same results for each of the polarizability models, i.e. the intensity of each spectrum decreases as the polarizability model becomes more distributed.

4.4.8 *Comparison of Simulation and Experiment*

Figure 4.10A compares the simulated (NID model) and experimental response functions and Figure 4.10B compares the simulated and experimental RSDs. In both cases the simulation is in good agreement with experiment, although the recurrence feature evident in the experimental response at ~450 fs is not apparent in the simulated response. The simulated RSD covers the same frequency range as the experimental spectrum, which is indicative of the accuracy of the intermolecular interactions captured by the potential developed by Bonnaud *et al*. The simulated spectrum does not have as much of a flattened top as does the experimental spectrum, indicating that the simulated spectrum either slightly overemphasizes modes at lower frequencies or slightly underemphasizes modes at higher frequencies.

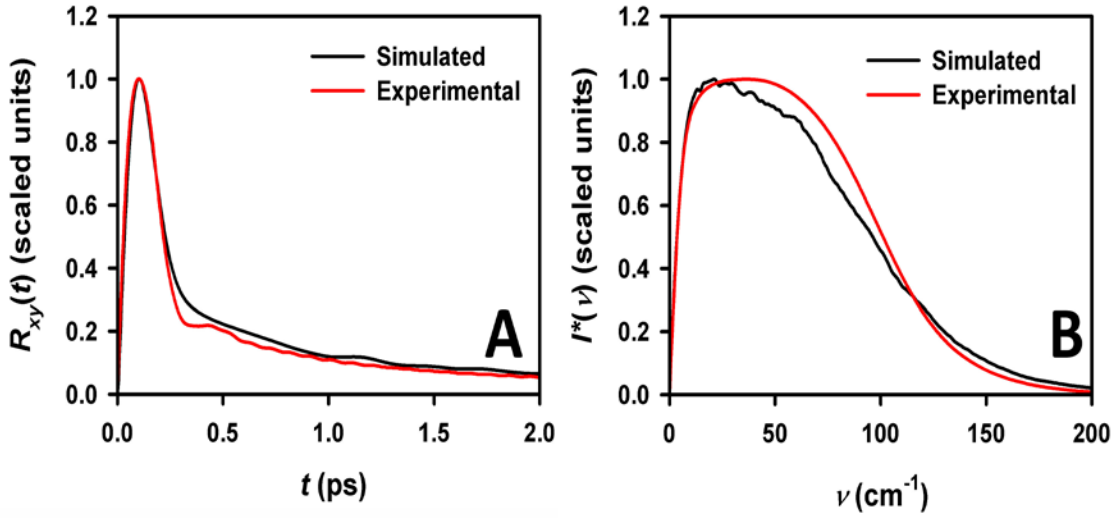

Figure 4.10 Normalized depolarized response functions (A) and RSDs (B) for the simulations using the NID model (black) and from experiment (red).

As a further test of the Bonnaud potential, we compare its predictions to experimentally measureable pair correlation parameters. The ratio of the collective

orientational correlation time τ_c to the single-molecule orientational correlation time τ_s is given by

$$\frac{\tau_c}{\tau_s} = \frac{g_2}{j_2}, \tag{4.9}$$

where g_2 is the static orientational pair correlation parameter and j_2 is the dynamic orientational pair correlation parameter.[44] Based on our calculation of $C_{xy}^{SM}(t)$ (Figure 4.11), we find that τ_s is 2.82 ps. In conjunction with the 3.20 ps value of τ_c (see Table 4.2), we find that g_2/j_2 is 1.13. We note that the decay time of $C_{xy}(t)$, which is what is measured experimentally, is 3.17 ps, which yields a value of 1.12 for g_2/j_2. Both values are in good agreement with experiment,[24] and compare favorably to the value of 1.38 determined using the Williams potential.[18] Additionally, g_2 is given by the initial value of the collective molecular TCF:[5]

$$g_2 = C_{xy}^{CM}(0)\,. \tag{4.10}$$

Based on our simulations, this value is 1.08, which is in good agreement with the experimentally determined value of 1.16±0.12.[45] We therefore conclude that the combination of the Bonnaud potential and any of the distributed polarizability models tested here does an excellent job in reproducing the low-frequency Raman spectrum of benzene.

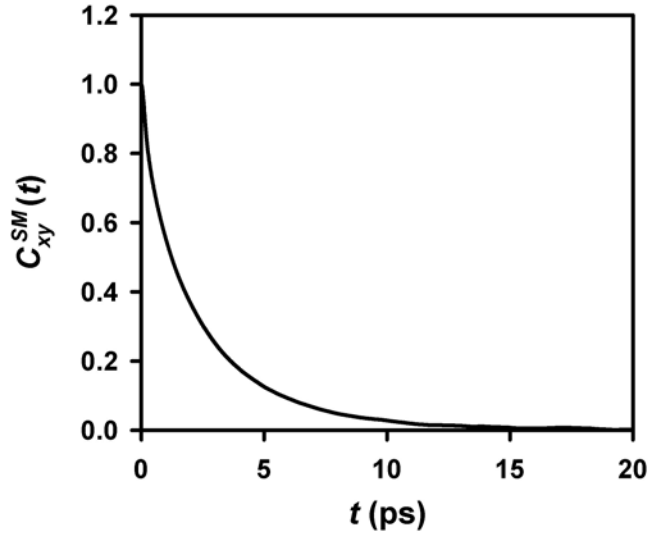

Figure 4.11 The depolarized, single-molecule polarizability TCF for benzene calculated with the Bonnaud potential.

4.5 *Discussion*

4.5.1 *Point Polarizability Models versus Distributed Models*

One striking result of our comparisons is that calculations performed with the PAP model differ considerably from those performed using the distributed models. For instance, many-body polarizability TCFs, response functions, and spectral densities calculated using the PAP model have significantly greater amplitudes than those calculated with the distributed models. Surprisingly, even the collective orientational correlation time determined from the many-body polarizability TCF for the PAP model differs somewhat from those determined from the other models.

The data in Figures 4.2 through 4.4 highlight the increased importance of interaction-induced effects in the PAP model as compared to the distributed models, which accounts for most of the differences observed in the TCFs, response functions and

RSDs between the two types of model. The greater amplitude of interaction-induced effects in the PAP model is a consequence of having the polarizability localized at the center of a relatively large molecule. This geometry makes it difficult for two polarizable sites to approach one another closely. It is even rarer for one polarizable site to be near to two others. Thus, the interaction-induced portion of the many-body polarizability is dominated by two-body interactions in the PAP model. Three-body interactions typically have the effect of decreasing the many-body polarizability,[46] and their absence causes the interaction-induced contribution to this polarizability to be unrealistically large.

The PAP model also tends to overemphasize the contribution of fluctuations in distance in the interaction-induced contribution to the many-body polarizability. The polarizable sites on two different molecules are closest to one another, and therefore have the largest interaction, when the molecules are face-to-face. However, in this geometry tumbling reorientation of the molecules relative to one another is difficult, whereas translation can occur with relative ease.

The manifestations of this behavior are clear in Figures 4.5 through 4.7. For instance, the magnitudes of the collision-induced term and the reorientation/collision-induced cross term in the PAP TCF are much greater than for any of the distributed models. This behavior indicates that in the PAP model, many-body polarizability dynamics that are orthogonal to those of reorientation are considerably more important than in the other models. Translation presumably plays a major role in these orthogonal dynamics.

The differences in interaction-induced effects in the PAP model are also responsible for the small difference in the PAP collective orientational correlation time

compared to those of the distributed models. Although the contribution of diffusive reorientation to the OKE signal depends primarily on the orientations of individual molecular polarizability tensors, the overall magnitude of the contribution of diffusive reorientation is modulated by the interaction-induced polarizability. As can be seen in Figure 4.5, for the distributed polarizability models the vast majority of the influence of interaction-induced effects on the diffusive reorientation contribution to the signal has dynamics that match those of the reorientation itself (i.e., the collision-induced and reorientation/collision-induced cross-term contributions to the overall TCF are quite small, particularly at the longer delay times when the TCF is dominated by diffusive reorientation). In the PAP model, the cross-term contribution remains substantial even at long delay times. Because this cross term arises in part from polarizability dynamics that are orthogonal to those of reorientation, it has a somewhat different decay time than does the reorientational contribution to the TCF, leading to the difference in the overall orientational correlation time.

Our overall conclusion from this analysis is that although PAP models are computationally attractive, in large enough molecules they are prone to cause undesired distortions in time- and frequency-domain functions of the many-body polarizability. It may still be appropriate to use such models in some circumstances, so long as one has a clear picture of where the calculated quantities are likely to differ from those calculated with a more realistic polarizability model.

4.5.2 *Comparison of Distributed Models*

We next compare the distributed models with one another. It is evident from the data in Figures 4.2 through 4.4 that increasing the degree of distribution of the

polarizability leads to a modest decrease in the overall amplitude of the TCFs, the response functions and the RSDs. This phenomenon reflects the increased importance of three-body effects as the polarizability becomes more distributed.

Perhaps the most surprising feature of this comparison is that the time and frequency dependence of all of the quantities we have calculated is virtually unaffected in going from the NID model to the more distributed IID and IAD models. We observe slight changes in the interaction-induced and collision-induced portions of quantities and the cross terms that involve them, but to a good approximation the shapes of the TCFs, response functions and RSDs (and their decompositions) are independent of the distributed model used.

From a physical perspective, the similarities of the results for the three models suggest that all of these models capture the important aspects of three-body interactions in determining the many-body polarizability dynamics of the liquid. Indeed, it has been shown previously that the polarizability of liquid benzene is dominated by first-order interaction-induced effects.[18,25] From a practical perspective, using the somewhat more computationally efficient NID model is not likely to result in any significant loss in accuracy for this system.

4.5.3 *AMPT versus Full-Inversion Methods*

Another key result of our comparisons is that when the AMPT approximation is used in conjunction with any of the distributed polarizability models, the TCFs, response functions and RSDs (as well as their decompositions) are virtually identical except for a change in amplitude. As discussed above, the AMPT approximation treats the polarizability interactions between pairs of molecules at the atomic level and interactions

among more than two molecules at the molecular level. The success of the AMPT method indicates that the essential form of three-molecule interactions is captured by this approximation. This result is consistent with the relatively minor differences among the distributed polarizability models studied here, which indicates that the ability to capture three-molecule interactions is sufficient to determine the shapes of polarizability TCFs, response functions and RSDs, but not their absolute magnitudes. The AMPT approximation slightly underestimates the importance of three-molecule effects because the center-to-center distance between molecules is greater than or equal to the distance between the closest atoms of those molecules.

From a practical standpoint, the ability of the AMPT approximation to produce accurate shapes for TCFs, response functions and RSDs provides a substantial computational advantage. The absolute magnitudes of these quantities are difficult to determine experimentally, and so it is their dependence on time or frequency that is generally of the greatest interest. In the case of the NID model, use of the AMPT approximation affords a time savings of nearly a factor of 5 in our system with no loss of information regarding the temporal response or the spectral shape.

4.5.4 *Interplay Between the Simulation Potential and the Polarizability Model*

As noted above, the PAP model yields results that differ considerably from those of the distributed models. Interestingly, our PAP results also differ substantially from those of Elola and Ladanyi and those of Ryu and Stratt.[18,25-27] Similarly, the NID results of Elola and Ladanyi differ significantly from ours. Both of these groups used the Williams[47,48] molecular potential for benzene in their simulations, whereas we have employed the Bonnaud potential.[33] The difference in results with respect to the potential

model indicates that the choice of molecular potential can have a profound effect on the simulated spectrum.

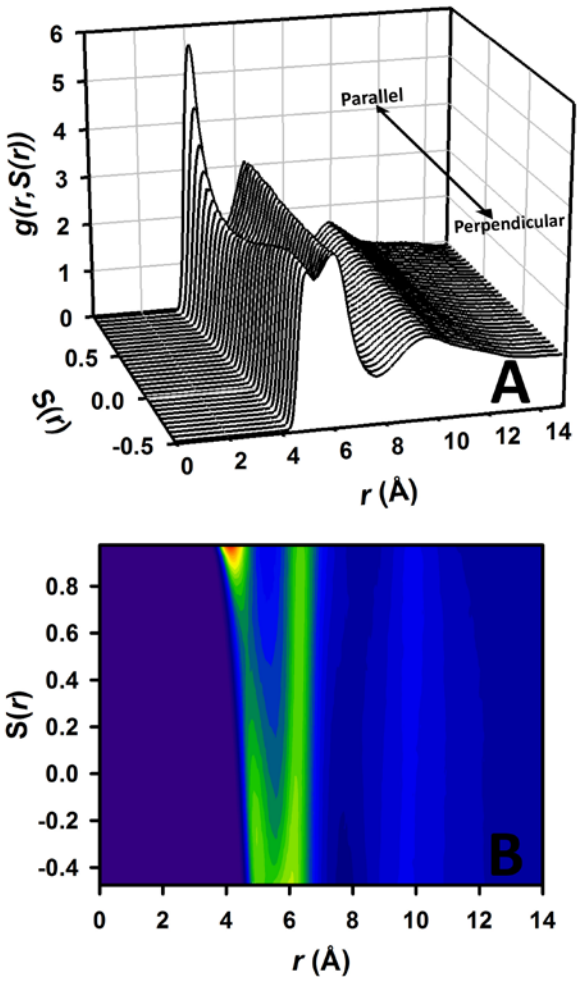

Figure 4.12 (A) Local structure $g(r,S(r))$ and (B) contour plot of $g(r,S(r))$ of benzene liquid simulated with the potential used here.

Many-body polarizability dynamics depend not only on the dynamics of the molecules in a system, but also on the local structure. Thus, realistic simulations of the many-body polarizability must employ a potential that captures both of these aspects of the liquid accurately. Figure 4.12A shows the center-to-center radial distribution function of liquid benzene as a function of the angle between the molecules. The angle is

expressed in terms of $S(r)$, which is given by $\langle \frac{3}{2} cos^2\theta - \frac{1}{2} \rangle$, where θ is the angle between the vectors normal to the planes of the molecules. Parallel vectors give $S(r) = 1$, whereas perpendicular vectors give $S(r) = -0.5$. Figure 4.12B gives a top-down contour plot of the radial distribution function. The potential employed here was optimized to reproduce the carbon-carbon radial distribution function and a number of dynamic quantities,[33] and it predicts significantly enhanced populations of nearest neighbors that are parallel at distances shorter than 4.7 Å and perpendicular at separations between 4.7 Å and 6 Å. The liquid structure becomes isotropic at distances longer than 6 Å. In contrast, in the Williams potential there is a slight preference for parallel nearest neighbors at distances shorter than 5 Å, with all other configurations having nearly equal probability at longer distances.[26] These structural distinctions lead to a substantial difference in the dependence of the many-body polarizability on time and frequency, particularly in the case of the PAP model.

4.6 *Conclusions*

We have presented an MD study comparing/contrasting the depolarized OKE RSD of benzene calculated with four different polarizability models. The type of center-of-mass, point anisotropic molecular polarizability model that has often been employed in simulations of the low-frequency Raman spectrum is insufficient for describing the liquid polarizability for the molecular potential used in our simulations. This type of model is likely to overemphasize the contribution of interaction-induced scattering in most molecular liquids. The simplest of three distributed polarizability models tested yields low-frequency Raman spectra for benzene that differ little from those calculated using more sophisticated distributed models, other than having a different overall magnitude.

This result indicates that, at least for this system, the important physics of many-body interactions among molecules is captured simply by having multiple polarizable sites within the molecules, even if the sites within a given molecule are not allowed to interact with one another.

We have also shown that the AMPT approximation developed by Hu *et al.*[32] yields spectra that are identical in shape to those computed with the full-inversion method, while allowing for considerably more efficient computation of these spectra. The combination of AMPT with a simple distributed polarizability model is a promising approach for the efficient computation of many-body polarizability dynamics in liquids. It will be of great interest to test the generality of this approach by applying it to simulations of the OKE spectra of other liquids.

4.7 *References*

(1) Zhong, Q.; Fourkas, J. T. Optical Kerr Effect Spectroscopy of Simple Liquids. *J. Phys. Chem. B* **2008**, *112*, 15529-15539.

(2) Hunt, N. T.; Jaye, A. A.; Meech, S. R. Ultrafast Dynamics in Complex Fluids Observed Through the Ultrafast Optically-Heterodyne-Detected Optical-Kerr-Effect (OHD-OKE). *Phys. Chem. Chem. Phys.* **2007**, *9*, 2167-2180.

(3) Righini, R. Ultrafast Optical Kerr-Effect in Liquids and Solids. *Science* **1993**, *262*, 1386-1390.

(4) McMorrow, D.; Lotshaw, W. T. Intermolecular Dynamics in Acetonitrile Probed with Femtosecond Fourier-Transform Raman-Spectroscopy. *J. Phys. Chem.* **1991**, *95*, 10395-10406.

(5) Madden, P. A.; Tildesley, D. J. Interaction-Induced Contributions to Rayleigh and Allowed Raman Bands - a Simulation Study of CS_2. *Mol. Phys.* **1985**, *55*, 969-998.

(6) Geiger, L. C.; Ladanyi, B. M. Higher-Order Interaction-Induced Effects on Rayleigh Light-Scattering by Molecular Liquids. *J. Chem. Phys.* **1987**, *87*, 191-202.

(7) Bardak, F.; Xiao, D.; Hines, L. G.; Son, P.; Bartsch, R. A.; Quitevis, E. L.; Yang, P.; Voth, G. A. Nanostructural Organization in Acetonitrile/Ionic Liquid Mixtures: Molecular Dynamics Simulations and Optical Kerr Effect Spectroscopy. *Chemphyschem* **2012**, *13*, 1687-1700.

(8) Manfred, K.; He, X. X.; Fourkas, J. T. Assessing the Role of Moment of Inertia in Optical Kerr Effect Spectroscopy. *J. Phys. Chem. B* **2010**, *114*, 12096-12103.

(9) Ricci, M.; Bartolini, P.; Chelli, R.; Cardini, G.; Califano, S.; Righini, R. The Fast Dynamics of Benzene in the Liquid Phase - Part I. Optical Kerr Effect Experimental Investigation. *Phys. Chem. Chem. Phys.* **2001**, *3*, 2795-2802.

(10) Elola, M. D.; Ladanyi, B. M. Polarizability Response in Polar Solvents: Molecular-Dynamics Simulations of Acetonitrile and Chloroform. *J. Chem. Phys.* **2005**, *122*, 224506.

(11) Chelli, R.; Cardini, G.; Ricci, M.; Bartolini, P.; Righini, R.; Califano, S. The Fast Dynamics of Benzene in the Liquid Phase - Part II. A Molecular Dynamics Simulation. *Phys. Chem. Chem. Phys.* **2001**, *3*, 2803-2810.

(12) Chelli, R.; Cardini, G.; Procacci, P.; Righini, R.; Califano, S.; Albrecht, A. Simulated Structure, Dynamics, and Vibrational Spectra of Liquid Benzene. *J. Chem. Phys.* **2000**, *113*, 6851.

(13) Loughnane, B. J.; Scodinu, A.; Fourkas, J. T. Temperature-Dependent Optical Kerr Effect Spectroscopy of Aromatic Liquids. *J. Phys. Chem. B* **2006**, *110*, 5708-5720.

(14) Zhong, Q.; Fourkas, J. T. Shape and Electrostatic Effects in Optical Kerr Effect Spectroscopy of Aromatic Liquids. *J. Phys. Chem. B* **2008**, *112*, 15342-15348.

(15) Zhu, X.; Farrer, R. A.; Fourkas, J. T. Ultrafast Orientational Dynamics of Nanoconfined Benzene. *J. Phys. Chem. B* **2005**, *109*, 12724-12730.

(16) Neelakandan, M.; Pant, D.; Quitevis, E. L. Reorientational and Intermolecular Dynamics in Binary Liquid Mixtures of Hexafluorobenzene and Benzene: Femtosecond Optical Kerr Effect Measurements. *Chem. Phys. Lett.* **1997**, *265*, 283-292.

(17) Rajian, J. R.; Hyun, B. R.; Quitevis, E. L. Intermolecular Spectrum of Liquid Biphenyl Studied by Optical Kerr Effect Spectroscopy. *J. Phys. Chem. A* **2004**, *108*, 10107-10115.

(18) Elola, M. D.; Ladanyi, B. M.; Scodinu, A.; Loughnane, B. J.; Fourkas, J. T. Effects of Molecular Association on Polarizability Relaxation in Liquid Mixtures of Benzene and Hexafluorobenzene. *J. Phys. Chem. B* **2005**, *109*, 24085-24099.

(19) Ricci, M.; Wiebel, S.; Bartolini, P.; Taschin, A.; Torre, R. Time-Resolved Optical Kerr Effect Experiments on Supercooled Benzene and Test of Mode-Coupling Theory. *Philos. Mag.* **2004**, *84*, 1491-1498.

(20) Heisler, I. A.; Meech, S. R. Low-Frequency Isotropic and Anisotropic Raman Spectra of Aromatic Liquids. *J. Chem. Phys.* **2010**, *132*, 174503.

(21) McMorrow, D.; Lotshaw, W. T. Evidence for Low-Frequency ($\approx$15 cm^{-1}) Collective Modes in Benzene and Pyridine Liquids. *Chem. Phys. Lett.* **1993**, *201*, 369-376.

(22) Rønne, C.; Jensby, K.; Loughnane, B. J.; Fourkas, J.; Nielsen, O. F.; Keiding, S. R. Temperature Dependence of the Dielectric Function of C_6H_6(l) and $C_6H_5CH_3$(l) Measured with THz Spectroscopy. *J. Chem. Phys.* **2000**, *113*, 3749-3756.

(23) Farrer, R. A.; Loughnane, B. J.; Deschenes, L. A.; Fourkas, J. T. Level-Dependent Damping in Intermolecular Vibrations: Linear Spectroscopy. *J. Chem. Phys.* **1997**, *106*, 6901-6915.

(24) Loughnane, B. J.; Scodinu, A.; Farrer, R. A.; Fourkas, J. T.; Mohanty, U. Exponential Intermolecular Dynamics in Optical Kerr Effect Spectroscopy of Small-Molecule Liquids. *J. Chem. Phys.* **1999**, *111*, 2686-2694.

(25) Ryu, S.; Stratt, R. M. A Case Study in the Nolecular Interpretation of Optical Kerr Effect Spectra: Instantaneous-Normal-Mode Analysis of the OKE Spectrum of Liquid Benzene. *J. Phys. Chem. B* **2004**, *108*, 6782-6795.

(26) Elola, M. D.; Ladanyi, B. M. Molecular Dynamics Study of Polarizability Anisotropy Relaxation in Aromatic Liquids and Its Connection with Local Structure. *J. Phys. Chem. B* **2006**, *110*, 15525-15541.

(27) Tao, G. H.; Stratt, R. M. Why Does the Intermolecular Dynamics of Liquid Biphenyl So Closely Resemble that of Liquid Benzene? - Molecular Dynamics Simulation of the Optical-Kerr-Effect Spectra. *J. Phys. Chem. B* **2006**, *110*, 976-987.

(28) Coasne, B.; Fourkas, J. T. Structure and Dynamics of Benzene Confined in Silica Nanopores. *J. Phys. Chem. C* **2011**, *115*, 15471-15479.

(29) Stratt, R. M. The Instantaneous Normal Modes of Liquids. *Acc. Chem. Res.* **1995**, *28*, 201-207.

(30) Moore, P.; Keyes, T. Normal Mode Analysis of Liquid CS_2: Velocity Correlation Functions and Self-Diffusion Constants. *J. Chem. Phys.* **1994**, *100*, 6709-6717.

(31) Steele, W. A. A Theoretical Approach to the Calculation of Time-Correlation Functions of Several-Variables. *Mol. Phys.* **1987**, *61*, 1031-1043.

(32) Hu, Z. H.; Huang, X. H.; Annapureddy, H. V. R.; Margulis, C. J. Molecular Dynamics Study of the Temperature-Dependent Optical Kerr Effect Spectra and Intermolecular Dynamics of Room Temperature Ionic Liquid 1-Methoxyethylpyridinium Dicyanoamide. *J. Phys. Chem. B* **2008**, *112*, 7837-7849.

(33) Bonnaud, P.; Nieto-Draghi, C.; Ungerer, P. Anisotropic United Atom Model Including the Electrostatic Interactions of Benzene. *J. Phys. Chem. B* **2007**, *111*, 3730-3741.

(34) Thole, B. T. Molecular Polarizabilities Calculated with a Modified Dipole Interaction. *Chem. Phys.* **1981**, *59*, 341-350.

(35) van Duijnen, P. T.; Swart, M. Molecular and Atomic Polarizabilities: Thole's Model Revisited. *J. Phys. Chem. A* **1998**, *102*, 2399-2407.

(36) Birge, R. R.; Schick, G. A.; Bocian, D. F. Calculation of Molecular Polarizabilities Using a Semiclassical Slater-Type Orbital-Point Dipole Interaction (STOPDI) Model. *J. Chem. Phys.* **1983**, *79*, 2256-2264.

(37) Kiyohara, K.; Kamada, K.; Ohta, K. Orientational and Collision-Induced Contribution to Third-Order Nonlinear Optical Response of Liquid CS_2. *J. Chem. Phys.* **2000**, *112*, 6338-6348.

(38) Alms, G. R.; Burnham, A. K.; Flygare, W. H. Measurement of Dispersion in Polarizability Anisotropies. *J. Chem. Phys.* **1975**, *63*, 3321-3326.

(39) Mossa, S.; Ruocco, G.; Sampoli, M. Orientational and Induced Contributions to the Depolarized Rayleigh Spectra of Liquid and Supercooled Ortho-Terphenyl. *J. Chem. Phys.* **2002**, *117*, 3289-3295.

(40) Smith, W.; Yong, C. W.; Rodger, P. M. DL_POLY: Application to Molecular Simulation. *Mol. Simulat.* **2002**, *28*, 385-471.

(41) Allen, M. P.; Tildesley, D. J. *Computer Simulation of Liquids*; Oxford University Press: Oxford (England), 1989.

(42) Nosé, S. A Unified Formulation of the Constant Temperature Molecular Dynamics Methods. *J. Chem. Phys.* **1984**, *81*, 511-519.

(43) Savitzky, A.; Golay, M. J. E. Smoothing and Differentiation of Data by Simplified Least Squares Procedures. *Anal. Chem.* **1964**, *36*, 1627-1639.

(44) Kivelson, D.; Madden, P. Light Scattering Studies of Molecular Liquids. *Annu. Rev. Phys. Chem.* **1980**, *31*, 523-558.

(45) Battaglia, M. R.; Cox, T. I.; Madden, P. A. Orientational Correlation Parameter for Liquid CS_2, C_6H_6 and C_6F_6. *Mol. Phys.* **1979**, *37*, 1413-1427.

(46) Barocchi, F.; Zoppi, M. Collision Induced Light Scattering: Three- and Four-Body Spectra of Gaseous Argon. *Phys. Lett. A* **1978**, *69*, 187-189.

(47) Williams, D. E.; Cox, S. R. Nonbonded Potentials for Azahydrocarbons - the Importance of the Coulombic Interaction. *Acta Crystallogr. Sect. B: Struct. Sci.* **1984**, *40*, 404-417.

(48) Williams, D. E.; Houpt, D. J. Fluorine Nonbonded Potential Parameters Derived from Crystalline Perfluorocarbons. *Acta Crystallogr. Sect. B: Struct. Sci.* **1986**, *42*, 286-295.

Chapter 5: Toward *in Situ* Measurement of the Density of Liquid Benzene using Optical Kerr Effect Spectroscopy

Adapted from: Bender, J.S.; Cohen, S.R.; He, X., Fourkas, J.T., Coasne B. *J. Phys. Chem. B*, **2016**, *120(34)*, 9103-9114.
Research designed by: John S. Bender and Xiaoxiao He
Research conducted by: John S. Bender and Samuel R. Cohen
Authored by: John S. Bender

5.1 *Introduction*

Optical Kerr effect (OKE) spectroscopy[1-3] has been used broadly to investigate the intermolecular dynamics and structure of liquids as a function of different thermodynamic variables.[4-14] The wide application of OKE spectroscopy, which is the time-domain analog of low-frequency Raman scattering, has been driven by the simplicity of its implementation and the wealth of the information that it can provide. In particular, detailed information on orientational dynamics can be extracted from time-domain OKE data. Furthermore, Fourier-transform deconvolution techniques[15,16] can be used to calculate the Bose-Einstein-corrected, low-frequency Raman spectrum (otherwise known as the reduced spectral density, or RSD), in which the frequency dependence of librational motion is revealed.

OKE data from liquids are often interpreted in terms of features of the intermolecular potential.[6,9,17-21] Through their different modulation of intermolecular interactions, the temperature and density of a liquid have distinct effects on RSDs. For example, as the temperature of a liquid increases, the RSD typically narrows. This effect arises in part because the softening of the intermolecular potential due to decreasing density in turn decreases librational frequencies. On the other hand, an increase in temperature also makes more of the highly anharmonic, repulsive portion of the

intermolecular potential thermally accessible, increasing librational frequencies. Although it is clear from experiments that the density effect is the more important of the two,[9,22] if one could determine the relative magnitudes of these effects it should in principle be possible to use the RSD to determine a liquid's density under any set of accessible thermodynamic conditions.

The effects of density and temperature on the low-frequency Raman spectrum have been studied previously in atomic fluids[23] and liquid carbon disulfide[22,24] using depolarized light scattering (DLS). These studies set out to describe the exponential character of collision-induced spectra for these fluids, and the results were used to derive empirical relations for the effects of density and temperature on the spectra. Fleury *et al.* showed that the density and temperature dependences of the DLS spectrum for monatomic fluids are separable over a large range of thermodynamic states.[23] Hegemann *et al.* characterized the effects of temperature and density of different regions of the DLS spectrum for carbon disulfide.[22,24] Based on calculations by Madden and Cox,[25] these regions were assumed to be dominated by different mechanisms of light scattering. The low-frequency components were attributed to reorientation and the high-frequency components were assigned to gas-like translations.[24] Even though it is now known that reorientation dominates the entire DLS spectrum of carbon disulfide,[26-28] these pioneering studies nevertheless showed that density and temperature can in fact be separable in the low-frequency Raman spectrum of molecular liquids.

Ladanyi *et al.* used molecular dynamics (MD) and Monte Carlo simulations to evaluate the temperature and density dependences of the spectral moments of low-frequency Raman spectra of argon and xenon.[29] It was found that the spectral moments

are quite sensitive to density. In particular, the higher the spectral moment, the stronger the density dependence, suggesting that the high-frequency components of the spectra are significantly affected by changes in density.[29] Ladanyi further used MD simulations to demonstrate that the effective polarizabilities of molecular oxygen and carbon dioxide depend more strongly on density than on temperature.[30] Additionally, it was found that the reorientational and collision-induced/reorientational cross-correlation components of the low-frequency Raman spectrum of oxygen and carbon dioxide are strongly dependent on density.[30] The time scale difference between reorientational dynamics and collision-induced dynamics was also shown to increase with increasing density.[30]

Kohler and Nelson used both isothermal OKE experiments and MD simulations to explore the effects of density and temperature on the OKE response function for liquid carbon disulfide.[11] They observed a rapidly dephasing, oscillatory signal in the response function at high pressures.[11] This result was in agreement with earlier low temperature experiments.[17] The spectral feature was attributed to an increase in librational frequencies with increasing density. Their MD simulations revealed that the single-molecule component in the CS_2 OKE response broadens with decreasing pressure at constant temperature and narrows with decreasing temperature at constant pressure.[11] Thus, density effects dominate the shape of the OKE response for this liquid.

RSDs are often fit to empirical functions to extract information from the thermodynamic evolution of the spectra.[6,9,19,31-34] These functions reproduce experimental spectra reasonably well, but it is difficult to ascribe any physical meaning to the fits. The simulated contributions to the spectra (single-molecule, interaction-induced, and a cross term) have forms that are significantly more complicated than the form of the empirical

functions.[9,35-37] This problem of assignment is exacerbated by the fact that the cross-term between the molecular and interaction-induced components is typically largely negative,[35-37] whereas the total spectrum is always positive. Nevertheless, empirical functions provide a useful description of the qualitative behavior of RSDs.

The low-frequency Raman spectrum of benzene has been the subject of many OKE experiments[4,9,14,19,21,32,34,38,39] and simulations.[35,37,40-42] As is generally the case for molecular liquids, under isobaric conditions the blue edge of the RSD of benzene shifts to higher frequency with decreasing temperature.[9,19] Here we use this liquid as a representative system to identify the distinct effects of temperature and density on RSDs. We have measured isobaric RSDs of benzene at atmospheric pressure for a wide range of temperatures. The time-domain measurements were made with a finer time step and with a larger total delay time than our previous measurements,[9] which decreases interpolation during the deconvolution[15] procedure used to calculate the RSDs and thereby provides more accurate spectra. We have also performed detailed MD studies in which we have isolated the effects that temperature and density have on the RSD of this liquid. The results of these simulations allow us to quantify the individual contributions of temperature and density to the shape of benzene RSDs. By fitting experimental and simulated spectra to common empirical functions, we demonstrate that there is a separable, physical relationship between the fitting parameters and the thermodynamic state of the liquid.

5.2 *Theory*

5.2.1 *OHD-OKE Spectroscopy*

The theory for OHD-OKE spectroscopy is given in Chapter 2, Section 2.2.

5.2.2 *Simulations of OKE Spectra*

To simulate the RSD of bulk benzene, we start by calculating the many-body polarizability of the liquid as shown in Chapter 2, Section 2.1, Subsection 2.1.1. Starting from eq 2.4, for a liquid composed of *N* molecules, each containing *n* polarizable sites, if intramolecular polarizability interactions is assumed to be unimportant in the calculation of the total liquid polarizability, then the *3Nn* × *3Nn* representation of the molecular site interactions can be written for molecules *p* and *q*

$$\overleftrightarrow{\boldsymbol{\alpha}}_i^{-1}\overrightarrow{\boldsymbol{\pi}}_i + \sum_{i\neq j}^{Nn} \overleftrightarrow{\boldsymbol{T}}_{ij}\overrightarrow{\boldsymbol{\pi}}_j\left(1-\delta_{pq}\right) = \overleftrightarrow{\mathbf{1}}\,, \tag{5.1}$$

where δ is the Kronecker delta function. It has been shown previously that this approximation does not have a significant effect on the simulated OKE spectrum of benzene.[37,40,41]

The interaction matrix shown in eq 2.5 then becomes

$$\overleftrightarrow{\boldsymbol{W}} = \overleftrightarrow{\boldsymbol{\alpha}}_i^{-1} + \overleftrightarrow{\boldsymbol{T}}_{ij}\left(1-\delta_{pq}\right)\,. \tag{5.2}$$

The interaction matrix is then inverted and contracted in the manner shown in Chapter 2, Section 2.1, Subsection 2.1.1 to find the many-body polarizability of the liquid. The polarizability TCF is then calculated according to eq 4.3 and the RSD is then calculated according to the theory given in Chapter 2, Section 2.1, Subsection 2.1.2.

5.3 *Experimental Details*

5.3.1 *OHD-OKE Spectrometer*

The OHD-OKE spectrometer is described in Chapter 3. These experiments were performed using nearly-transform-limited 44 fs laser pulses centered at a wavelength of approximately 810 nm.

5.3.2 *Experimental Data Collection and Analysis*

OHD-OKE decays were collected with two different, equally-spaced time steps. To characterize the slower, diffusive orientational motions, scans with a step size of 6.67 fs were performed. To characterize the more rapid inertial and intermolecular dynamics, scans with a time step of 0.667 fs were performed out to 5 ps. Consecutive decays were collected at opposite heterodyne angles. The long-time-step scans were used to fit the long-time diffusive dynamics. The resulting fits were used to strip a long-time tail (with the same point spacing as the short-time-step data) onto the short-time-step data. This procedure assists in the clean removal of the contribution of orientational diffusion when performing the Fourier-transform deconvolution analysis. The decays were integrated and fit to the sum of two exponential functions (for times >2 ps) to determine the orientational diffusion time constants and amplitudes. The exponential with the longer decay constant was removed during the Fourier analysis, as described above.

Cross-correlations between the pump and probe pulses were performed at the sample position using second-harmonic generation from a KDP crystal. Four data scans, with a resolution of 0.667 fs/step, were averaged to measure the autocorrelation and to characterize the laser pulses.

5.3.3 *Sample Preparation*

Liquid benzene (Sigma Aldrich, +99.8%) that had been passed through a 0.2 μm filter was placed in a 1.0-mm-pathlength cuvette. The cuvette was sealed and mounted on a brass sample holder in a continuous-flow vacuum cryostat (Janis ST-100). A silicon-diode probe was placed in contact with the sample cuvette to obtain an accurate temperature reading. To ensure sufficient temperature stabilization, cold nitrogen gas was flowed over the prepared sample for at least one hour before data collection commenced.

5.4 *Computational and Simulation Details*

5.4.1 *Interaction Potential*

Liquid benzene was simulated using the 9-site, anisotropic united-atom model developed by Bonnaud *et al.*, which accurately reproduces the liquid/vapor phase diagram and the molecular structure of liquid benzene as well as important properties such as shear viscosity.[43] The potential parameters are listed in Table 5.1. This model includes six sites for the methine groups of the benzene ring. Two negatively charged sites are placed on either side of the ring face to mimic the π-electron system of the molecule, and one positively charged site is placed at the center of the ring. These nine sites interact through the intermolecular pair potential given in eq 4.8. The interaction potential model is rigid, so there are no torsional, bending, or stretching energy terms.

Table 5.1 Intermolecular potential parameters for benzene

r(CH-CH)	1.715 Å
$q(z = 0.0$ Å$)^a$	$+8.130e$
$q(z = \pm 0.4$ Å$)^a$	$-4.065e$
σ_{CH}	3.361 Å
ε_{CH}/k_B	75.6 K

[a]Along the axis normal to the benzene ring.

5.4.2 *Grand-Canonical Monte Carlo and Molecular Dynamics Simulations*

Grand-canonical Monte Carlo (GCMC) simulations were used to generate liquid benzene in simulation boxes measuring 30 Å in each Cartesian direction. Each liquid system was simulated near the saturation vapor pressure of benzene at each temperature studied. Well-equilibrated simulation boxes for benzene at 240 K, 260 K, 280 K, 293 K, 310 K, 330 K, and 340 K contained 192, 187, 184, 182, 177, 173, and 169 molecules, respectively.

MD simulations of benzene were performed with DL_POLY V2[44] using the potential in eq 4.8. The Verlet Leapfrog algorithm[45] was used to integrate the equations of motion every 5 fs. The SHAKE[46] algorithm was used for bond constraints during translation, whereas Fincham's implicit quaternion algorithm[47] was used for rigid-body rotation. Each simulation used a 27×10^3 Å^3 box under cubic periodic boundary conditions, with the initial configuration generated from the GCMC simulations at the same temperature. The interaction cutoff length was set to 15 Å. Long-range Coulombic interactions were included using Ewald summation, which was automatically optimized by DL_POLY V2 with 1.0×10^{-5} precision. All of the simulations were equilibrated in the NVT ensemble for 50 ps using a Nosé-Hoover thermostat[48,49] with a 10 fs relaxation constant. Using the equilibrated liquids, simulations were then run in the NVE ensemble with no thermostat, and configurations were stored for every time step out to 2 ns of simulation time to ensure sufficient statistics were collected. Simulations were first performed under isobaric conditions for each of the temperatures listed above, i.e. the liquid density was chosen to match the density of the bulk liquid under 1 atm of external

pressure at that temperature. The same temperatures were then used for simulations of liquid benzene with a fixed density of 8.74×10^2 g/L. Finally, six densities ranging from 8.12×10^2 g/L to 9.22×10^2 g/L were used for simulations of liquid benzene held at a fixed temperature of 293 K. The simulation conditions are summarized in Table 5.2.

Table 5.2 Thermodynamic conditions for the isobaric, isochoric, and isothermal simulations.

Isobaric				Isochoric				Isothermal			
T (K)[a]	N_{mol}	ρ (g/L)[b]	P (atm)[d]	T (K)[a]	N_{mol}	ρ (g/L)	P (atm)[d]	T (K)[a]	N_{mol}	ρ (g/L)	P (atm)[d]
240	192	922[c]	1	240	182	874	-763	293	192	922	659
260	187	898[c]	1	260	182	874	-491	293	184	884	60
280	184	884	1	280	182	874	-231	293	182	874	1
293	182	874	1	293	182	874	1	293	177	850	-290
310	177	850	1	310	182	874	148	293	173	831	-411
330	173	831	1	330	182	874	398	293	169	812	-475
340	169	812	1	340	182	874	518				

[a] Uncertainties in temperature are <3%.
[b] Deviations from densities calculated using the Bender equation of state[54] at 1 atm are <1%.
[c] These states are deeply supercooled. Extrapolated values for the Bender equation of state[54] were used for comparison.
[d] Deviations from pressures calculated using the Bender equation of state[54] are <1%. Metastable states were calculated by extrapolation for comparison with the simulation values.

5.4.3 *Polarizability Computation*

The isotropic and anisotropic components of the polarizaiblity ($\sum_i^n \boldsymbol{\pi}_i$) for an isolated molecule were 10.39 Å^3 and -5.62 Å^3, respectively. These values correspond to the polarizability of an isolated molecule as measured experimentally at 632.8 nm.[51] The distributed polarizability model developed by Mossa *et al.* was used to simulate the molecular polarizability of benzene.[52] This model evenly distributes the molecular polarizability to each of the six π-orbital sites in benzene (i.e. $\boldsymbol{\alpha_i} = (\sum_i^n \boldsymbol{\pi}_i)/6$) and has been shown to capture the polarizability dynamics for the liquid accurately.[37,40,41] The result of this distribution is that each polarizability site has the same axial symmetry as

the total molecular polarizability. The configuration of the polarizability sites corresponds to the experimental geometry of the benzene molecule.

The many-body polarizability was calculated in the manner described in section 5.2.2. However, the atomic-to-molecular polarizability transformation (AMPT) approximation, developed by Hu *et al.*, was used to decrease the computational expense.[53] The AMPT approximation effectively treats molecular pair polarizability interactions at the atomic level and many-body interactions at the molecular level. This approximation has been found to have a minimal effect on the accuracy of the simulated OKE spectrum of benzene.[37] Matrix inversions were performed using the LAPACK linear algebra package.[54]

5.4.4 *Collective Polarizability TCF and RSD Analysis*

The simulated collective orientational TCFs were fit to the sum of two exponential functions, the more slowly decaying of which is assumed to arise from orientational diffusion and the more rapidly decaying is assumed to arise from the so-called intermediate response.[9] The diffusive contribution was removed from the OKE response in the same manner as described above for the experimental data. The TCFs were then differentiated with respect to time, and the short-time fit was used to splice a smooth tail (for times >1 ps) onto the OKE response function to yield a smooth RSD upon Fourier transformation. A typical simulated RSD, with and without the splice of the short-time tail, is shown in Figure 5.1.

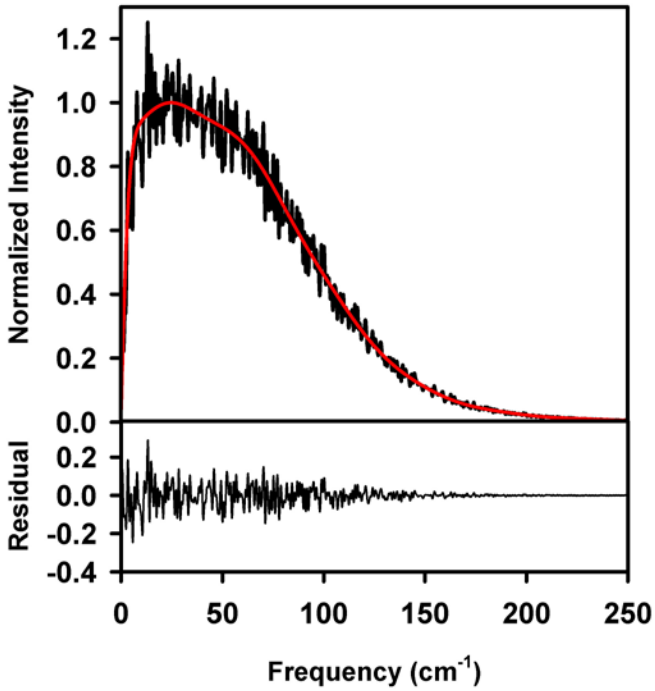

Figure 5.1 The top panel is a comparison of a typical simulated OKE RSD without (black) and with (red) stripping a fit long-time tail onto the decay. The bottom panel shows the difference between the two spectra.

5.5 *Results and Discussion*

5.5.1 *Experimental Spectra*

Isobaric OKE spectra were obtained at temperatures ranging from 275.2 K to 340.1 K. Biexponential fits capturing the collective orientational diffusion and intermediate relaxation[9] components (the latter of which is related to motional narrowing) of the integrated OKE decays are shown in Figure 5.2 and the fit parameters are listed in Table 5.3.

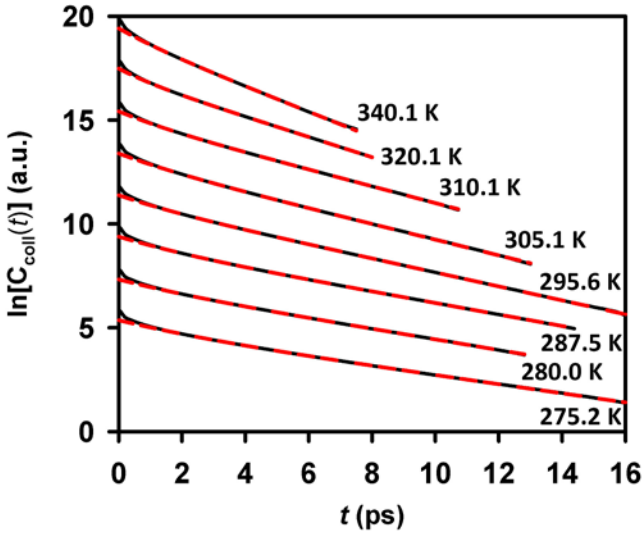

Figure 5.2 Semi-logarithmic plot of the experimental integrated OHD-OKE decays (black) and the biexponential fits (red dash) for bulk benzene at temperatures ranging from 275.2 K to 340.2 K.

Table 5.3 Fit parameters for integrated experimental OKE decays of bulk benzene. Numbers in parentheses are estimated uncertainties in the last digit.

T (K)	A_1	τ_1 (ps)	A_2	τ_2 (ps)
275.2	0.37(2)	1.62(2)	0.63(3)	4.57(2)
280.0	0.31(2)	1.44(3)	0.69(3)	3.99(3)
287.5	0.35(3)	1.28(8)	0.65(3)	3.60(2)
295.6	0.30(2)	1.10(2)	0.69(3)	2.99(2)
305.1	0.32(2)	1.03(1)	0.67(3)	2.69(2)
310.0	0.32(2)	0.89(1)	0.68(3)	2.48(2)
320.1	0.31(2)	0.69(2)	0.69(3)	2.05(2)
340.2	0.32(2)	0.75(6)	0.68(3)	1.65(2)

As the temperature of a typical bulk liquid such as benzene is decreased, the blue edge of the OKE RSD shifts to higher frequency and the red edge shifts to lower frequency (Figure 5.3A).[9,14,21,55] The shift of the blue edge of the RSD with decreasing temperature has been attributed to an increase in the librational frequencies due to densification of the liquid.[55] The shift of the red edge with decreasing temperature has been related to a reduction in motional narrowing as the time scale of liquid dynamics becomes longer.[42,55]

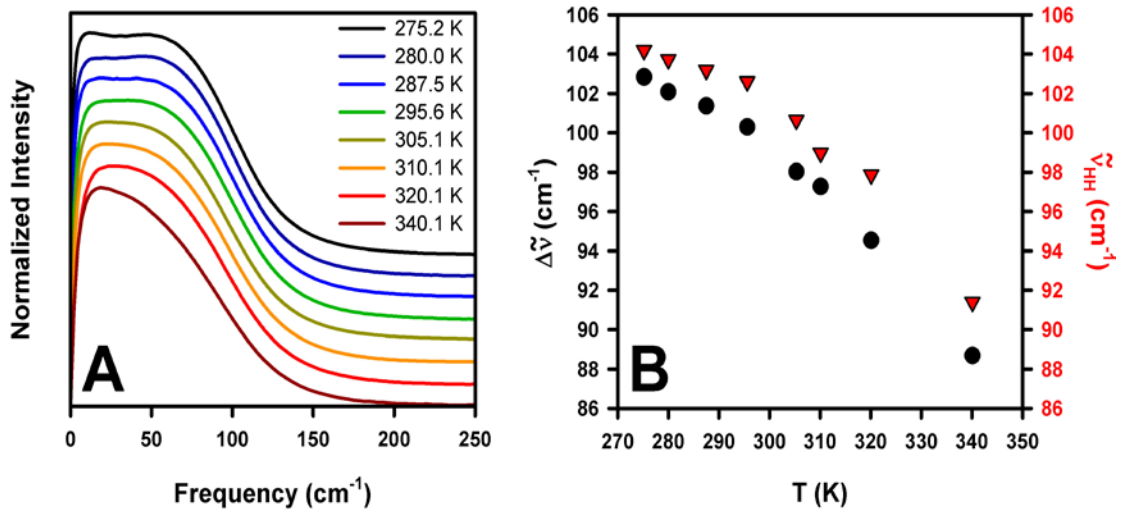

Figure 5.3 (A) Isobaric OKE RSDs for benzene as a function of temperature from 275.2 K to 320.1 K. The plots are offset for clarity. (B) Full width at half maximum (black circles) and frequency at half height (red triangles) of the blue edge of the RSD as a function of temperature.

To quantify the effects of temperature and density on the isobaric OKE RSD of benzene, the full width at half maximum ($\Delta\tilde{\nu}$) and the frequency at half height ($\tilde{\nu}_{HH}$) of the high-frequency edge were used to describe the evolution of the spectrum. Although $\Delta\tilde{\nu}$ is typically used to describe the broadening of spectra, RSDs are a special case because they extend down to zero frequency. The red edge of the RSD is affected by factors that do not influence the blue edge of the spectrum, such as motional narrowing and the cross term between interaction-induced and librational scattering. The use of $\tilde{\nu}_{HH}$

in lieu of $\Delta\tilde{\nu}$ avoids these potential problems, and so we examine both quantities here. Figure 5.3B shows $\Delta\tilde{\nu}$ and $\tilde{\nu}_{HH}$ as a function of temperature as measured experimentally for liquid benzene. Both values decrease monotonically as the temperature of the liquid is increased. On the one hand, the intermolecular potential well around each molecule becomes broader as the density of the liquid decreases with increasing temperature, which leads to a decrease in $\tilde{\nu}_{HH}$. On the other hand, increasing the liquid temperature also allows molecules to sample more of the highly anharmonic, repulsive portion of the local potential, which leads to a blue shift of $\tilde{\nu}_{HH}$. The spectra in Figure 5.3 indicate that the former phenomenon plays a more important role in the shape of the RSD than does the latter one.

5.5.2 *Simulated Spectra*

We used MD simulations to assess how the effects of temperature and density are reflected in OKE RSDs. We first consider the isobaric RSDs of the bulk liquid at atmospheric pressure for temperatures ranging from 240 K to 340 K. Biexponential fit parameters for the OKE decays are listed in Table 5.4. The simulated OKE TCFs are shown in Figure 5.4.

Table 5.4 Fit parameters for simulated isobaric OKE decays of benzene at atmospheric pressure. Numbers in parentheses are estimated uncertainties in the last digit.

T (K)	A_1	τ_1 (ps)	A_2	τ_2 (ps)
240	0.25(2)	0.89(8)	0.75(2)	8.0(7)
260	0.25(2)	0.79(6)	0.75(2)	5.6(3)
280	0.35(2)	0.78(6)	0.65(2)	4.9(2)
293	0.26(3)	0.80(5)	0.74(3)	3.2(2)
310	0.37(3)	0.48(4)	0.63(3)	3.0(1)
330	0.38(3)	0.60(4)	0.62(3)	2.5(1)
340	0.42(3)	0.25(2)	0.58(3)	1.8(1)

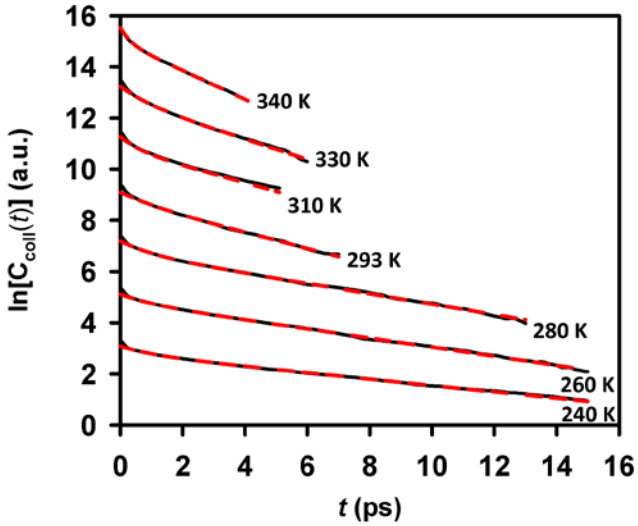

Figure 5.4 Semi-logarithmic plot of the simulated collective correlation functions $C_{coll}(t)$ (black) and the biexponential fits (red dash) for benzene at equilibrium density and atmospheric pressure as a function of temperature.

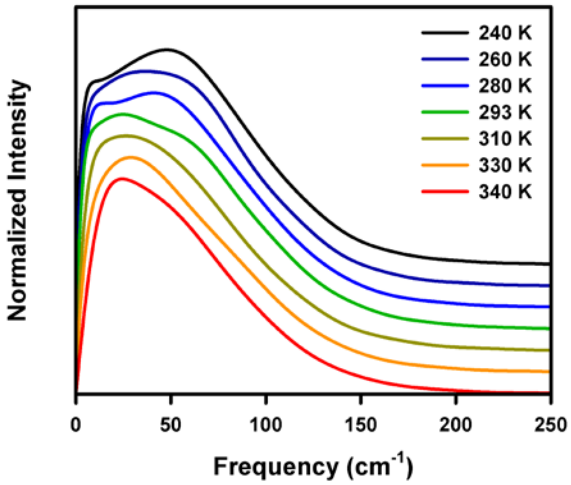

Figure 5.5 Simulated OKE RSDs for benzene at atmospheric pressure at different temperatures. The plots are offset for clarity.

The simulated RSDs at seven temperatures in this range are shown in Figure 5.5. Our simulated spectra are of similar quality to those calculated previously by other groups using different potentials and polarizability models.[35,40,41] The simulated RSDs strongly resemble, but are somewhat narrower than, the experimental RSDs. In agreement with experiment, with decreasing temperature the red edge of the simulated RSDs shifts to lower frequency and the blue edge shifts to higher frequency. As can be seen by inspection of Figure 5.1, the noise in the spectrum increases as the frequency decreases, creating greater uncertainty in the low-frequency components of the smoothed spectrum than their high-frequency counterparts.

5.5.3 *Isochoric Spectra*

We next assess the effect of temperature on the RSD of bulk liquid benzene held at a constant density of 0.874 g/mL. The biexponential fit parameters for the simulated, integrated OKE decays under these conditions are listed in Table 5.5. As shown in Figure 5.6A, with decreasing temperature, both the red and blue edges of the transformed spectrum move to lower frequency. The effect on the red edge of the spectrum can again be ascribed to a decrease in motional narrowing with decreasing temperature. The red shift of the blue edge of the spectrum with decreasing temperature at constant density is indicative of the anharmonicity in the repulsive portion of the intermolecular potential of the liquid. At higher temperatures the liquid has greater access to higher portions of the intermolecular potential well, which are steeper than the lower portions of the potential well. This phenomenon causes the average librational frequency to increase with increasing temperature.

Table 5.5 Fit parameters for integrated, simulated OKE decays of benzene at a density of 0.874 g/mL. Numbers in parentheses are estimated uncertainties in the last digit.

T (K)	A_1	τ_1 (ps)	A_2	τ_2 (ps)
240	0.29(4)	0.54(1)	0.71(4)	4.6(3)
260	0.28(4)	0.60(5)	0.72(4)	4.1(3)
280	0.32(3)	0.74(5)	0.68(3)	4.1(3)
293	0.26(3)	0.80(5)	0.74(3)	3.2(2)
310	0.28(3)	0.43(5)	0.72(3)	3.0(2)
330	0.34(3)	0.31(4)	0.66(3)	2.7(2)
340	0.33(3)	0.35(4)	0.67(3)	2.7(2)

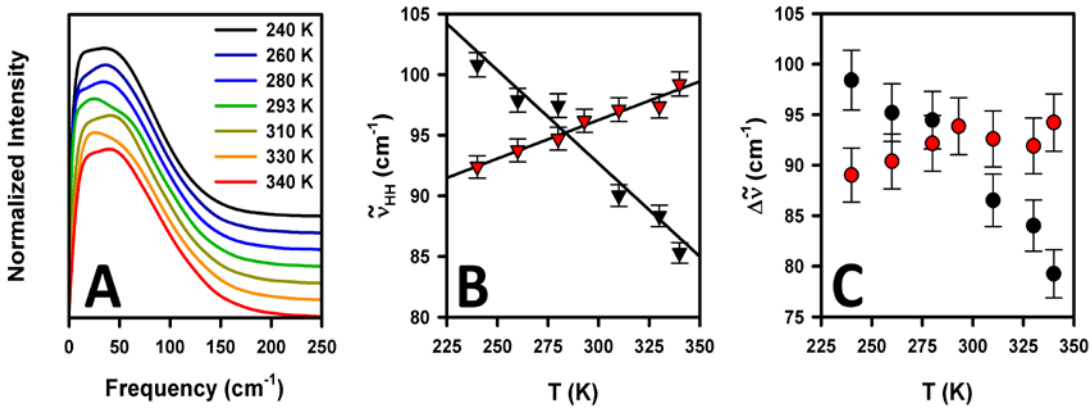

Figure 5.6 (A) Simulated OKE RSDs for benzene at different temperatures at a density of 874 g/L. The plots are offset for clarity. (B) The dependence of $\tilde{\nu}_{HH}$of the blue edge on temperature for the isobaric liquid (black triangles) and the isochoric liquid (red triangles). The lines are linear least-squares fits of the data. (C) $\Delta\tilde{\nu}$ of the simulated spectra as a function of temperature for the isobaric liquid (black circles) and the isochoric liquid (red circles). The error bars are estimated at 1% for the $\tilde{\nu}_{HH}$values and 3% for the $\Delta\tilde{\nu}$ values.

In Figure 5.6B we plot $\tilde{\nu}_{HH}$ as a function of temperature for the isobaric liquid (isobaric, black triangles) and the isochoric liquid (isochoric, red triangles). The positive shift of $\tilde{\nu}_{HH}$ with increased temperature in the isochoric liquid has a somewhat smaller overall range than the negative shift for the isobaric liquid, indicating that the influence of density on the blue edge of the RSD is larger in magnitude than the overall shift observed with temperature for the liquid at its equilibrium density at atmospheric pressure. This result suggests that although the softening of the intermolecular potential with decreasing density is the major factor in determining the shift of the high-frequency

edge of the RSD, this effect is indeed counterbalanced to some extent by the increase in thermal energy in the liquid.

In agreement with experiment, $\Delta\tilde{\nu}$ of the liquid at atmospheric pressure moves to lower values as the temperature is increased, as shown in Figure 5.6C. For the isochoric spectra, $\Delta\tilde{\nu}$ tends to larger values as the temperature increases. This result can be interpreted in terms of an increase in access to the anharmonic, repulsive portion of the intermolecular potential as the temperature of the liquid is increased. Within the associated error, $\Delta\tilde{\nu}$ for the isochoric spectra increases monotonically as the temperature of the liquid increases. Qualitatively, $\Delta\tilde{\nu}$ values for the constant-density liquid span a shorter range than do the values for the atmospheric pressure liquid, indicating that density has a greater effect on the breadth of the RSD than does temperature.

Based on linear regressions of the $\tilde{\nu}_{HH}$ data in Figure 5.6B, $\tilde{\nu}_{HH}$ shifts by -0.15 ± 0.02 cm^{-1}/K in the isobaric liquid and by 0.064 ± 0.005 cm^{-1}/K in the isochoric liquid. If we assume that the effects of temperature and density are additive, then the contribution of density alone to the shift of $\bar{\nu}_{HH}$ with temperature is -0.21 ±0.02 cm^{-1}/K. Thus, density affects the magnitude of the shift of the high-frequency side of the OKE RSD of benzene by a factor of ~3 more than does temperature.

5.5.4 *Isothermal Spectra*

We investigated the influence of density on the RSD further by simulating liquid benzene at 293 K at a range of different densities. The biexponential fit parameters for the simulated, integrated OKE decays under these conditions are listed in Table 5.6. As shown in Figure 5.7A, the blue edge of the RSD moves to higher frequency with

increasing density, as expected. It is possible that the small peak at low frequency for the densest liquid is an error arising from the fitted function used to smooth the spectrum.[56]

Table 5.6 Fit parameters for integrated, simulated OKE decays of benzene at 293 K. Numbers in parentheses are estimated uncertainties in the last digit.

ρ (g/mL)	A_1	τ_1 (ps)	A_2	τ_2 (ps)
0.812	0.31(3)	0.38(5)	0.69(3)	2.0(1)
0.831	0.33(3)	0.33(5)	0.67(3)	2.3(1)
0.850	0.31(3)	0.52(5)	0.69(3)	2.8(2)
0.874	0.26(3)	0.80(5)	0.74(3)	3.2(2)
0.898	0.28(2)	0.65(6)	0.72(2)	4.0(2)
0.922	0.41(2)	1.7(5)	0.59(2)	6.8(3)

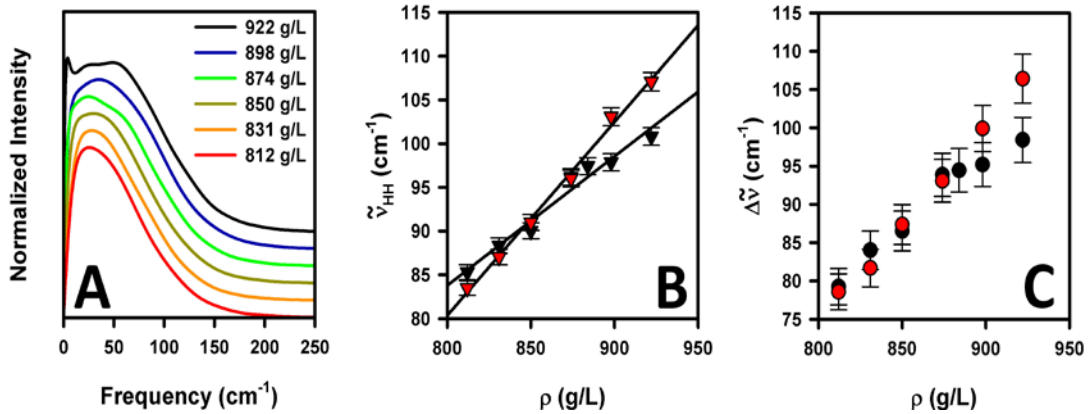

Figure 5.7 (A) Simulated OKE RSDs for benzene for different densities at 293 K. The plots are offset for clarity. (B) The dependence of $\tilde{\nu}_{HH}$ on temperature for the isobaric liquid (black triangles) and the isothermal liquid (red triangles). The solid lines are linear regressions of the data. (C) $\Delta\tilde{\nu}$ of the simulated spectra as a function of density for the isobaric liquid (black circles) and the isothermal liquid (red circles). The error bars are estimated at 1% for the $\tilde{\nu}_{HH}$ values and 3% for the $\Delta\tilde{\nu}$ values.

Figures 5.7B and 5.7C show that the dependences of $\tilde{\nu}_{HH}$ and $\Delta\tilde{\nu}$ on density at constant temperature are indeed greater than their dependence on density with temperature at constant pressure. The linear fits in Figure 5.7B confirm that the effect of density on the magnitude of the shift is ~3 times greater than the effect of temperature. The width $\Delta\tilde{\nu}$ increases with density faster in the isothermal liquid faster than in the

isobaric liquid, suggesting that density significantly affects the evolution of spectral inhomogeneity in benzene.

5.5.5 *Thermodynamic Connections to Empirical Lineshapes*

For further extraction of thermodynamic trends from the OKE data, we fitted empirical functions to the simulated and experimental data. These functions have no rigorous physical connection to the spectra, but are often assumed to correspond to distinct scattering mechanisms. For example, RSDs are often fit to the sum of the so-called Bucaro-Litovitz (BL) function and an anti-symmetrized Gaussian (AG) function. The resultant function takes the form

$$f_{BL,AG} = A_{BL}\omega^{\delta}e^{-\omega/\omega_{BL}} + A_{AG}\left[e^{-(\omega-\omega_{AG})/2\sigma_{AG}^2} - e^{-(\omega+\omega_{AG})/2\sigma_{AG}^2}\right]. \qquad (5.3)$$

Here, $A_{BL}$is the amplitude of the BL function, δ describes how quickly the rising edge of the BL function reaches a maximum, ω_{BL} is the characteristic frequency of the BL function, A_{AG} is the amplitude of the AG function, and ω_{AG} and σ_{AG} are the center frequency and width, respectively, of the two Gaussian functions comprising the AG function. The BL function was developed to fit depolarized light scattering spectra from monatomic fluids,[57] and is therefore commonly associated with collision-induced scattering. However, the intensity of the BL functions for the fits to the simulated spectra is greater than the intensity of the interaction-induced components of the spectra for benzene.[37] Therefore, the BL function overestimates the collision-induced contributions to the spectrum. The AG function is usually attributed to librational scattering. Although any physical information contained in this function is likely dominated by librational character, interaction-induced contributions are also present. We have chosen to set the amplitude associated with the AG function to unity for the normalized line shape

analysis, on the basis that the true height of the AG function is modulated by the difference of the two Gaussian functions comprising the total. The center frequencies and widths of the AG function fits to the experimental data are in agreement with previous results, but with decreased uncertainties in the fitting parameters.

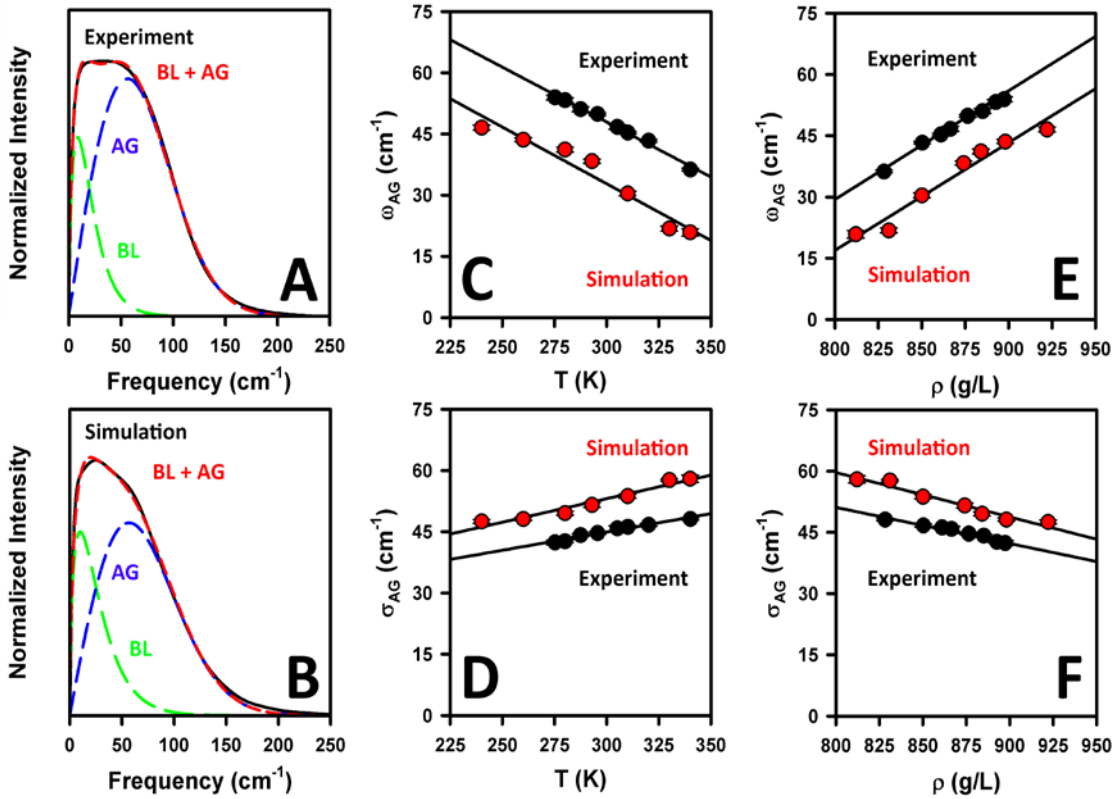

Figure 5.8 (A) Representative fit of BL and AG functions to experimental data obtained at 295.6 K. (B) Representative fit of BL and AG functions to simulated data at 293 K. (C) Center frequency of the AG function for experimental and simulated data under standard conditions as a function of temperature. (D) Width of the AG function for experimental and simulated data under standard conditions as a function of temperature. (E) Center frequency of the AG function for experimental and simulated data under standard conditions as a function of density. (F) Width of the AG function for experimental and simulated data under standard conditions as a function of density. The solid lines in (C), (D), (E), and (F) are linear least squares fits.

Figures 5.8A and 5.8B show representative fits to the BL and AG functions to experimental and simulated isobaric RSDs for benzene, respectively. In both cases, the spectra are well described by the BL and AG functions. The fit parameters for the experimental data are given in Table 5.7. The fits are in agreement with previous

experimental data for both the BL and AG functions.[9] δ increases monotonically with temperature and ω_{BL} essentially remains constant. The fit parameters for the simulated spectra, which are listed in Table 5.8, are in qualitative agreement with the experimental results.

Table 5.7 Fit parameters for experimental OKE RSDs of benzene. Numbers in parentheses are estimated uncertainties in the last digit.

T (K)	A_{BL}	δ	ω_{BL} (cm^{-1})	ω_{AG} (cm^{-1})	σ (cm^{-1})
275.2	0.52(2)	0.51(3)	12.3(6)	54.0(6)	42.4(6)
280	0.41(2)	0.60(3)	12.0(6)	53.3(6)	42.7(3)
287.5	0.40(2)	0.62(3)	12.2(6)	51.1(6)	44.2(3)
295.6	0.30(1)	0.73(3)	11.8(3)	49.9(3)	44.7(3)
305.1	0.30(2)	0.73(3)	12.2(6)	46.7(6)	45.9(6)
310.1	0.27(1)	0.77(3)	12.1(3)	45.3(3)	46.2(3)
320.1	0.191(9)	0.88(3)	12.3(3)	43.3(3)	46.7(3)
340.1	0.26(1)	0.89(9)	12(2)	36.3(3)	48.1(3)

Table 5.8 Fit Parameters for isobaric simulated OKE RSDs of benzene. Numbers in parentheses are estimated uncertainties in the last digit.

T (K)	A_{BL}	δ	ω_{BL} (cm^{-1})	ω_{AG} (cm^{-1})	σ (cm^{-1})
240	0.33(1)	0.53(6)	15.2(6)	46.6(6)	47.5(5)
260	0.290(6)	0.62(1)	15.6(7)	43.5(5)	48.1(4)
280	0.26(1)	0.66(6)	15.6(6)	41.2(6)	49.5(5)
293	0.33(2)	0.61(8)	16.6(4)	38.3(5)	51.6(6)
310	0.22(1)	0.72(7)	19.5(7)	30.4(6)	53.7(5)
330	0.17(6)	0.76(6)	24.4(6)	21.8(6)	57.6(3)
340	0.08(6)	1.1(8)	16.9(8)	20.9(9)	58.0(9)

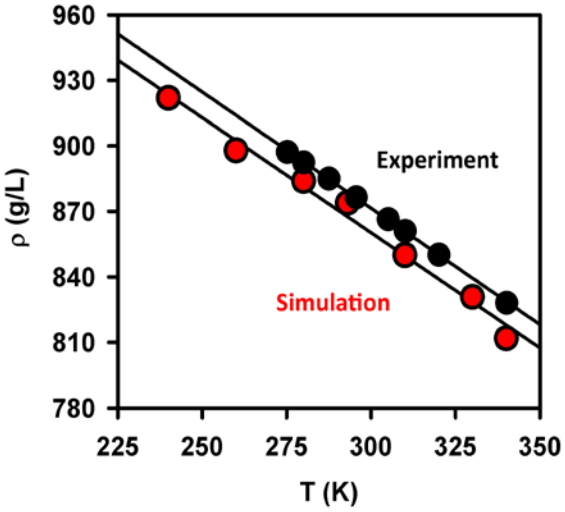

Figure 5.9 The liquid density of benzene as a function of temperature for experiment and simulation. The black lines are linear regressions to the experiment (black) and simulation (red) data.

We are primarily concerned with the high-frequency components of the RSD, so we concentrate on the fit parameters for the AG functions, which are plotted as a function of temperature and density in Figure 5.8. Figures 5.8C and 5.8D show the respective plots of ω_{AG} and σ_{AG} as a function of temperature for the experimental and simulated data under atmospheric pressure. The values of ω_{AG} for the fits of the simulated data are slightly smaller than the experimental values, and the values of σ_{AG} are slightly larger due to the narrower simulated spectra. However, the rate at which these values change with temperature is remarkably similar between the two sets of data. In fact, the trend in ω_{AG} is identical for the experimental and simulated data. Figures 5.8E and 5.8F show the same plots as a function of density, demonstrating the same linear trends for the experimental and simulated data. Figure 5.9 shows the density of benzene as a function of temperature for the simulations and experiment. In both cases, the density of benzene is linear in temperature, and the trends are nearly identical. However, the simulated densities are

slightly lower than the experimental densities, which contributes to the narrower simulated spectra. These results indicate that whereas the simulated spectra do not capture the polarizability dynamics of the liquid exactly, the thermodynamic evolution of the simulated spectra can be compared directly to experiment.

Table 5.9 Fit Parameters for isochoric simulated OKE RSDs of benzene. Numbers in parentheses are estimated uncertainties in the last digit.

T (K)	A_{BL}	δ	ω_{BL} (cm^{-1})	ω_{AG} (cm^{-1})	σ (cm^{-1})
240	0.209(8)	0.81(1)	13.58(8)	39.58(8)	46.61(6)
260	0.23(6)	0.67(1)	17.7(1)	36.9(1)	49.99(8)
280	0.32(2)	0.58(1)	17.8(1)	37.4(1)	50.54(8)
293	0.33(1)	0.61(3)	16.6(3)	38.3(3)	51.6(3)
310	0.17(1)	0.75(2)	20.2(1)	35.57(7)	53.61(7)
330	0.10(1)	1.01(8)	16.46(9)	36.15(9)	55.33(7)
340	0.14(1)	0.82(2)	20.4(2)	35.26(7)	56.20(7)

Table 5.10 Fit parameters for isothermal simulated OKE RSDs of benzene. Numbers in parentheses are estimated uncertainties in the last digit.

ρ (g/mL)	A_{BL}	δ	ω_{BL} (cm^{-1})	ω_{AG} (cm^{-1})	σ (cm^{-1})
0.922	0.66(3)	0.29(1)	18.5(2)	48.2(1)	51.3(1)
0.898	0.24(2)	0.69(1)	16.27(9)	43.20(8)	52.1(6)
0.874	0.33(1)	0.61(3)	16.6(3)	38.3(3)	51.6(3)
0.850	0.21(1)	0.73(1)	18.6(1)	32.6(1)	52.06(8)
0.831	0.12(2)	0.94(1)	19.2(1)	26.2(1)	53.49(6)
0.812	0.14(2)	0.84(2)	22.3(2)	21.5(1)	54.3(6)

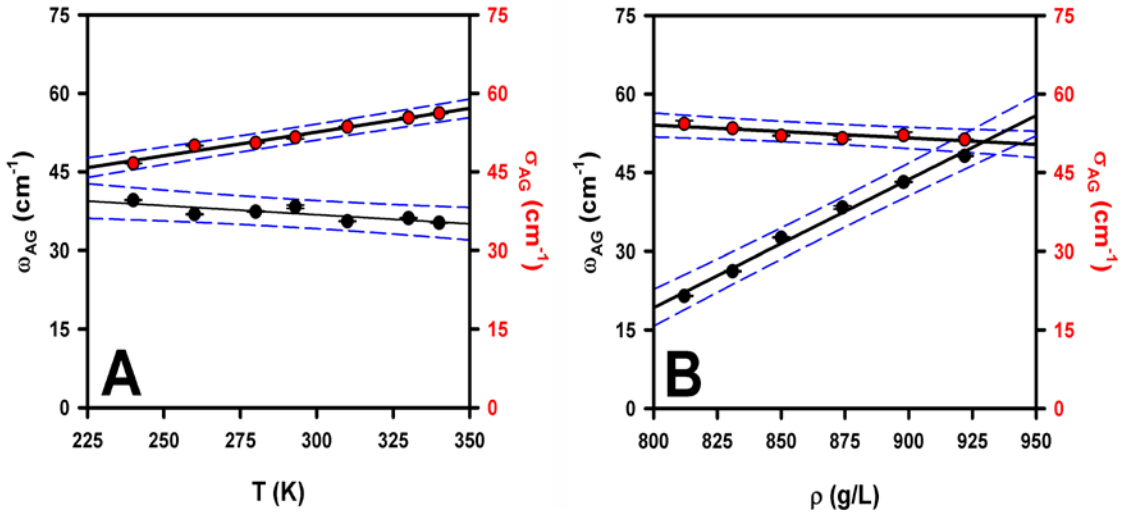

Figure 5.10 Fit parameters for the AG function for the (A) isochoric and (B) isothermal simulations. The dotted blue lines represent the 95% prediction band.

The AG fits to the isochoric and isothermal simulations show that the effects of temperature and density are separable in the low-frequency Raman spectra of benzene. The fit parameters are given in Tables 5.9 and 5.10, respectively. Figure 5.10A shows the fit parameters for the isochoric simulations. Here, it is seen that the thermodynamic evolution of the spectrum is captured almost completely by the width of the AG function σ_{AG}, whereas ω_{AG} is independent of temperature to within our statistical uncertainty. The 95% prediction band for σ_{AG} is quite narrow, whereas the 95% prediction band for ω_{AG} is more than twice as broad. These results suggest that σ_{AG} indeed describes the thermal accessibility of librational states in the liquid, in confirmation of a previous conjecture for benzene.[9]

Figure 5.10B shows the temperature and density dependences of the AG fitting parameters for the isothermal simulations. The dependence of the spectrum on density correlates strongly with ω_{AG}, but is nearly independent of σ_{AG}. The 95% prediction band associated with ω_{AG} is slightly wider than the band associated with σ_{AG}, which is likely

due to the much larger range of values that ω_{AG} covers. These results indicate that the effects of density on the high-frequency components of the OKE spectrum are highly correlated with ω_{AG}, which is therefore reflective of the stiffness of the intermolecular potential.

5.5.6 *Liquid Structure*

According to the van der Waals picture of liquids, density has a greater impact on the structure of a liquid than does temperature.[58] We can assess this influence by looking at the radial distribution functions $g(r)$ for our simulations. Figure 5.11A shows the center-to-center $g(r)$ for the atmospheric pressure simulations. At distances shorter than ~4.4 Å, which correspond to the closest molecular contacts, the average distance between molecules becomes somewhat shorter with increasing temperature. For larger values of r, the average distance increases with increasing temperature. This behavior is consistent with thermal energy giving the liquid greater access to the repulsive portion of the intermolecular potential, even as the liquid itself becomes less dense. The radial distribution functions for the constant-density simulations (Figure 5.11B) show little change in structure with temperature. However, for distances shorter than ~4.6 Å, the average pair distance decreases slightly with increasing temperature. There is also a shift to shorter pair distances with increasing temperature for the peak located at 6.0 Å. Figure 5.11C shows that the average molecular pair distance shifts to shorter distances with increasing density over the entire range of the functions.

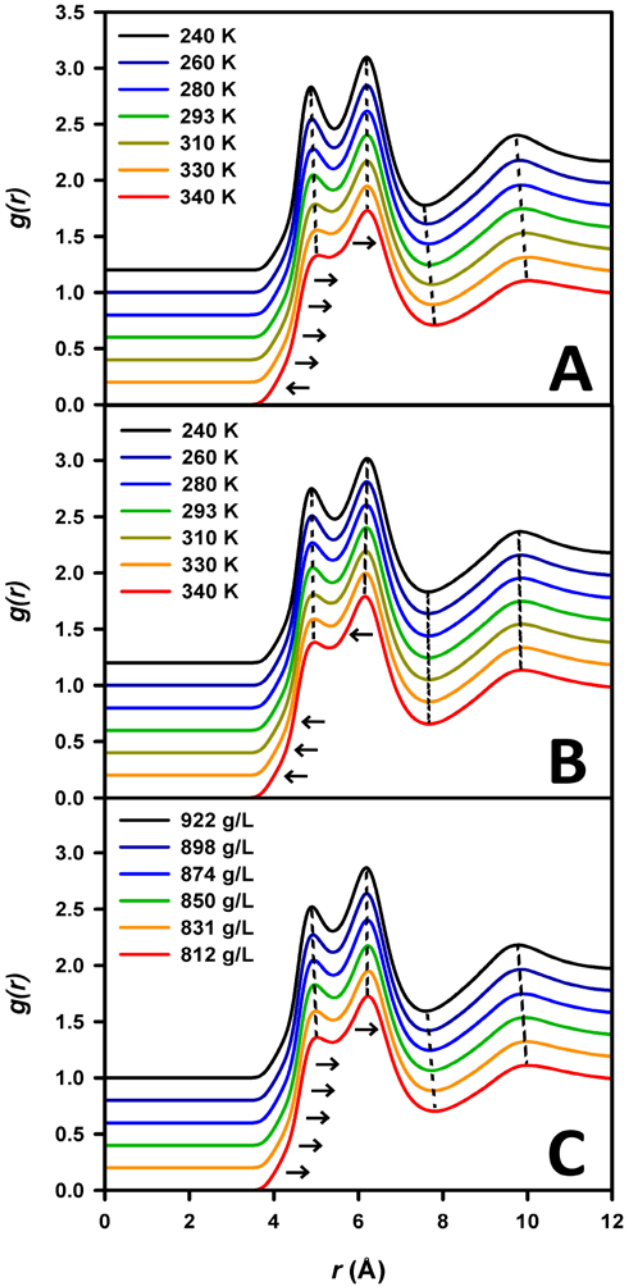

Figure 5.11 The center-to-center radial distribution functions for benzene simulated under (A) standard temperature and density, (B) constant density, and (C) constant temperature conditions. The dashed lines and arrows are guides for the eye. The plots are offset for clarity.

The OKE spectrum is sensitive to the liquid structure through dipole-induced-dipole interactions, and Figure 5.11 shows that density has a greater impact on the liquid structure of benzene, and over much greater pair distances, than does temperature. The decrease in pair distances with increasing density leads to a decrease in free volume, and the librational frequencies of benzene therefore experience a blue shift with increased density. Furthermore, the fact that the evolution of the shifts in the librational components of the OKE RSD with respect to temperature and density is recapitulated in the structure of the first and second coordination shells of the liquid suggests that the local structure of a liquid is indeed captured by the spectrum.

5.6 *Conclusions*

We have used a combination of GCMC and MD simulations to interpret the experimentally observed temperature/density dependent evolution of the benzene OKE RSD. Temperature and density have opposing effects on the shape and breadth of the RSD. The effects of broadening of the potential wells with the decreasing density caused by increasing temperature are offset to some extent by the increased access to the anharmonic, repulsive portion of the wells. Our simulated spectra of benzene show that the high-frequency edge of the RSD blue shifts upon increasing density at constant temperature and, to a lesser extent, upon increasing temperature at constant density. These results imply that intermolecular distances play a greater role in determining librational frequencies in benzene than does the kinetic energy of the molecules. In accordance with the van der Waals picture of molecular liquid structure, density has a greater impact than does temperature on the structure of the liquid. Again, the effect of density is the opposite of that of temperature at short molecular pair distances, indicating

temperature mitigates the effect of density on the librational frequencies of benzene. It would be interesting to conduct experiments at constant temperature and varying densities, and vice versa, to quantify these effects experimentally.

We fit the experimental and simulated data to a sum of Bucaro-Litovitz and anti-symmetrized Gaussian functions. The high-frequency components of the experimental spectrum evolve in the same manner as the simulated spectra for the liquid under standard conditions, suggesting that the thermodynamic evolution of the simulated spectra can be directly compared to the experimental data. The fitting parameters for the isochoric and isothermal simulations show that the effects of temperature and density are separable in the OKE spectrum of benzene.

Our results suggest that the temperature and density of bulk benzene should be uniquely determined by the parameters of empirical fits to BL and AG functions. It will be important to test this conjecture experimentally. If this behavior holds, then it will be possible to use OKE spectroscopy to determine the temperature and density of benzene simultaneously. Because this liquid has a known equation of state, the temperature and density are sufficient to determine the pressure of the liquid as well.

Given that the qualitative features of the dependence of the RSD of benzene on temperature hold for many other simple liquids, it is likely that the separability of the contributions of temperature and density to the RSD will be a feature of the majority of van der Waals liquids. OKE spectroscopy may therefore be a valuable tool for making *in situ* measurements of thermodynamic conditions in liquids and for determining equations of state.

5.7 *References*

(1) Zhong, Q.; Fourkas, J. T. Optical Kerr Effect Spectroscopy of Simple Liquids. *J. Phys. Chem. B* **2008**, *112*, 15529-15539.

(2) Hunt, N. T.; Jaye, A. A.; Meech, S. R. Ultrafast Dynamics in Complex Fluids Observed Through the Ultrafast Optically-Heterodyne-Detected Optical-Kerr-Effect (OHD-OKE). *Phys. Chem. Chem. Phys.* **2007**, *9*, 2167-2180.

(3) Righini, R. Ultrafast Optical Kerr-Effect in Liquids and Solids. *Science* **1993**, *262*, 1386-1390.

(4) Ricci, M.; Wiebel, S.; Bartolini, P.; Taschin, A.; Torre, R. Time-Resolved Optical Kerr Effect Experiments on Supercooled Benzene and Test of Mode-Coupling Theory. *Philos. Mag.* **2004**, *84*, 1491-1498.

(5) Taschin, A.; Bartolini, P.; Eramo, R.; Righini, R.; Torre, R. Evidence of Two Distinct Local Structures of Water from Ambient to Supercooled Conditions. *Nat. Commun.* **2013**, *4*, 2401.

(6) Xiao, D.; Rajian, J. R.; Cady, A.; Li, S.; Bartsch, R. A.; Quitevis, E. L. Nanostructural Organization and Anion Effects on the Temperature Dependence of the Optical Kerr Effect Spectra of Ionic Liquids. *J. Phys. Chem. B* **2007**, *111*, 4669-4677.

(7) Winkler, K.; Lindner, J.; Bürsing, H.; Vöhringer, P. Ultrafast Raman-Induced Kerr-Effect of Water: Single Molecule Versus Collective Motions. *J. Chem. Phys.* **2000**, *113*, 4674-4682.

(8) Loughnane, B. J.; Scodinu, A.; Fourkas, J. T. Temperature-Dependent Optical Kerr Effect Spectroscopy of Chloroform in Restricted Geometries. *Chem. Phys.* **2000**, *253*, 323-330.

(9) Loughnane, B. J.; Scodinu, A.; Fourkas, J. T. Temperature-Dependent Optical Kerr Effect Spectroscopy of Aromatic Liquids. *J. Phys. Chem. B* **2006**, *110*, 5708-5720.

(10) Sokolowsky, K. P.; Bailey, H. E.; Fayer, M. D. Length Scales and Structural Dynamics in Nematogen Pseudonematic Domains Measured with 2D IR Vibrational Echoes and Optical Kerr Effect Experiments. *J. Phys. Chem. B* **2014**, *118*, 7856-7868.

(11) Kohler, B.; Nelson, K. A. Femtosecond Impulsive Stimulated Light Scattering from Liquid Carbon Disulfide at High Pressure: Experiment and Computer Simulation. *J. Phys. Chem.* **1992**, *96*, 6532-6538.

(12) Ishizumi, A.; Kasami, M.; Mishina, T.; Yamamoto, S.; Nakahara, J. Optical Kerr Effect in Carbon Disulfide Under High Pressure. *High Pressure Res.* **2003**, *23*, 201-204.

(13) Ishizumi, A.; Yamamoto, S.; Nakahara, J. Pressure Dependence of Low-Frequency Light Scattering in Carbon Disulfide. *J. Lumin.* **2001**, *94–95*, 687-690.

(14) Rønne, C.; Jensby, K.; Loughnane, B. J.; Fourkas, J.; Nielsen, O. F.; Keiding, S. R. Temperature Dependence of the Dielectric Function of C_6H_6(l) and $C_6H_5CH_3$(l) Measured with THz Spectroscopy. *J. Chem. Phys.* **2000**, *113*, 3749-3756.

(15) McMorrow, D.; Lotshaw, W. T. Intermolecular Dynamics in Acetonitrile Probed with Femtosecond Fourier-Transform Raman-Spectroscopy. *J. Phys. Chem.* **1991**, *95*, 10395-10406.

(16) McMorrow, D.; Lotshaw, W. T. The Frequency Response of Condensed-Phase Media to Femtosecond Optical Pulses: Spectral-Filter Effects. *Chem. Phys. Lett.* **1990**, *174*, 85-94.

(17) Ruhman, S.; Kohler, B.; Joly, A. G.; Nelson, K. A. Intermolecular Vibrational Motion in CS_2 Liquid at $165 \leqslant T \geqslant 300$ K Observed by Femtosecond Time-Resolved Impulsive Stimulated Scattering. *Chem. Phys. Lett.* **1987**, *141*, 16-24.

(18) Farrer, R. A.; Loughnane, B. J.; Deschenes, L. A.; Fourkas, J. T. Level-Dependent Damping in Intermolecular Vibrations: Linear Spectroscopy. *J. Chem. Phys.* **1997**, *106*, 6901-6915.

(19) Ricci, M.; Bartolini, P.; Chelli, R.; Cardini, G.; Califano, S.; Righini, R. The Fast Dynamics of Benzene in the Liquid Phase - Part I. Optical Kerr Effect Experimental Investigation. *Phys. Chem. Chem. Phys.* **2001**, *3*, 2795-2802.

(20) Smith, N. A.; Meech, S. R. Ultrafast Dynamics of Polar Monosubstituted Benzene Liquids Studied by the Femtosecond Optical Kerr Effect. *J. Phys. Chem. A* **2000**, *104*, 4223-4235.

(21) Zhong, Q.; Fourkas, J. T. Shape and Electrostatic Effects in Optical Kerr Effect Spectroscopy of Aromatic Liquids. *J. Phys. Chem. B* **2008**, *112*, 15342-15348.

(22) Hegemann, B.; Baker, K.; Jonas, J. Temperature and Density Effects on the Collision-Induced Depolarized Rayleigh Line-Shapes of Liquid Carbon-Disulfide. *J. Chem. Phys.* **1984**, *80*, 570-571.

(23) Fleury, P. A.; Daniels, W. B.; Worlock, J. M. Density and Temperature Dependence of Intermolecular Light Scattering in Simple Fluids. *Phys. Rev. Lett.* **1971**, *27*, 1493-1496.

(24) Hegemann, B.; Jonas, J. Separation of Temperature and Density Effects on Collision-Induced Rayleigh and Raman Line-Shapes of Liquid Carbon-Disulfide. *J. Chem. Phys.* **1985**, *82*, 2845-2855.

(25) Madden, P. A.; Cox, T. I. A Comparative-Study of the Interaction-Induced Spectra of Liquid CS_2. 2. Lineshapes. *Mol. Phys.* **1981**, *43*, 287-305.

(26) Murry, R. L.; Fourkas, J. T.; Keyes, T. Nonresonant Intermolecular Spectroscopy Beyond the Placzek Approximation. II. Fifth-Order Spectroscopy. *J. Chem. Phys.* **1998**, *109*, 7913-7922.

(27) Murry, R. L.; Fourkas, J. T.; Keyes, T. Nonresonant Intermolecular Spectroscopy Beyond the Placzek Approximation. I. Third-Order Spectroscopy. *J. Chem. Phys.* **1998**, *109*, 2814-2825.

(28) Murry, R. L.; Fourkas, J. T.; Li, W.-X.; Keyes, T. Mechanisms of Light Scattering in Supercooled Liquids. *Phys. Rev. Lett.* **1999**, *83*, 3550-3553.

(29) Ladanyi, B. M.; Barreau, A.; Dumon, B. Density and Temperature Dependence of Spectral Moments in Depolarized Light Scattering by Rare Gases. *Mol. Phys.* **1992**, *77*, 735-767.

(30) Ladanyi, B. M. Molecular-Dynamics Study of Rayleigh Light-Scattering from Molecular Fluids. *J. Chem. Phys.* **1983**, *78*, 2189-2203.

(31) Neelakandan, M.; Pant, D.; Quitevis, E. L. Reorientational and Intermolecular Dynamics in Binary Liquid Mixtures of Hexafluorobenzene and Benzene: Femtosecond Optical Kerr Effect Measurements. *Chem. Phys. Lett.* **1997**, *265*, 283-292.

(32) Heisler, I. A.; Meech, S. R. Low-Frequency Isotropic and Anisotropic Raman Spectra of Aromatic Liquids. *J. Chem. Phys.* **2010**, *132*, 174503.

(33) Smith, N. A.; Lin, S. J.; Meech, S. R.; Shirota, H.; Yoshihara, K. Ultrafast Dynamics of Liquid Anilines Studied by the Optical Kerr Effect. *J. Phys. Chem. A* **1997**, *101*, 9578-9586.

(34) Manfred, K.; He, X. X.; Fourkas, J. T. Assessing the Role of Moment of Inertia in Optical Kerr Effect Spectroscopy. *J. Phys. Chem. B* **2010**, *114*, 12096-12103.

(35) Ryu, S.; Stratt, R. M. A Case Study in the Molecular Interpretation of Optical Kerr Effect Spectra: Instantaneous-Normal-Mode Analysis of the OKE Spectrum of Liquid Benzene. *J. Phys. Chem. B* **2004**, *108*, 6782-6795.

(36) Elola, M. D.; Ladanyi, B. M. Polarizability Response in Polar Solvents: Molecular-Dynamics Simulations of Acetonitrile and Chloroform. *J. Chem. Phys.* **2005**, *122*, 224506.

(37) Bender, J. S.; Coasne, B.; Fourkas, J. T. Assessing Polarizability Models for the Simulation of Low-Frequency Raman Spectra of Benzene. *J. Phys. Chem. B* **2015**, *119*, 9345-9358.

(38) Zhu, X.; Farrer, R. A.; Fourkas, J. T. Ultrafast Orientational Dynamics of Nanoconfined Benzene. *J. Phys. Chem. B* **2005**, *109*, 12724-12730.

(39) Mcmorrow, D.; Lotshaw, W. T. Evidence for Low-Frequency (~15 Cm^{-1}) Collective Modes in Benzene and Pyridine Liquids. *Chem. Phys. Lett.* **1993**, *201*, 369-376.

(40) Elola, M. D.; Ladanyi, B. M. Molecular Dynamics Study of Polarizability Anisotropy Relaxation in Aromatic Liquids and Its Connection with Local Structure. *J. Phys. Chem. B* **2006**, *110*, 15525-15541.

(41) Elola, M. D.; Ladanyi, B. M.; Scodinu, A.; Loughnane, B. J.; Fourkas, J. T. Effects of Molecular Association on Polarizability Relaxation in Liquid Mixtures of Benzene and Hexafluorobenzene. *J. Phys. Chem. B* **2005**, *109*, 24085-24099.

(42) Chelli, R.; Cardini, G.; Ricci, M.; Bartolini, P.; Righini, R.; Califano, S. The Fast Dynamics of Benzene in the Liquid Phase. Part II. A Molecular Dynamics Simulation. *Phys. Chem. Chem. Phys.* **2001**, *3*, 2803-2810.

(43) Bonnaud, P.; Nieto-Draghi, C.; Ungerer, P. Anisotropic United Atom Model Including the Electrostatic Interactions of Benzene. *J. Phys. Chem. B* **2007**, *111*, 3730-3741.

(44) Smith, W.; Yong, C. W.; Rodger, P. M. DL_POLY: Application to Molecular Simulation. *Mol. Simulat.* **2002**, *28*, 385-471.

(45) Allen, M. P.; Tildesley, D. J. *Computer Simulation of Liquids*; Oxford University Press: New York, NY, 1989.

(46) Forester, T. R.; Smith, W. SHAKE, Rattle, and Roll: Efficient Constraint Algorithms for Linked Rigid Bodies. *J. Comput. Chem.* **1998**, *19*, 102-111.

(47) Fincham, D. Leapfrog Rotational Algorithms. *Mol. Simulat.* **1992**, *8*, 165-178.

(48) Nosé, S. A Unified Formulation of the Constant Temperature Molecular Dynamics Methods. *J. Chem. Phys.* **1984**, *81*, 511-519.

(49) Hoover, W. G. Canonical Dynamics: Equilibrium Phase-Space Distributions. *Phys. Rev. A: At. Mol. Opt. Phys.* **1985**, *31*, 1695-1697.

(50) Polt, A.; Platzer, B.; Maurer, G. The Bender Equation of State for 14 Polyatomic Fluids. *Chem. Tech. (Leipzig)* **1992**, *44*, 216-224.

(51) Alms, G. R.; Burnham, A. K.; Flygare, W. H. Measurement of Dispersion in Polarizability Anisotropies. *J. Chem. Phys.* **1975**, *63*, 3321-3326.

(52) Mossa, S.; Ruocco, G.; Sampoli, M. Orientational and Induced Contributions to the Depolarized Rayleigh Spectra of Liquid and Supercooled Ortho-Terphenyl. *J. Chem. Phys.* **2002**, *117*, 3289-3295.

(53) Hu, Z. H.; Huang, X. H.; Annapureddy, H. V. R.; Margulis, C. J. Molecular Dynamics Study of the Temperature-Dependent Optical Kerr Effect Spectra and Intermolecular Dynamics of Room Temperature Ionic Liquid 1-methoxyethylpyridinium Dicyanoamide. *J. Phys. Chem. B* **2008**, *112*, 7837-7849.

(54) Anderson, E.; Bai, Z.; Bischof, C.; Blackford, S.; Demmel, J.; Dongarra, J.; Du Croz, J.; Greenbaum, A.; Hammarling, S.; McKenney, A. et al. *LAPACK Users' Guide*, 3 ed.; Society for Industrial and Applied Mathematics: Philadelphia, PA, 1999.

(55) Loughnane, B. J.; Scodinu, A.; Farrer, R. A.; Fourkas, J. T.; Mohanty, U. Exponential Intermolecular Dynamics in Optical Kerr Effect Spectroscopy of Small-Molecule Liquids. *J. Chem. Phys.* **1999**, *111*, 2686-2694.

(56) The amplitude of the long-time, diffusive orientational decay for the decay curve of the densest liquid is significantly smaller than the amplitudes of the decays for the other liquids, which are essentially constant. Table S4 gives the fit parameters for the constant-temperature OKE TCFs. If the fit amplitude is erroneously small, the diffusive reorientational portion of the TCF would not be completely removed before Fourier transformation, resulting in a sharp peak at low frequency. It is worth noting, however, that a phenomenon similar to this peak has been observed experimentally in supercooled aromatic liquids. See reference 9.

(57) Bucaro, J. A.; Litovitz, T. A. Rayleigh Scattering: Collisional Motions in Liquids. *J. Chem. Phys.* **1971**, *54*, 3846-3853.

(58) Chandler, D. Structures of Molecular Liquids. *Annu. Rev. Phys. Chem.* **1978**, *29*, 441-471.

Chapter 6: Optical Probing of the Density of a Confined Liquid

Adapted from: in preparation for publication
Research designed by: John S. Bender and Xiaoxiao He
Research conducted by: John S. Bender and Samuel R. Cohen
Authored by: John S. Bender

6.1 *Introduction*

Liquids confined at the molecular distance scale are ubiquitous in Nature and play an important role in many technologies. Confined liquids play important roles in areas that include the biological, physical, chemical, geological, and materials sciences. Understanding the novel structural, dynamic and thermodynamic behavior that confinement induces in liquids is therefore a problem of broad interest and importance.[1-7]

One fundamental property that characterizes a liquid is its density. Remarkably, there is no consensus as to whether confined liquids tend to be more or less dense than their bulk counterparts. From an experimental perspective, there is no rigorous means of measuring the accessible volume of a nanoporous material. Accessible volume measurements are typically performed using adsorption of a material such as nitrogen, argon or mercury.[8-11] However, there is no guarantee that the volume that is accessible to these substances is the same as that for another liquid. Furthermore, if the density of the substance used to measure the accessible volume differs from that of the bulk, then the volume measurement will be miscalibrated.

An alternative approach to the experimental measurement of the density of confined liquids is the use of small-angle neutron scattering (SANS).[12-16] Liu *et al.* used this technique to observe the density minimum in supercooled water confined in

nanoporous MCM-41,[15] and concluded that the liquid is densified in this medium.[16] Morineau *et al.* studied toluene confined in MCM-41 and SBA-15 and concluded that whereas the density of this liquid in confinement is nearly identical to that of the bulk liquid at room temperature, at lower temperature the density of the confined liquid is lower than that of the bulk liquid.[13] Morineau *et al.* concluded that the density of methanol confined in MCM-41 is 8% lower than that of the bulk.[12] Xia *et al.* similarly concluded that the density of benzene confined in MCM-41 is lower than that of the bulk liquid.[14] It should be noted, however, that in the cases of benzene and methanol, the liquid pressures corresponding to the inferred densities lie at or below the estimated liquid/vapor spinodal for the bulk.[17] Furthermore, in the case of benzene, the pressure of the liquid corresponding to the reported density lies below its measured tensile strength.[18,19]

SANS measurements rely on contrast-matching conditions to determine the density of confined liquids,[12-16] in essence measuring this density from the perspective of the confining matrix rather than from the perspective of the liquid itself. The Bragg peak resulting from the ordered nanopores is monitored, and the change in scattering intensity between the empty and filled pores is related to the density of the liquid. Therefore, the density of the confined liquid is deduced from the scattering properties of the matrix rather than those of the liquid itself. These experiments require accurate knowledge of the neutron scattering length density of the confining matrix. In the case of nanoporous silicate glasses, the pore surfaces are hydroxylated, making the scattering length density heterogeneous. Therefore, it is difficult to determine the average scattering length density for the nanopores. Additionally, porous silicate glasses have inaccessible pore volume,[11]

which also contributes to the scattering intensity. Thus, as is the case in adsorption measurements, there is no rigorous determination of the accessible volume in SANS contrast-matching experiments. Both of these effects lead to a calculated density that is smaller than the actual density.

The rigorous determination of the density of simulated confined liquids is equally challenging. Simulations indicate that confined liquids typically undergo extensive layering, wherein the surface layer is densified and the subsequent layers tend toward the bulk density.[20-23] Although the radial density profile of a confined liquid could in principle be integrated to determine the average density, there is no *a priori* method for determining where to begin this integration in the vicinity of the pore wall.[21] In essence, simulations and experiments both suffer from the same inability to determine a rigorous accessible volume.

We propose the use of the local collective dynamics (librations) of a confined liquid to measure its density. Librational motions are an inherent property of a liquid that are dependent upon its density. Librational dynamics therefore provides an opportunity to measure density from the perspective of the confined liquid, without requiring any knowledge of the accessible volume of the confining material.

The optical Kerr effect (OKE) reduced spectral density (RSD) of a liquid is related directly to the depolarized, Bose-Einstein-corrected, low-frequency Raman spectrum, and therefore can be used to probe the liquid's Raman-active librations. We have recently demonstrated, through both experiment and simulation, that the OKE RSD of bulk liquid benzene can be used to determine the liquid's density. In particular, we

showed that a common OKE RSD lineshape analysis[24-28] can be used to determine the density of liquid benzene.[29] This analysis involves fitting the RSD to the sum of the so-called Bucaro-Litovitz (BL)[30] and antisymmetrized Gaussian (AG)[31] functions. The BL function models the low-frequency components of the RSD, and the AG function describes the high-frequency components. We found that the characteristic frequency of the AG function is related directly to the density of liquid benzene, whereas the width of the AG function is related directly to temperature.

Here we use OKE RSDs to study the density of benzene confined in nanoporous, silica sol-gel monoliths. The high-frequency edge of the RSD shifts to the blue with increasing confinement, and lineshape analysis suggests that the density increases linearly with pore curvature. To complement these experiments, we have also performed molecular dynamics (MD) simulations of benzene confined in cylindrical silica pores. The tumbling vibrational density of states (VDOS), which is related to the librations observed in OKE spectroscopy, exhibits the same behavior as does the OKE RSD for confined benzene. We also find that the evolution of the structure of benzene with increasing confinement is consistent with densification, further supporting the picture of densification of this liquid upon confinement.

6.2 *Experimental Details*

6.2.1 *Sol Gel Synthesis, Processing, and Impregnation*

Nanoporous sol-gel monoliths were synthesized according to a process described elsewhere.[32,33] Briefly, water was rapidly mixed into tetraethyl orthosilicate (TEOS) and ethanol in a 12:1:2 molar ratio. 8.05×10^{-4} moles of HCl (37% v/v) were then added to

the solution. The resultant acidic solution was continuously mixed for 40 min at 40 °C. After this mixing period, the solution was placed in an ice bath and another 12 moles of water were added with an amount of NH_4OH (28% v/v). Hydrolysis of TEOS was completed under basic conditions. The amount of base added was controlled to produce monoliths with varying pore size distributions. For monoliths with the smallest pore size distribution, 9.00×10^{-4} moles of NH_4OH was added. 1.80×10^{-3} moles of NH_4OH was added for intermediate sized pores. A 3.60×10^{-4} mole aliquot of base was added for monoliths with the largest pore size distribution. Once the basic solution was well mixed, the solution was poured into cylindrical containers that were sealed for aging.

Monoliths with the smallest pore size were aged at room temperature for one week. Monoliths with the medium and largest pore sizes were aged for one month in a 55 °C oven. Monoliths with the largest pore size were soaked in a 0.1 M solution of NH_4OH for 24 hours before aging. After aging, the sol-gels were slowly dried by controlling evaporation of the solvent. During the drying process, the sol-gel monoliths shrink and harden. The dried monoliths were tempered by baking them in a programmable oven (Lindberg/Blue). The temperature was ramped to 800 °C at a rate of 0.5 °C/min. The sol-gels were then baked at 800 °C for 24 hours before ramping the temperature back to room temperature at 0.5 °C/min. The average pore diameters of the prepared monoliths used in these experiments were 57 Å, 42 Å, 31 Å, and 24 Å as measured with a Bunauer-Emmett-Teller sorptometer (Micrometrics TriStar 3020 Surface Area Analyzer).

To obtain monoliths of the desired thickness for OKE experiments, 2-cm-long tempered sol-gel cylinders were cut into 5.0-mm-long pieces with a diamond saw and then were ground with sandpaper to 2.0 mm in thickness. The disks were then polished

with 20 μm, 15 μm, and 6 μm grit diamond paste, successively, until the surfaces were of optical quality. Organic impurities from the polishing process were removed by high-temperature treatment (at 500 °C in a programmable oven for 48 hours). Once the heating process was finished, the glasses were allowed to cool to room temperature (24 hours).

Air and residual water were removed from the discs under vacuum. The discs were then immediately submerged in analytical grade benzene (Sigma Aldrich, +99.8%) that had been passed through a 0.2 μm filter. The discs were soaked for at least 24 hours and then were placed in a 2.0-mm-pathlength optical glass cuvette. The discs were immersed in benzene, and the cuvette was hermetically sealed with a Teflon cap and quick setting epoxy.

6.2.2 *OHD-OKE Spectrometer*

The OHD-OKE spectrometer was described in Chapter 3. These experiments were performed using nearly-transform-limited 44 fs laser pulses centered at a wavelength of approximately 810 nm.

6.2.3 *Data Collection*

OHD-OKE decays were measured using two different scan lengths, each with equally-spaced data points. To characterize the slower, diffusive orientational dynamics, scans with a time delay of 6.67 fs/step were performed. To characterize the more rapid inertial and intermolecular dynamics, scans with a spacing of 0.667 fs/step were performed. Spectra were collected at opposite heterodyne angles in immediate succession and combined to form one data set prior to analysis. All spectra were collected at 295.6 K. Thirty long-time-step and four short-time-step scans were performed for each sample.

To characterize the laser pulse, intensity autocorrelations were measured through second-harmonic-generation in a KDP crystal using 0.667 fs/step time resolution. Four autocorrelation scans were averaged to determine the laser pulse shape. This measurement was made once before data collection and once after to ensure that the pulse shape remained constant throughout the experiment.

6.2.4 *Data Analysis*

To calculate the RSDs for the confined liquid, long-time-step OKE decays were integrated to determine the collective orientational correlation function, $C_{coll}(\tau)$,[34,35] where τ is the experimental delay time between the pump and probe pulses. To remove the diffusive dynamics from the experimental decays, $C_{coll}(\tau)$ was fitted to the sum of two exponential functions at times greater than 3 ps (Figure 6.1). This function takes the form

$$A\left[Be^{-\tau/\tau_1} + (1-B)e^{-\tau/\tau_2}\right], \tag{6.1}$$

where the amplitude B is less than unity, A is a scaling factor, τ_1 is the shorter decay time, and τ_2 is the longer decay time. In accordance with previous results, the longer of the two exponential decays was constrained to have a decay time of 33.33 ps. These fits were used to splice a tail onto the short-time-step decays. The resultant data were then transformed to produce the RSD via a Fourier deconvolution technique,[36] using the laser-pulse autocorrelations and the OKE decays.

6.3 *Simulation Details*

6.3.1 *Intermolecular Potentials*

All intermolecular interactions were computed through the sum of the Lennard-Jones and Coulomb potentials (See eq 4.8). The nine-site anisotropic united atom model

developed by Bonnaud *et al.* was used to simulate benzene.[37] This model accurately reproduces the thermodynamics, molecular dynamics, and liquid structure of bulk benzene. Included in the model are nine interaction sites; one site for each of the methine groups in the ring and three charged sites to mimic the interactions of the π system of the molecule. The charged sites consist of a positive charge at the center-of-mass of the molecule and two negative charges displaced ±0.4 Å along the surface normal through the center-of-mass and on either side of the molecular plane. The geometry and model parameters for this benzene potential have been listed elsewhere.[29,37,38] The intermolecular potential parameters for the silica have been listed elsewhere.[39] The Lennard-Jones parameters for interactions between unlike atoms were computed according to the Lorentz-Berthelot combination rules.

6.3.2 *Preparation of Nanopores*

The nanopore simulation model was provided by our collaborator, Dr. Benoit Coasne. The nanopore simulation model will be described here briefly. Canonical Monte Carlo (CMC) simulations and geometric carving were used to prepare amorphous silica nanopores. Starting from a cube of crystalline silica measuring 71.6 Å on each side, a simulated annealing process was performed to produce a cube of amorphous silica. MC simulations of the cube were performed from temperatures ranging from 5000 K to 293 K to simulate annealing in the following manner. CMC simulations were run at each temperature, for which 10 blocks of 10^5 trials were performed. After each simulation was completed, the temperature was lowered by one percent of the previous value. At 293 K, a cubic block of amorphous silica was produced. A cylindrical nanopore was then carved out of the cube by removing silica atoms for which $(x^2 + y^2)^{1/2} < D/2$. Here, D is the

nominal pore diameter, and *x* and *y* are the atomic coordinates of the silica atom in the respective Cartesian space. The result of this process was a cylindrical pore directed along the *z* axis of the cube of amorphous silica. All Si atoms that were not in a complete tetrahedral environment were then removed, as were all non-bonded O atoms. The surface of the pore was hydroxylated by choosing dangling O atoms at random and coordinating H atoms with them. The surface density of hydroxyl groups was ~4 per nm^2, which is typical for silica surfaces.[40,41] The remaining dangling O atoms were removed by replacing nearest neighbor pairs of dangling O atoms with one O atom placed at the center-of-mass of the pair. This procedure ensures that all O atoms participate in a siloxane bridge or a silanol group. The final pore architecture was then relaxed using MD simulations. Five cylindrical pores were prepared in this manner, with nominal pore diameters of 24 Å, 28 Å, 32 Å, 36 Å, and 48 Å.

6.3.3 *Adsorption of Benzene*

Grand Canonical Monte Carlo (GCMC) simulations were performed to simulate the adsorption of benzene in the silica nanopores. During the GCMC simulations, the Si, O, and H atoms of the silica were frozen (i.e. these atoms were restricted to one atomic position in Cartesian space) and the temperature was set to 293 K. The pressure of the liquid reservoir was 10,000 Pa, which is close to the saturating vapor pressure for benzene at 293 K. The pores were considered full when equilibrium was reached between the benzene molecules in the pore and the bulk liquid. Table 6.1 gives the number of adsorbed molecules in each pore.

Table 6.1 Number of molecules (N_{mol}) adsorbed in simulated silica nanopores.

Pore Diameter (Å)	N_{mol}
24	202
28	279
32	369
36	470
48	844

6.3.4 *MD Simulations*

The filled pores were used in MD simulations to investigate the dynamics and structure of confined benzene. DL_POLY V_2[42] was used to run equilibration simulations in the NVT ensemble with a Nosé-Hoover thermostat[43,44] set at 293 K. These runs lasted 1 ns (200,000 integration steps). After equilibration, 1 ns runs were performed in the NVE ensemble with no thermostat and the same integration step size. The interaction cutoff length was set to 35.8 Å. The long-range electrostatic interactions were calculated using the Ewald summation method, which was automatically optimized by DL_POLY V_2[42] to within 10^{-5} precision. The silica atoms were frozen and the benzene molecules were rigid. The Verlet Leapfrog algorithm was used to integrate the equations of motion every 5 fs.[45] The SHAKE algorithm[46] was used for bond constraints during translation, and Fincham's implicit quaternion algorithm[47] was used for rigid-body rotation.

MD simulations of bulk benzene at a constant temperature of 293 K and varying density were also performed. Six different densities were investigated: 0.922, 0.898,

0.884, 0.874, 0.850, 0.831, and 0.812 g/mL. The simulation boxes measured 30 Å on each side, corresponding to 192, 187, 184, 182, 177, 173, and 169 molecules at the respective densities. Cubic periodic boundary conditions were employed with an interaction cutoff length of 15 Å. All other simulation parameters were identical to those in the simulations of confined benzene.

6.4 *Results and Discussion*

6.4.1 *Experiment*

OKE spectroscopy is the time domain analog of depolarized Raman scattering, and through a well-known Fourier transform technique,[36] the RSD can be calculated from the time-domain decay. OKE spectroscopy has been used to study a wide range of liquids confined in silica sol-gel monoliths, which contain tortuous, interconnected cylindrical nanopores.[33,35,48-51] These studies have shown that confined liquids exhibit heterogeneous dynamics. In all cases, the diffusive relaxation is slowed relative to the bulk liquid dynamics. These slower dynamics arise from several mechanisms, including geometric effects, chemical interactions with the pore surfaces, and disruption of collective motions. The diffusive dynamics generally occur on a time scale of 1 ps or longer, but OKE spectroscopy is also sensitive to non-diffusive dynamics that occur on time scales up to a few ps. These non-diffusive dynamics, which are best visualized in the RSD, are expected to be affected by confinement as well. The OKE spectroscopy of benzene, both in the bulk and confined, has been studied extensively through experiment[24-27,29,51-57] and simulation.[21,28,38,58-60] The high-frequency portion of the RSD for this typical van der

Waals liquid is dominated by librational character,[29] making this liquid an ideal test case for using OKE spectroscopy to measure density in confinement.

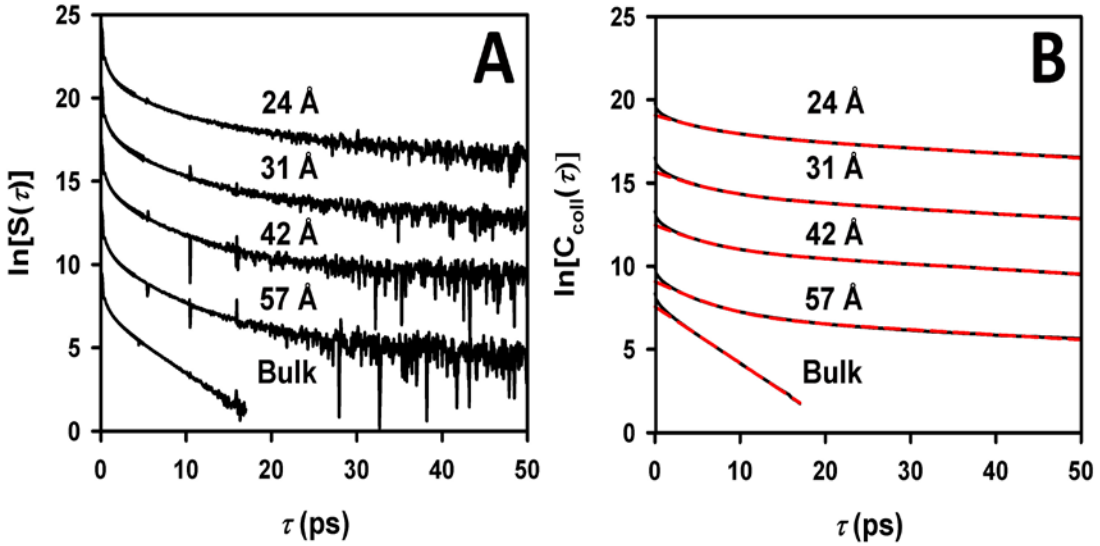

Figure 6.1 Semilogarithmic plots of experimental (A) OKE decays and (B) integrated decays (black) with biexponential fits (dashed red) for confined benzene. The curves are offset for clarity.

Table 6.2 Parameters for constrained biexponential fits to experimental integrated OKE decays for benzene confined in amorphous silica nanopores. $\mathbf{A_1}$ and $\mathbf{A_2}$ have been normalized to sum to unity. The numbers in parentheses are estimated uncertainties in the last digit.

D (Å)	D^{-1} ($Å^{-1}$)	A_1	τ_1 (ps)	A_2	τ_2 (ps)
24(2)	0.042(4)	0.660(7)	4.6(2)	0.340(8)	33.3(7)
31(3)	0.032(3)	0.726(7)	4.2(1)	0.274(4)	33.3(5)
42(4)	0.024(2)	0.763(6)	3.88(8)	0.237(3)	33.3(7)
57(6)	0.018(2)	0.865(7)	3.7(1)	0.14(1)	33(1)
Bulk	0	1.000(3)	2.95(1)		

The raw time-domain data, from which the RSDs are derived, are shown in Figure 6.1, and the exponential fit parameters are given in Table 6.2. In agreement with previous experiments, the long-time tail of the OKE decays of confined benzene is characterized by the sum of two exponentials.[51] The smaller decay constant, which increases with increasing pore curvature, is associated with the liquid in the centers of the silica pores.

The larger decay constant, which is insensitive to pore curvature, is attributed to molecules at the surfaces of the pores.[51]

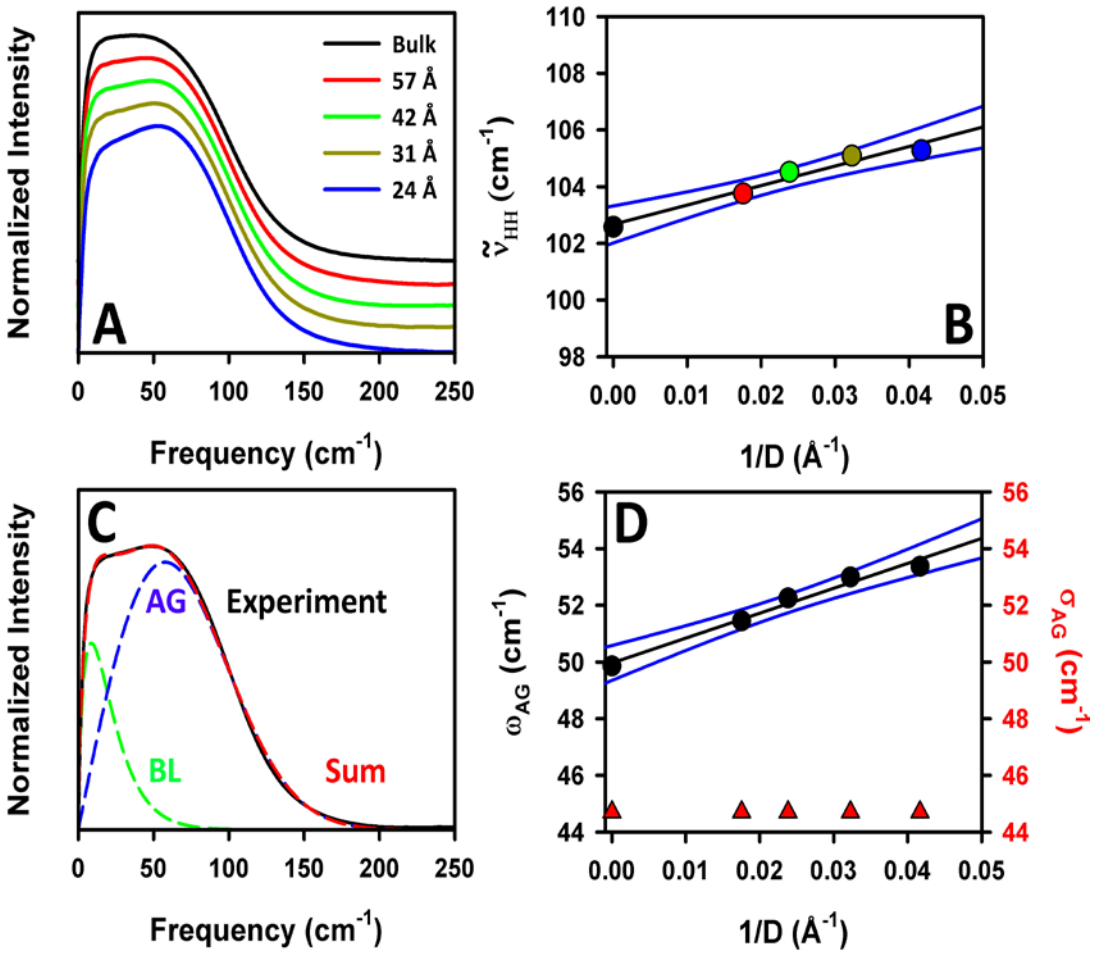

Figure 6.2 Plots of (A) RSDs for benzene confined in amorphous silica sol-gel monoliths, (B) the frequency-at-half-height for the RSDs of confined benzene as a function of average pore curvature, (C) a typical fit of the BL and AG functions to an experimental RSD, and (D) the constrained AG function parameters as a function of confining pore curvature. The black lines in (B) and (D) are linear regressions to the data, and the blue lines are the 95% prediction bands for the fits to the data.

Figure 6.2A shows the experimental RSDs for confined benzene, which display two features that evolve with increasing confinement. First, the low-frequency side of the spectrum decreases in relative intensity. This phenomenon may be due to a decrease in collective motion within the liquid at the surfaces of the silica pores (i.e., interactions at the pore surfaces reduce the accessibility of collective modes within the liquid). Second,

the high-frequency edge of the spectrum shows a blue shift. Figure 6.2B shows that the frequency-at-half-height ($\tilde{\nu}_{HH}$) of the high-frequency side of the spectrum increases linearly as a function of pore curvature. The 95% prediction band associated with the linear regression to the data is narrow, demonstrating the strong linear correlation of $\tilde{\nu}_{HH}$ with pore curvature. The high-frequency components of the RSD have been shown to be due largely to libration, which is sensitive to the liquid structure and density.[29] As bulk benzene is cooled, the blue shift in $\tilde{\nu}_{HH}$ has been shown to be the result of densification.[29] The shift of $\tilde{\nu}_{HH}$ with increasing confinement is therefore consistent with densification.

For further characterization of the evolution of the high frequency components of the RSD with increasing confinement, we fit the RSDs to the sum of a BL function and an AG function (eq 5.3) For all fits, A_{AG} was set to unity because the true amplitude of the AG function is a result of the difference between the Gaussian functions. A representative fit to an experimental spectrum is shown in Figure 6.2C and demonstrates that the RSD is well described by this empirical formula. We are interested in the high-frequency components of the spectrum, so we will focus on the parameters associated with the AG function, which are plotted as a function of pore curvature in Figure 6.2D. The width of the AG function, σ_{AG}, was constrained to the value for the bulk liquid at the same temperature, because this parameter has been found previously to depend on temperature rather than density.[29] However, similar results are found in unconstrained fits. Figure 6.3 shows a comparison of the parameters, which are given in Tables 6.3 and 6.4, respectively, for unconstrained and constrained fits. Figure 6.3 shows that the values of σ_{AG} for the constrained fits are well within the 95% prediction band associated with the linear fit to the unconstrained parameters, and that virtually all of the correlation of the

AG function with pore size is described by ω_{AG}. Furthermore, constraining σ_{AG} to the bulk value has negligible impact on the slope of the linear correlation associated with ω_{AG} as the pore curvature increases; in fact, this correlation increases when σ_{AG} is constrained. The 95% prediction band associated with the linear regression to ω_{AG} is again narrow, showing a strong linear correlation with pore curvature, whereas the 95% prediction band for the linear regression to σ_{AG} is broad, showing weak correlation with pore curvature.

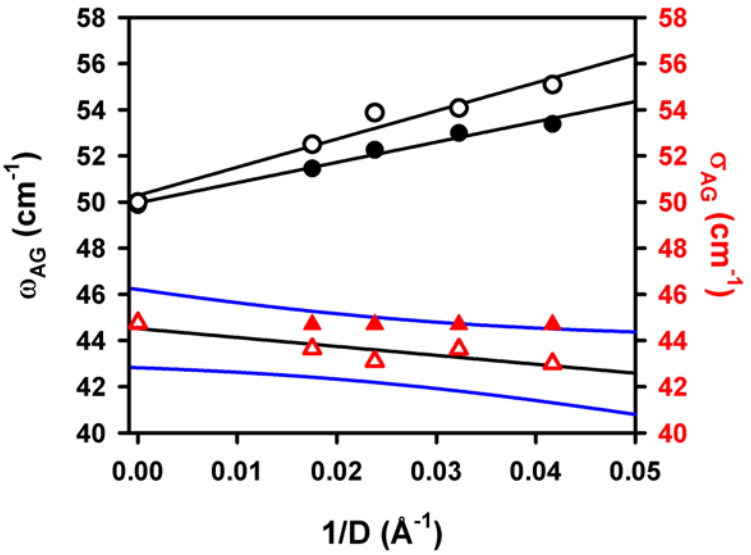

Figure 6.3 Comparison of unconstrained (open symbols) and constrained (solid symbols) fit parameters from the AG function for the RSDs of confined benzene. The black lines are linear regressions. The blue lines represent the 95% prediction band for σ_{AG} of the unconstrained fits.

Table 6.3 Parameters from unconstrained fits for RSDs of confined benzene. The numbers in parentheses are estimated uncertainties in the last digit.

D (Å)	D^{-1} ($Å^{-1}$)	A_{BL}	δ	ω_{BL} (cm^{-1})	ω_{AG} (cm^{-1})	σ (cm^{-1})
24(2)	0.042(4)	0.19(1)	0.88(5)	10.90(7)	55.1(2)	43.00(8)
31(3)	0.032(3)	0.29(3)	0.72(9)	11.8(2)	54.1(4)	43.6(2)
42(4)	0.024(2)	0.27(2)	0.77(7)	11.3(1)	53.9(3)	43.1(1)
57(6)	0.018(2)	0.29(1)	0.84(4)	11.02(6)	52.5(2)	43.64(9)
Bulk	0	0.30(1)	0.73(3)	11.8(3)	49.9(3)	44.7(3)

Table 6.4 Parameters from constrained fits for RSDs of confined benzene. The numbers in parentheses are estimated uncertainties in the last digit.

D (Å)	D^{-1} ($Å^{-1}$)	A_{BL}	δ	ω_{BL} (cm^{-1})	ω_{AG} (cm^{-1})	σ (cm^{-1})
24(2)	0.042(4)	0.20(1)	0.82(5)	11.70(9)	53.4(2)	44.7(1)
31(3)	0.032(3)	0.30(4)	0.69(1)	12.3(2)	53.0(6)	44.7(3)
42(4)	0.024(2)	0.28(3)	0.72(8)	12.1(1)	52.3(5)	44.7(2)
57(6)	0.018(2)	0.25(1)	0.80(4)	11.55(7)	51.5(2)	44.7(1)
Bulk	0	0.30(1)	0.73(3)	11.8(3)	49.9(3)	44.7(3)

As was the case for $\tilde{\nu}_{HH}$, ω_{AG} shows a strong linear correlation with pore curvature. Previous studies of bulk benzene have shown that ω_{AG} shifts linearly to higher frequency with increasing density.[24,29] Furthermore, MD simulations have shown that ω_{AG} correlates strongly with the density of bulk benzene.[29] This shift is the result of stiffening of the molecular potential as the free volume of the liquid decreases, which increases librational frequencies.[29] Therefore, the blue shift in this parameter with increasing confinement is consistent with densification of the liquid as the curvature of the confining geometry increases.

6.4.2 *Simulation*

Although the experimental RSDs for benzene exhibit a blue shift with increasing confinement that is similar to that of the bulk liquid with increasing density, we must

consider the possibility that the blue shift in confinement arises from interactions with the pore surfaces. To explore this scenario, we performed MD simulations for benzene confined in cylindrical nanopores composed of amorphous silica.

The calculation of RSDs for the simulated confined benzene requires that the collective polarizability time correlation functions (TCFs) be determined.[38] To obtain realistic spectra, such calculations must take the polarizability of the silica into account. It is impractical to use an atomistic model of the silica polarizability, and there is no simplified model available to reduce the computational cost of the calculations. An alternative approach, which has been used previously to calculate collective polarizability TCFs for acetonitrile confined in silica nanopores, is to neglect the polarizability of the silica altogether.[61] However, the response functions in that previous work were noisy enough that they could not be used to calculate RSDs.

We have decided instead to calculate the tumbling vibrational density of states ($VDOS_{TUM}$) for the simulated confined liquid. $VDOS_{TUM}$ arises from the same librational motions that contribute to the RSD, but is not weighted by their collective, depolarized Raman activity. To isolate the tumbling velocity, we take advantage of benzene's axial molecular symmetry. The velocity of the center-of-mass ($\vec{v}_{COM}$) of each molecule was first subtracted from the velocity of each of its methine groups ($\vec{v}_{CH}$). The resultant vector for each methane group $\left(\vec{v}_{CH,ANG}\right)$ arises from molecular spinning and tumbling. To isolate the tumbling velocity $\vec{v}_{CH,TUM}$, $\vec{v}_{CH,ANG}$ was projected onto a unit vector perpendicular to the plane of the benzene ring. $VDOS_{TUM}$ is then defined as

$$VDOS_{TUM} = \frac{1}{2\pi} Re\mathcal{F}\langle \vec{v}_{TUM}(0) \cdot \vec{v}_{TUM}(t)\rangle^2, \tag{6.2}$$

where $\mathcal{F}$ denotes a Fourier transform.

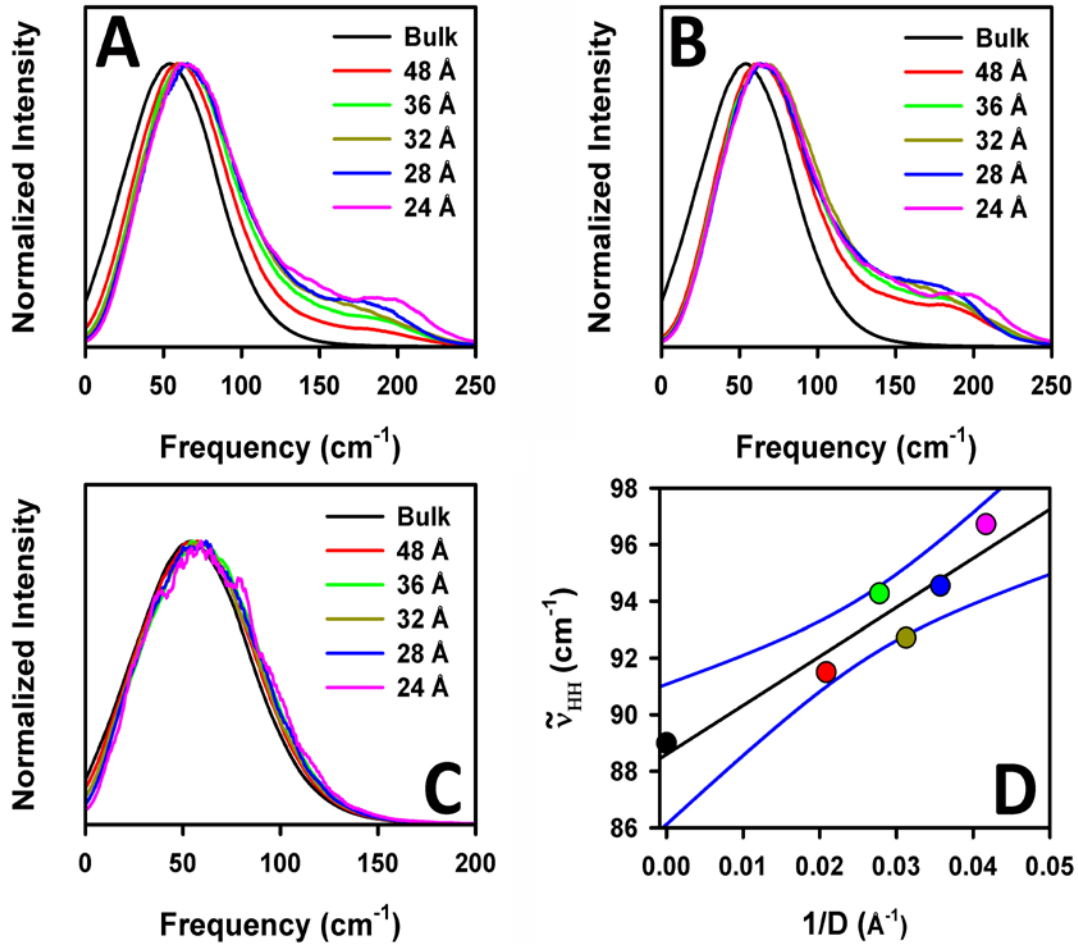

Figure 6.4 Plots of the tumbling VDOS for (A) the total population, (B) the surface population, and (C) the bulk-like population of confined benzene. (D) The frequency at half height of the VDOS for the bulk-like population of molecules confined in simulated amorphous silica nanopores. The black line in (D) is a linear regression to the data. The blue lines represent the 95% prediction values for this regression.

VDOS$_{TUM}$ of benzene confined in pores shifts to higher frequency and develops a bimodal structure with increasing pore curvature (Figure 6.4A). Compared to VDOS$_{TUM}$ for all of the confined molecules, VDOS$_{TUM}$ for molecules whose center of mass is within 10 Å of the pore surfaces exhibits a significant blue shift of the main peak and features a secondary peak at higher frequency (Figure 6.4B). This bimodal structure is the result of overemphasized hydrogen bonds at the pore surfaces. The negative charges in the

benzene model, which were designed to mimic the π cloud, have a strong Coulombic interaction with the silanol groups of the silica. Figure 6.5A shows the radial distribution function for the hydrogen atoms at the silica surface and the negative charges on the benzene molecules. Benzene molecules whose negative charges were within 2 Å of a hydrogen atom on the silica surface were defined as hydrogen bond acceptors. Figure 6.5B shows $VDOS_{TUM}$ for molecules within the first layer of the silica surface. These data indicate that the bimodal structure is the result of molecules tumbling about a donated hydrogen bond. For molecules that do not accept hydrogen bonds, there is no bimodal structure in $VDOS_{TUM}$. The interaction energy between the negative charges on the simulated benzene molecule and the silanol hydrogen is three orders of magnitude larger than the thermal energy, making these hydrogen bonds unrealistic and explains why this bimodal structure is not evident in the experimental RSDs.

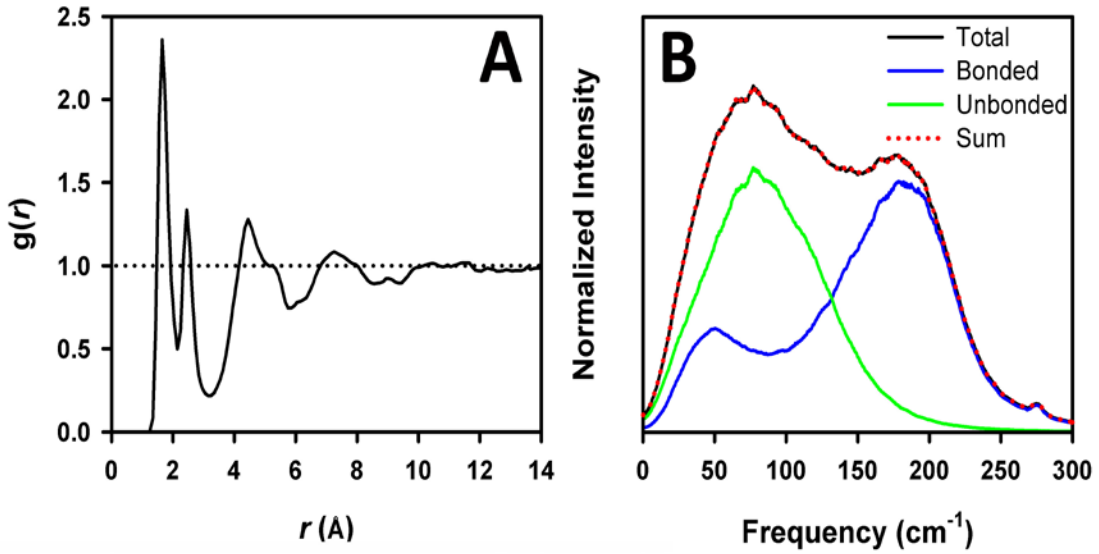

Figure 6.5 (A) The radial distribution function g(*r*) for the hydrogen atoms on the silica and the π-cloud charges on the benzene molecules. (B) $VDOS_{TUM}$ for molecules in the first layer at the silica surface.

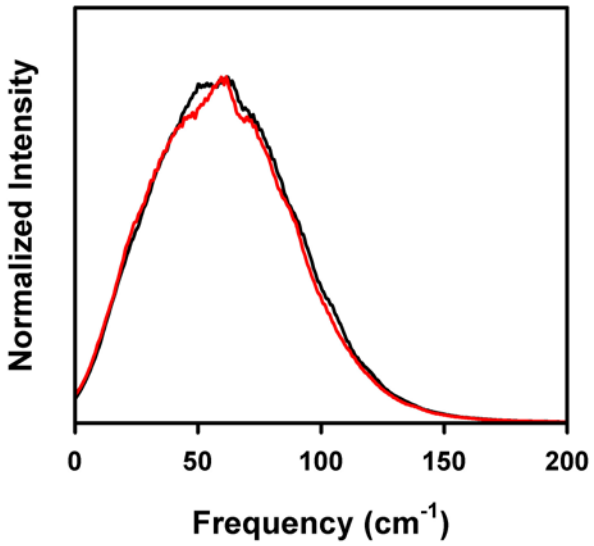

Figure 6.6 $VDOS_{TUM}$ for two starting configurations of confined benzene in a 28 Å pore.

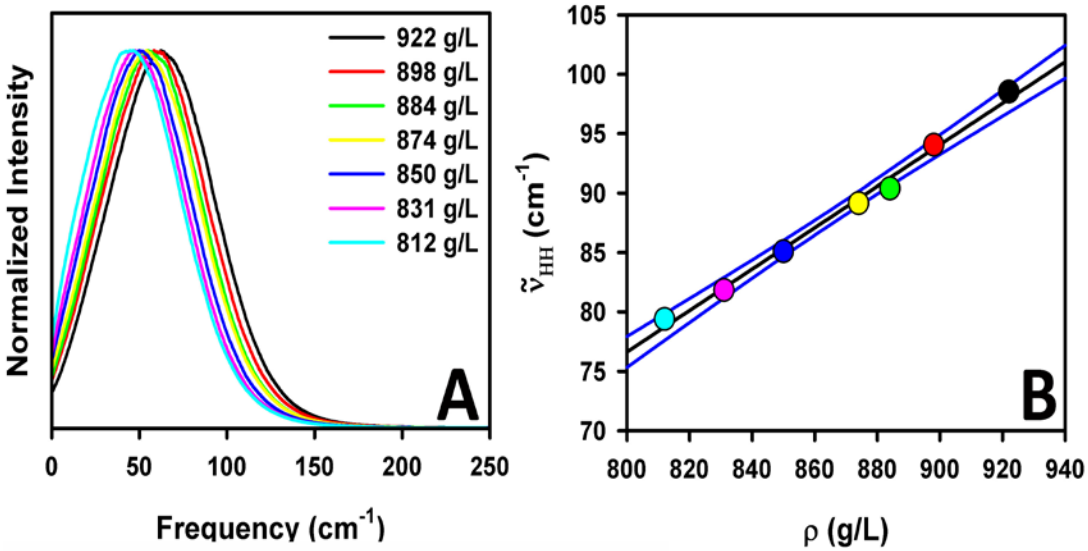

Figure 6.7 (A) $VDOS_{TUM}$ for bulk benzene at constant temperature. (B) Frequency at half-height for the high-frequency edge of the VDOS as a function of density. The solid black line in (B) is a linear least-squares fit and the blue lines represent the 95% prediction band.

Given the issues with the interactions between the pore surfaces and the confined liquid, we focus instead on the "bulk-like" population of molecules whose center of mass is more than 10 Å from the pore surfaces. $VDOS_{TUM}$ for these molecules is unimodal (Figure 6.4C), further supporting the assignment of the high-frequency mode in the surface population to hydrogen-bonded molecules. The frequency-at-half-height of the blue edge for $VDOS_{TUM}$ increases with increasing confinement (Figure 6.4D). The scatter

in the data in Figure 6.4D is the result of noise in the $VDOS_{TUM}$. Additionally, $VDOS_{TUM}$ is dependent on the starting configuration of the simulation. Figure 6.6 shows $VDOS_{TUM}$ for two starting configurations in the 28 Å pore. The spectra do not overlap completely, demonstrating the dependence of the VDOS on the initial configuration. However, within the uncertainty of the calculations, the shift in $\tilde{\nu}_{HH}$ monotonic.

Figure 6.7A shows $VDOS_{TUM}$ for bulk benzene simulated at constant temperature and several densities. These spectra shift to higher frequency with increasing density, and Figure 6.7B shows that this shift of $\tilde{\nu}_{HH}$ is linear in density. These data support the picture that the blue shift of $\tilde{\nu}_{HH}$ for the "bulk-like" molecules in confinement is consistent with densification.

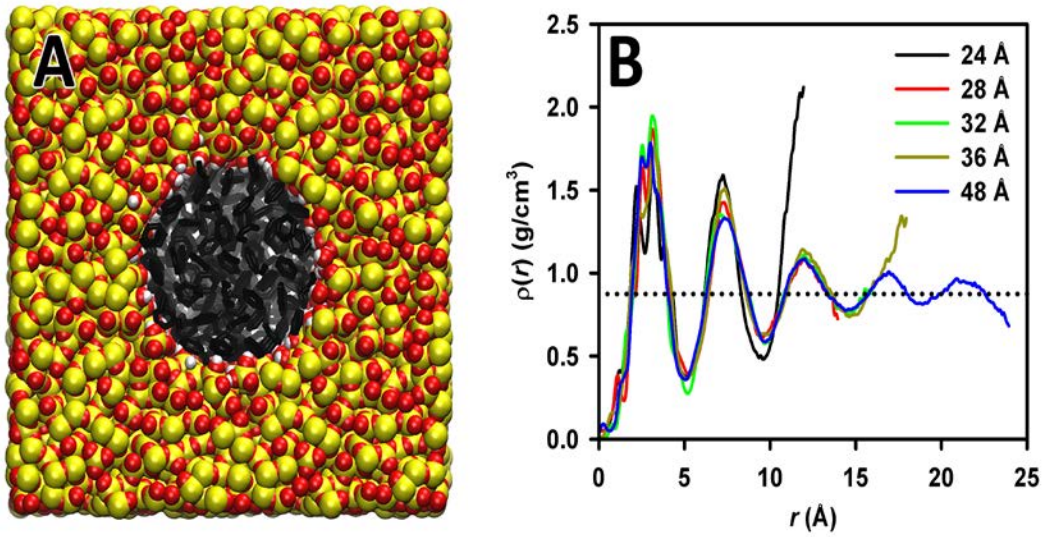

Figure 6.8 (A) Snapshot of benzene confined in a pore with a 36 Å diameter. The yellow atoms are Si, the red atoms are O, and the white atoms are H. The benzene molecules are represented as black hexagons. For clarity, the charged sites have been removed. (B) The radial density profile for benzene confined in 24 Å, 28 Å, 32 Å, 36 Å, and 48 Å silica nanopores. *r* is the nominal distance from the pore surface. The dotted line represents the bulk density, 0.874 g/cm^3.

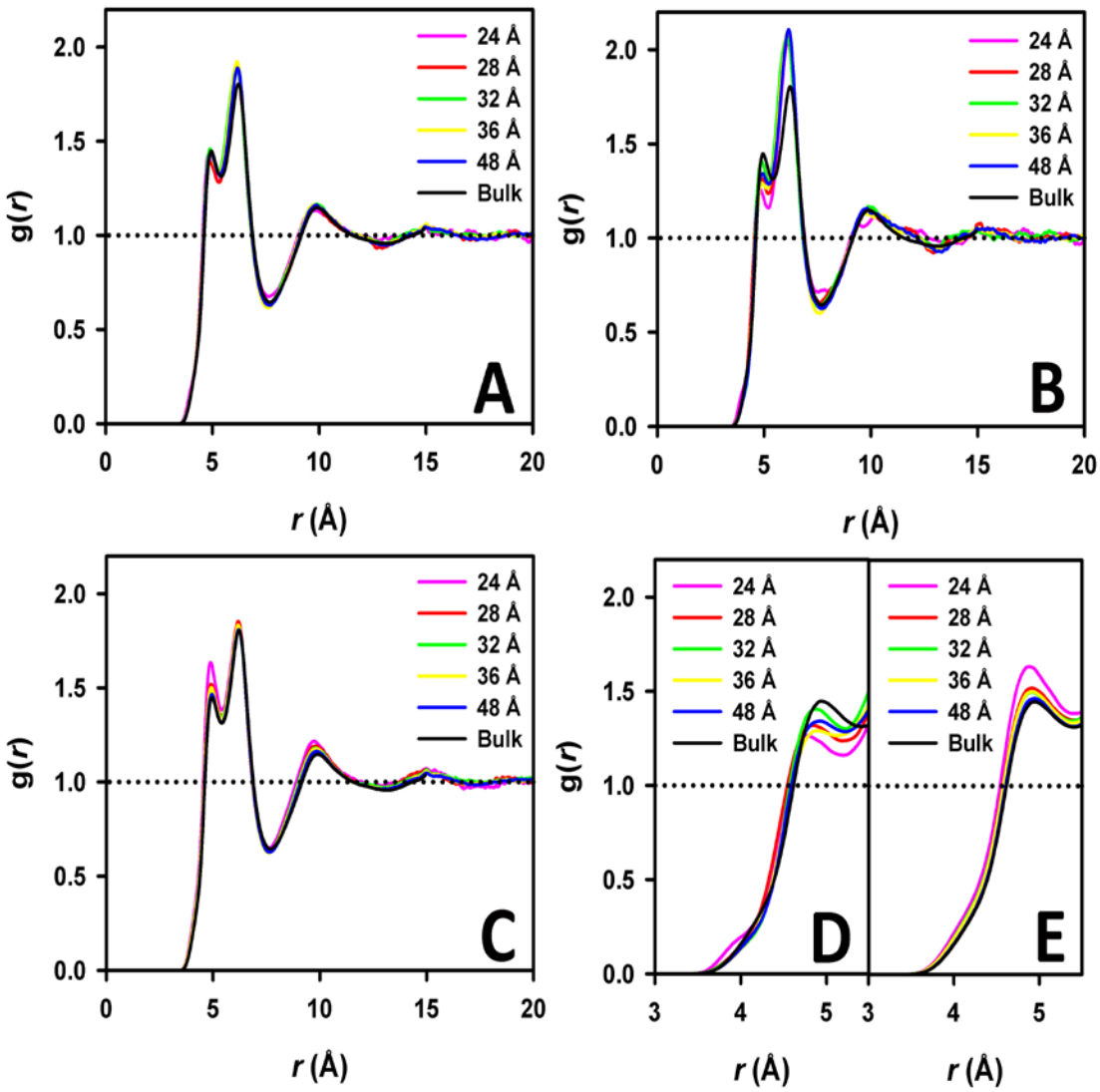

Figure 6.9 Pair-correlation functions for (A) the total confined liquid, (B) molecules at the pore surfaces, (C) molecules in the centers of the pores. Close-up of the first peak of the correlation functions for (D) surface molecules and (E) molecules in the centers of the pores.

Finally, we consider the structure of confined benzene. Figure 6.8A shows a snapshot of liquid benzene confined in a simulated pore with a 36 Å diameter. Figure 6.8B shows the center-to-center radial density profile for benzene confined in 24 Å, 28 Å, 32 Å, 36 Å, and 48 Å diameter pores. The structure of each of the confined liquids exhibits significant and nearly identical layering, extending far from the surface of the nanopore. There is fine structure in the first layer, resulting from two different

orientations at the pore surface. The first sub-peak corresponds to molecules lying parallel to the pore surface and the second sub-peak corresponds to molecules whose rings are standing orthogonal to the pore surface.[21] The anomalous density in the center of the 24 Å pore is indicative of a one-dimensional string of molecules running down the pore axis. The density of the confined liquid cannot be determined accurately by integrating the density profiles. In doing so, one must define a volume arbitrarily. Using the mathematical volume derived from the nominal pore diameter always yields a density lower than the bulk value because calculating the density in this manner does not account for the repulsive interactions at the pore walls, which effectively decrease the pore diameter.

Figure 6.9A shows the radial distribution functions for the liquid in the bulk and in pores with five different diameters. The pair-correlation functions for the confined liquid have been corrected for excluded volume effects using a method developed by Gallo *et al.*[62] At first glance, there is little change in the structure of the liquid with pore curvature, which is consistent with neutron diffraction measurments.[14] However, the organization of molecules within the vicinity of the pore surfaces differs from that of the liquid in the centers of the pores. Figure 6.9B shows the pair-correlation functions for molecules within ~10 Å of the pore surfaces. There is a decrease in correlation relative to the bulk at an r of ~5 Å with increasing pore curvature. This peak is dominated by T-shaped molecular configurations,[38] and a decrease in correlation indicates that there is a corresponding increase in parallel molecular ordering at the surface of the pore. This phenomenon reflects a preference of the molecules to lie flat at the pore surface.[21] Figure 6.9C shows the correlation functions for the "bulk-like" molecules in the centers of the

pores. The peak at ~5 Å shows the opposite behavior from that for the surface population, which exhibits a monotonic increase in correlation at ~5 Å with increasing pore curvature. Figure 6.9D shows a close-up of this peak for the surface molecules and Figure 6.9E shows the close-up for the molecules in the pore centers. The behavior exhibited in Figure 6.9C is similar to the behavior for densified bulk benzene (See Figure 5.11).[29]

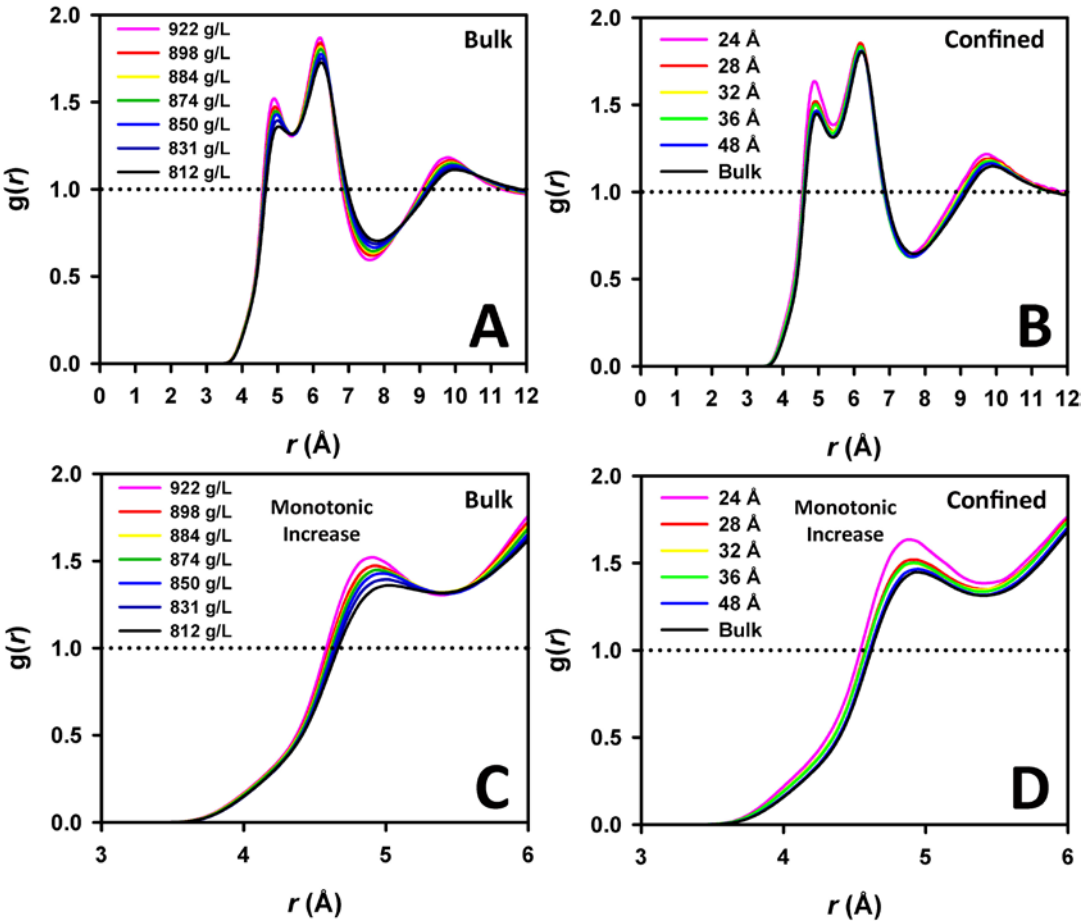

Figure 6.10 Center-to-center radial distribution functions for (A) bulk benzene simulated at 293 K at several densities and (B) confined benzene in the centers of the pores simulated at 293 K in pores of several diameters. (C) and (D) are close-ups of (A) and (B), respectively.

Figure 6.10 shows a comparison of the evolving structure for benzene simulated at constant temperature and variable density and the emerging structure of the liquid with increasing confinement. Figure 6.10A shows the pair-correlation functions for the bulk

liquid held at 293 K and at several densities. At and *r* of ~5 Å there is a monotonic increase in correlation with increasing density. For the convenience of the reader, Figure 6.10B is a reproduction of Figure 6.9C. A comparison of Figures 6.10A and 6.10B shows that the evolution of the structure of the confined liquid in the pore center as a function of pore curvature is similar to the evolution of the bulk liquid with increasing density at constant temperature. There is a shift to shorter pair distances with both increasing density and increasing pore curvature. This behavior is consistent with an increase in librational frequency, and therefore, a blue shift of the high-frequency side of the RSD. Figures 6.10C and 6.10D are close-ups of Figures 6.10A and 6.10B, respectively. A monotonic increase in the peak at and *r* of ~5 Å is shown for both the bulk liquid (6.10C) and the confined liquid (6.10D). These results are also consistent with the idea that the confined liquid in the pore centers is densified with an increase in pore curvature.

6.4.3 *Calculated Densities*

We have established that the evolution of the librational dynamics and structure of confined benzene is consistent with densification of the liquid. Assuming that confinement and temperature affect the density of benzene in the same manner, we can then calculate an estimated density from calibration curves constructed from bulk benzene experiments and simulations. For the experimental data, the linear regression in Figure 5E of reference 25 was used. Values of ω_{AG} for the fits to the RSDs of confined benzene were inserted into the equation for this curve. The same process was repeated for the simulated data, in which the curve in Figure 6.7B was used. Values of $\tilde{\nu}_{HH}$ for VDOS_{TUM} of the simulated confined benzene were used. Figure 6.11 shows the calculated densities as a function of pore curvature for benzene confined in amorphous

silica nanopores. The experimental results imply that benzene is densified by ~1.5% for the 24 Å pore relative to the bulk liquid at the room temperature. The experimental and simulated results are in qualitative agreement but diverge at high pore curvatures. The greater degree of densification observed in the simulations is probably an artifact of the strong surface interactions in this system. The simulated results show that benzene is densified by ~5% for benzene confined in a 24 Å pore.

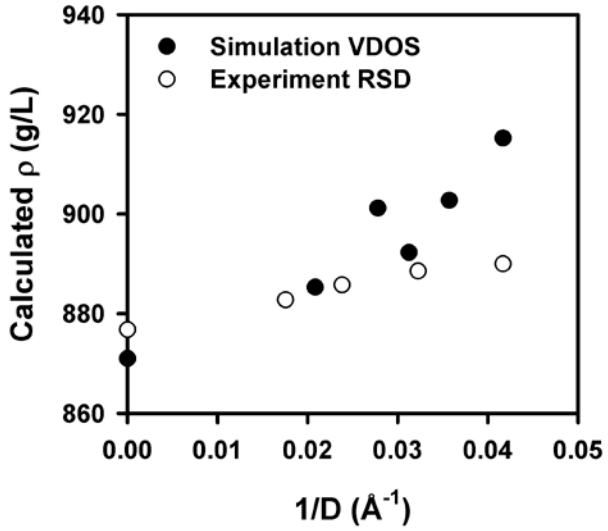

Figure 6.11 Calculated densities for benzene confined in amorphous silica nanopores. The densities are calculated using the calibrations of the experimental (open symbols) and simulated (closed symbols) data.

This picture of increased benzene density upon confinement in silica nanopores stands in contrast to the results of Xia *et al.*,[14] who found that benzene confined in crystalline silica is less dense than its bulk counterpart. As discussed above, their analysis is likely to underestimate the density of the confined liquid. Furthermore, the pore surface area increases with decreasing pore size, which increases the effects of the surface silanol groups. This phenomenon would potentially reverse the trend in the calculated density data presented by Xia *et al.*[14] The glass transition temperature of benzene confined in

MCM-41 is always higher than that of the bulk liquid,[14] which is also consistent with densification. The density of water was found to increase when confined in MCM-41.[16] Water interacts strongly with the surface of silica pores, and the molecular surface layer of water in these pores is about 15% more dense than the bulk liquid.[16] Benzene also wets silica strongly,[51] so it stands to reason that benzene confined in silica nanopores would be densified. We must note, however, that the topology of the sol-gel pores used in our experiments is different from that of MCM-41. Sol-gel silicate glasses contain interconnected cylindrical pores, whereas MCM-41 contains cylindrical pores that lie parallel to one another. It is doubtful, however, that this difference in topology would make a substantial difference in the average density of the confined liquid.

6.5 *Conclusions*

Using OKE experiments and MD simulations, we have shown that the structure and dynamics of benzene confined in amorphous silica nanopores are consistent with densification of the liquid with an increase in the curvature of the confining pore geometry. The high-frequency edge of the experimental OKE RSD shifts to higher frequency with increasing confinement, as does the simulated VDOS for molecular tumbling. The evolution of the structure of confined benzene is consistent with that of the bulk liquid at constant temperature and varying density. The effects observed in the VDOS and the pair correlation functions for molecules far from the pore surface are consistent with densification. Therefore, we conclude that benzene is densified upon confinement in amorphous silica nanopores. For benzene confined in the smallest pores studied here, the densification corresponds to what would be seen with a 14 K decrease in temperature of the bulk liquid.

We also have shown that $VDOS_{TUM}$ for confined benzene develops a bimodal structure upon confinement. This structure is the result of hydrogen bonds at the surfaces of the nanopores. This phenomenon is artificial, and results from the large charges on the benzene model developed by Bonnaud *et al*.[37] Although these charges optimize the structure of the bulk liquid, they bias the model to form unrealistically strong hydrogen bonds. Therefore, this molecular model should be reoptimized for simulations that include hydrogen-bond-donating molecules or materials.

6.6 *References*

(1) Drake, J. M.; Klafter, J.; Kopelman, R.; Awschalom, D. D. *Dynamics in Small Confining Systems*; Materials Research Society: Pittsburgh, PA, 1993; Vol. 290.

(2) Drake, J. M.; Klafter, J.; Kopelman, R.; Troian, S. M. *Dynamics in Small Confining Systems II*; Materials Research Society: Pittsburgh, PA, 1995; Vol. 366.

(3) Drake, J. M.; Klafter, J.; Kopelman, R. *Dynamics in Small Confining Systems III*; Materials Research Society: Pittsburgh, PA, 1997; Vol. 464.

(4) Drake, J. M.; Grest, G. S.; Klafter, J.; Kopelman, R. *Dynamics in Small Confining Systems IV*; Materials Research Society: Warrendale, PA, 1999; Vol. 543.

(5) Drake, J. M.; Klafter, J.; Levitz, P. E.; Overney, R. M.; Urbakh, M. *Dynamics in Small Confining Systems V*; Cambridge University Press, 2014.

(6) Drake, J. M.; Klafter, J. *Molecular Dynamics in Restricted Geometries*; Wiley: New York, NY, 1989.

(7) Farrer, R. A.; Fourkas, J. T. Orientational Dynamics of Liquids Confined in Nanoporous Sol−Gel Glasses Studied by Optical Kerr Effect Spectroscopy. *Acc. Chem. Res.* **2003**, *36*, 605-612.

(8) Haller, W. Chromatography on Glass of Controlled Pore Size. *Nature* **1965**, *206*, 693-696.

(9) Gregg, S. J.; Sing, K. S. W.; Salzberg, H. Adsorption Surface Area and Porosity. *J. Electrochem. Soc.* **1967**, *114*, 279C-279C.

(10) Iler, R. K. *The Chemistry of Silica*; Wiley: New York, NY, 1979.

(11) Brinker, C. J.; Scherer, G. W. *Sol-Gel Science: The Physics and Chemistry of Sol-Gel Processing*; Academic Press: San Diego, CA, 2013.

(12) Morineau, D.; Guégan, R.; Xia, Y.; Alba-Simionesco, C. Structure of Liquid and Glassy Methanol Confined in Cylindrical Pores. *J. Chem. Phys.* **2004**, *121*, 1466-1473.

(13) Morineau, D.; Xia, Y.; Alba-Simionesco, C. Finite-Size and Surface Effects on the Glass Transition of Liquid Toluene Confined in Cylindrical Mesopores. *J. Chem. Phys.* **2002**, *117*, 8966-8972.

(14) Xia, Y.; Dosseh, G.; Morineau, D.; Alba-Simionesco, C. Phase Diagram and Glass Transition of Confined Benzene. *J. Phys. Chem. B* **2006**, *110*, 19735-19744.

(15) Liu, D. Z.; Zhang, Y.; Chen, C. C.; Mou, C. Y.; Poole, P. H.; Chen, S. H. Observation of the Density Minimum in Deeply Supercooled Confined Water. *P. Natl. Acad. Sci. USA* **2007**, *104*, 9570-9574.

(16) Liu, D. Z.; Zhang, Y.; Liu, Y.; Wu, J. L.; Chen, C. C.; Mou, C. Y.; Chen, S. H. Density Measurement of 1-D Confined Water by Small Angle Neutron Scattering Method: Pore Size and Hydration Level Dependences. *J. Phys. Chem. B* **2008**, *112*, 4309-4312.

(17) “The spinodal for these liquids was estimated by extrapolating the isochores for several densities using the Bender equation of state. [Polt et al., *Chemische Technik* **44**,

216–224 (1992)] The function lying tangent to each of these isochores was taken as the metastable liquid spinodal. This function originates from the critical temperature on the liquid/vapor coexistence curve and extends into the negative pressure regime. The density reported for methanol at 290 K is 0.730 g/mL (8% lower than the value for the bulk liquid). The pressure corresponding to this density at 290 K is approximately -1000 atm, which is at the edge of the metastable region of the phase diagram. The density reported for benzene at 290 K is 0.811 g/mL (8% lower than the value for the bulk liquid). The pressure corresponding to this density at 290 K is approximately -945 atm, which is beyond the liquid mechanical stability."

(18) Briggs, L. J. The Limiting Negative Pressure of Acetic Acid, Benzene, Aniline, Carbon Tetrachloride, and Chloroform. *J. Chem. Phys.* **1951**, *19*, 970-972.

(19) Donoghue, J. J.; Vollrath, R. E.; Gerjuoy, E. The Tensile Strength of Benzene. *J. Chem. Phys.* **1951**, *19*, 55-61.

(20) Coasne, B.; Alba-Simionesco, C.; Audonnet, F.; Dosseh, G.; Gubbins, K. E. Molecular Simulation of the Adsorption and Structure of Benzene Confined in Mesoporous Silicas. *Adsorption* **2007**, *13*, 485-490.

(21) Coasne, B.; Fourkas, J. T. Structure and Dynamics of Benzene Confined in Silica Nanopores. *J. Phys. Chem. C* **2011**, *115*, 15471-15479.

(22) Bonnaud, P. A.; Coasne, B.; Pellenq, R. J. M. Molecular Simulation of Water Confined in Nanoporous Silica. *J. Phys.: Condens. Matter* **2010**, *22*, 284110.

(23) Victor, T.; Christiane Alba, S. Properties of a Confined Molecular Glass-Forming Liquid. *J. Phys.: Condens. Matter* **2002**, *14*, 5699.

(24) Loughnane, B. J.; Scodinu, A.; Fourkas, J. T. Temperature-Dependent Optical Kerr Effect Spectroscopy of Aromatic Liquids. *J. Phys. Chem. B* **2006**, *110*, 5708-5720.

(25) Ricci, M.; Bartolini, P.; Chelli, R.; Cardini, G.; Califano, S.; Righini, R. The Fast Dynamics of Benzene in the Liquid Phase - Part I. Optical Kerr Effect Experimental Investigation. *Phys. Chem. Chem. Phys.* **2001**, *3*, 2795-2802.

(26) Heisler, I. A.; Meech, S. R. Low-Frequency Isotropic and Anisotropic Raman Spectra of Aromatic Liquids. *J. Chem. Phys.* **2010**, *132*, 174503.

(27) Manfred, K.; He, X. X.; Fourkas, J. T. Assessing the Role of Moment of Inertia in Optical Kerr Effect Spectroscopy. *J. Phys. Chem. B* **2010**, *114*, 12096-12103.

(28) Ryu, S.; Stratt, R. M. A Case Study in the Molecular Interpretation of Optical Kerr Effect Spectra: Instantaneous-Normal-Mode Analysis of the OKE Spectrum of Liquid Benzene. *J. Phys. Chem. B* **2004**, *108*, 6782-6795.

(29) Bender, J. S.; Cohen, S. R.; He, X.; Fourkas, J. T.; Coasne, B. Toward in Situ Measurement of the Density of Liquid Benzene Using Optical Kerr Effect Spectroscopy. *J. Phys. Chem. B* **2016**, *120*, 9103-9114.

(30) Bucaro, J. A.; Litovitz, T. A. Rayleigh Scattering: Collisional Motions in Liquids. *J. Chem. Phys.* **1971**, *54*, 3846-3853.

(31) Chang, Y. J.; Castner, E. W. Intermolecular Dynamics of Substituted Benzene and Cyclohexane Liquids, Studied by Femtosecond Nonlinear-Optical Polarization Spectroscopy. *J. Phys. Chem.* **1996**, *100*, 3330-3343.

(32) Liu, G.; Li, Y.; Jonas, J. Confined Geometry Effects on Reorientational Dynamics of Molecular Liquids in Porous Silica Glasses. *J. Chem. Phys.* **1991**, *95*, 6892-6901.

(33) Loughnane, B. J.; Fourkas, J. T. Geometric Effects in the Dynamics of a Nonwetting Liquid in Microconfinement: An Optical Kerr Effect Study of Methyl Iodide in Nanporous Glasses. *J. Phys. Chem. B* **1998**, *102*, 10288-10294.

(34) Zhu, X.; Farrer, R. A.; Zhong, Q.; Fourkas, J. T. Orientational Diffusion of n-Alkyl Cyanides. *J. Phys.: Condens. Matter* **2005**, *17*, S4105.

(35) Scodinu, A.; Fourkas, J. T. Comparison of the Orientational Dynamics of Water Confined in Hydrophobic and Hydrophilic Nanopores. *J. Phys. Chem. B* **2002**, *106*, 10292-10295.

(36) McMorrow, D.; Lotshaw, W. T. Intermolecular Dynamics in Acetonitrile Probed with Femtosecond Fourier-Transform Raman-Spectroscopy. *J. Phys. Chem.* **1991**, *95*, 10395-10406.

(37) Bonnaud, P.; Nieto-Draghi, C.; Ungerer, P. Anisotropic United Atom Model Including the Electrostatic Interactions of Benzene. *J. Phys. Chem. B* **2007**, *111*, 3730-3741.

(38) Bender, J. S.; Coasne, B.; Fourkas, J. T. Assessing Polarizability Models for the Simulation of Low-Frequency Raman Spectra of Benzene. *J. Phys. Chem. B* **2015**, *119*, 9345-9358.

(39) Hill, J. R.; Sauer, J. Molecular Mechanics Potential for Silica and Zeolite Catalysts Based on ab Initio Calculations. 1. Dense and Microporous Silica. *J. Phys. Chem.* **1994**, *98*, 1238-1244.

(40) Ishikawa, T.; Matsuda, M.; Yasukawa, A.; Kandori, K.; Inagaki, S.; Fukushima, T.; Kondo, S. Surface Silanol Groups of Mesoporous Silica FSM-16. *J. Chem. Soc., Faraday Trans.* **1996**, *92*, 1985-1989.

(41) Cauvel, A.; Brunel, D.; Di Renzo, F.; Garrone, E.; Fubini, B. Hydrophobic and Hydrophilic Behavior of Micelle-Templated Mesoporous Silica. *Langmuir* **1997**, *13*, 2773-2778.

(42) Smith, W.; Yong, C. W.; Rodger, P. M. DL_POLY: Application to Molecular Simulation. *Mol. Simulat.* **2002**, *28*, 385-471.

(43) Nosé, S. A Unified Formulation of the Constant Temperature Molecular Dynamics Methods. *J. Chem. Phys.* **1984**, *81*, 511-519.

(44) Hoover, W. G. Canonical Dynamics: Equilibrium Phase-Space Distributions. *Phys. Rev. A: At. Mol. Opt. Phys.* **1985**, *31*, 1695-1697.

(45) Allen, M. P.; Tildesley, D. J. *Computer Simulation of Liquids*; Oxford University Press: New York, NY, 1989.

(46) Forester, T. R.; Smith, W. SHAKE, Rattle, and Roll: Efficient Constraint Algorithms for Linked Rigid Bodies. *J. Comput. Chem.* **1998**, *19*, 102-111.

(47) Fincham, D. Leapfrog Rotational Algorithms. *Mol. Simulat.* **1992**, *8*, 165-178.

(48) Farrer, R. A.; Loughnane, B. J.; Fourkas, J. T. Dynamics of Confined Carbon Disulfide from 165 to 310 K. *J. Phys. Chem. A* **1997**, *101*, 4005-4010.

(49) Loughnane, B. J.; Farrer, R. A.; Scodinu, A.; Fourkas, J. T. Dynamics of a Wetting Liquid in Nanopores: An Optical Kerr Effect Study of the Dynamics of Acetonitrile Confined in Sol-Gel Glasses. *J. Chem. Phys.* **1999**, *111*, 5116-5123.

(50) Loughnane, B. J.; Scodinu, A.; Fourkas, J. T. Temperature-Dependent Optical Kerr Effect Spectroscopy of Chloroform in Restricted Geometries. *Chem. Phys.* **2000**, *253*, 323-330.

(51) Zhu, X.; Farrer, R. A.; Fourkas, J. T. Ultrafast Orientational Dynamics of Nanoconfined Benzene. *J. Phys. Chem. B* **2005**, *109*, 12724-12730.

(52) Zhong, Q.; Fourkas, J. T. Shape and Electrostatic Effects in Optical Kerr Effect Spectroscopy of Aromatic Liquids. *J. Phys. Chem. B* **2008**, *112*, 15342-15348.

(53) McMorrow, D.; Lotshaw, W. T. Evidence for Low-Frequency (~15 cm^{-1}) Collective Modes in Benzene and Pyridine Liquids. *Chem. Phys. Lett.* **1993**, *201*, 369-376.

(54) Ricci, M.; Wiebel, S.; Bartolini, P.; Taschin, A.; Torre, R. Time-Resolved Optical Kerr Effect Experiments on Supercooled Benzene and Test of Mode-Coupling Theory. *Philos. Mag.* **2004**, *84*, 1491-1498.

(55) Rønne, C.; Jensby, K.; Loughnane, B. J.; Fourkas, J.; Nielsen, O. F.; Keiding, S. R. Temperature Dependence of the Dielectric Function of C_6H_6(l) and $C_6H_5CH_3$(l) Measured with THz Spectroscopy. *J. Chem. Phys.* **2000**, *113*, 3749-3756.

(56) Shirota, H.; Fujisawa, T.; Fukazawa, H.; Nishikawa, K. Ultrafast Dynamics in Aprotic Molecular Liquids: A Femtosecond Raman-Induced Kerr Effect Spectroscopic Study. *Bull. Chem. Soc. Jpn.* **2009**, *82*, 1347-1366.

(57) McMorrow, D.; Lotshaw, W. T.; Kenney-Wallace, G. A. Femtosecond Optical Kerr Studies on the Origin of the Nonlinear Responses in Simple Liquids. *IEEE J. Quantum Elect.* **1988**, *24*, 443-454.

(58) Elola, M. D.; Ladanyi, B. M. Molecular Dynamics Study of Polarizability Anisotropy Relaxation in Aromatic Liquids and Its Connection with Local Structure. *J. Phys. Chem. B* **2006**, *110*, 15525-15541.

(59) Elola, M. D.; Ladanyi, B. M.; Scodinu, A.; Loughnane, B. J.; Fourkas, J. T. Effects of Molecular Association on Polarizability Relaxation in Liquid Mixtures of Benzene and Hexafluorobenzene. *J. Phys. Chem. B* **2005**, *109*, 24085-24099.

(60) Chelli, R.; Cardini, G.; Ricci, M.; Bartolini, P.; Righini, R.; Califano, S. The Fast Dynamics of Benzene in the Liquid Phase. Part II. A Molecular Dynamics Simulation. *Phys. Chem. Chem. Phys.* **2001**, *3*, 2803-2810.

(61) Milischuk, A. A.; Ladanyi, B. M. Polarizability Anisotropy Relaxation in Nanoconfinement: Molecular Simulation Study of Acetonitrile in Silica Pores. *J. Phys. Chem. B* **2013**, *117*, 15729-15740.

(62) Gallo, P.; Ricci, M. A.; Rovere, M. Layer Analysis of the Structure of Water Confined in Vycor Glass. *J. Chem. Phys.* **2002**, *116*, 342-346.

Chapter 7: On the Empirical Analysis of Optical Kerr Effect Spectra: A Case for Constraint

7.1 *Introduction*

In 1990, McMorrow and Lotshaw presented a formalism for transforming the time-domain data of optically heterodyne detected optical Kerr effect (OHD-OKE) data into the frequency-domain, providing a means to calculate the low-frequency (0 to 500 cm^{-1}), depolarized Raman spectrum of a transparent liquid from OKE data.[1,2] Subtracting the well-characterized diffusive reorientation dynamics from the time-domain data and using this Fourier transform deconvolution procedure[1,2] yields the so-called reduced spectral density (RSD). The RSD, which is equivalent to the Bose-Einstein-corrected depolarized Raman spectrum, is typically broad and featureless. For this reason, interpretation of the underlying molecular motions proves difficult due to the overlapping nature of the polarizability contributions to the molecular response giving rise to the spectrum. Nevertheless, this formalism and the resultant low-frequency spectrum have been used to investigate the molecular dynamics of many simple[3] and complex[4] liquids.

To extract information from the RSDs of liquids, fits to empirical line shapes are often used.[5-12] The sum of the Bucaro-Litovitz (BL) function,[13]

$$f_{BL} = A_{BL}\omega^{\delta}e^{-\omega/\omega_{BL}}\,, \tag{7.1}$$

where A_{BL} is an amplitude, δ is a fitting parameter, and ω_{BL} is a characteristic frequency, and an antisymmetrized Gaussian (AG) function[14]

$$f_{AG} = A_{AG}\left[e^{-(\omega-\omega_{AG})/2\sigma_{AG}^2} - e^{-(\omega+\omega_{AG})/2\sigma_{AG}^2}\right], \quad (7.2)$$

where A_{AG} is an amplitude, and ω_{AG} is the center frequency and σ_{AG} is the width parameter of the Gaussian functions comprising the total, is used commonly to fit the RSD. The sum of these line shapes often reproduces the RSDs accurately. However, extracting a physical interpretation from the fits can be difficult and even misleading. The BL line shape was developed to fit the low-frequency Raman spectra for monatomic fluids and thus is commonly associated with interaction-induced (II) polarizability fluctuations. However, it is known that the BL function overestimates II effects in molecular liquids.[14,15] The BL function predominantly describes the low-frequency side of the RSD. The AG predominantly describes the high-frequency side of the spectrum, where molecular dynamics simulations have shown that librational dynamics dominate the spectral shape for van der Waals liquids.[16-18] Therefore, the AG function is commonly associated with the librational character of the spectrum, but there is overlap between the II, the cross-coupling between the II and purely librational dynamics, and the purely librational components on the high-frequency side of the spectrum. Fits to the OKE RSD using the BL and AG functions are not unique,[4] and the parameters extracted from them should be used cautiously in any subsequent analysis in which these values are assigned to any individual component of the spectrum.

The contributions to the OKE RSD include the collective molecular (CM) component, the II component, and the cross-coupling between the CM and II components. For a liquid composed of rigid molecules, the CM component arises solely from molecular rotation, and thus is purely librational. The II component arises from both

translational as well as rotational degrees of freedom. These two components are always positive in the time and frequency domains, whereas the cross-coupling term between them is often negative.[17-21] The BL function is always positive, and the AG function has both positive and negative components. Therefore, the three components of the fits can be compared to the three polarizability components giving rise to the RSD to gain an understanding of realistic fit parameters.

The polarizability components giving rise to the RSD are not experimentally separable. However, simulations offer the ability to separate these individual components and compare them to the BL and AG functions. Here, we present a comparison of the fitted BL and AG functions with the simulated spectrum and its individual components for benzene (i.e., a representative van der Waals liquid). The BL function is compared with the II component, whereas the positive portion of the AG function is compared with the CM contribution to the spectrum and the negative portion of the AG function compared with the cross-term between the CM and II contribution to the spectrum.

We then show fits for the experimental spectra for 1,3,5-trifluorobenzene and hexafluorobenzene, in which the fits are constrained based on the fits to the simulated spectrum of benzene. A previous study of the temperature evolution of the spectrum for 1,3,5-trifluorobenzene yielded odd results, which showed that the Gaussian frequency and width of the AG function decreased and increased, respectively, with decreasing temperature.[5] The Gaussian width for hexafluorobenzene showed behavior similar to that of the width of 1,3,5-trifluorobenzene with decreasing temperature.[5] As the temperature of a liquid decreases, the number of accessible librational states should decrease, translating into a decreased width of the AG function. As the liquid is cooled, the

intermolecular potential stiffens, which should increase librational frequency, and correspondingly, the Gaussian frequency of the AG function should increase. Therefore, the previous results were the opposite of the expected behavior.[5] Here, we show that by constraining the BL and AG fits, the expected behavior is recovered from the extracted parameters.

7.2 *Polarizability Components of the RSD*

The OKE RSD is encoded with the low-frequency, depolarized, Raman-active polarizability dynamics of a liquid. The many-body polarizability, $\mathbf{\Pi}$, of the liquid is the result of the CM component and an II component,

$$\mathbf{\Pi} = \mathbf{\Pi}^{CM} + \mathbf{\Pi}^{II} \,. \tag{7.3}$$

$\mathbf{\Pi}$ is a second-rank tensor, describing the polarizability of the liquid in Cartesian space. The CM component is the sum all the molecular polarizabilities in the liquid. The II component is the sum of all intermolecular polarizability interactions. The relevant dynamics are then encoded on the many-body polarizability time correlation function (TCF),

$$C_{xy}(t) = \langle \mathbf{\Pi}_{xy}(0)\mathbf{\Pi}_{xy}(t)\rangle \,, \tag{7.4}$$

which tracks an off-diagonal element of the polarizability tensor, and thus the decay of polarizability anisotropy in the liquid. Insertion of eq 6.3 into eq 6.4 shows that there are three components in the polarizability TCF: the CM, the II, and the cross-correlation (CMII)

$$C_{xy}^{CM}(t) = \langle \mathbf{\Pi}_{xy}^{CM}(0)\mathbf{\Pi}_{xy}^{CM}(t)\rangle \tag{7.5}$$

$$C_{xy}^{II}(t) = \langle \mathbf{\Pi}_{xy}^{II}(0)\mathbf{\Pi}_{xy}^{II}(t)\rangle \tag{7.6}$$

$$C_{xy}^{CMII}(t) = \langle \mathbf{\Pi}_{xy}^{CMII}(0)\mathbf{\Pi}_{xy}^{CMII}(t) + \mathbf{\Pi}_{xy}^{IICM}(0)\mathbf{\Pi}_{xy}^{IICM}(t)\rangle \, . \tag{7.7}$$

For liquids composed of rigid molecules, $C_{xy}^{CM}(t)$ contains only dynamics that depend on reorientation of the principle symmetry axis of the molecule. $C_{xy}^{CM}(t)$ is therefore, dominated by orientational diffusion and librational dynamics. $C_{xy}^{II}(t)$ contains translational dynamics as well as reorientation, and $C_{xy}^{CMII}(t)$ describes the coupling between interaction-induced and molecular polarizability dynamics.

The RSD is then calculated through transformation of the nuclear response function, $R(t)$,

$$R(t) \propto -\frac{d}{dt} C_{xy}(t) \, . \tag{7.8}$$

The RSD can be calculated by removing orientational diffusion from $R(t)$ and taking the Fourier transform of the resultant function. Orientational diffusion is removed by assuming an exponential functional form and subtracting this function from $R(t)$. The RSD, $I(\omega)$, is defined as the imaginary component of the Fourier transformation of this resultant function

$$I(\omega) = \int_0^\infty \left[R(t) - \left(e^{-t/\tau_c}\left(1 - e^{-t/\tau_{rise}}\right)\right)\right] \sin(\omega t)\, dt \, . \tag{7.9}$$

Here, τ_c is the collective orientational diffusion decay time constant and τ_{rise} is the assumed rise time of these dynamics, which is usually on the order of 200 fs. $I(\omega)$ can be calculated for each of the polarizability components corresponding to eqs 7.5, 7.6, and 7.7.

7.3 *Results and Discussion*

7.3.1 *Simulated Spectra*

The simulated spectra are taken from Chapter 4. Figure 7.1 shows the simulated RSD for benzene at 293 K. Three equivalent fits to the RSD using the BL and AG functions are also shown. These fits demonstrate that constraining the amplitude of the AG function does not substantially change the shape or the amplitude of the resultant fit. Inspection of the individual BL and AG functions comprising the total fit can point us toward a sensible protocol for fitting the OKE RSD and to obtain realistic parameter values for subsequent analysis.

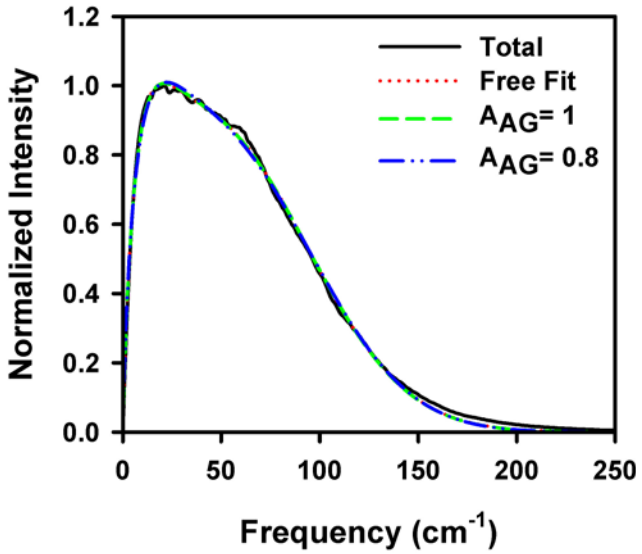

Figure 7.1 Fits of BL and AG functions to the simulated spectrum for benzene (black line), including the free fit (red dots) and constrained fits for A_{AG} = 1 (green dashes) and A_{AG} = 0.8 (blue dot dashes).

Figure 7.2 shows the comparisons between the BL and AG functions from the fits in Figure 7.1 and the individual polarizability components of the simulated RSD for benzene. In Figure 7.2A, the BL function, which was developed to fit II spectra for

monatomic fluids, is compared with the II component of the RSD. Even though the BL function and the II component of the spectrum have similar shapes, the BL function greatly overestimates the amplitude of II components represented in the spectrum. The BL function shows little change with changes in the constraint of the amplitude of the AG function, suggesting that the fitted BL function is unique.

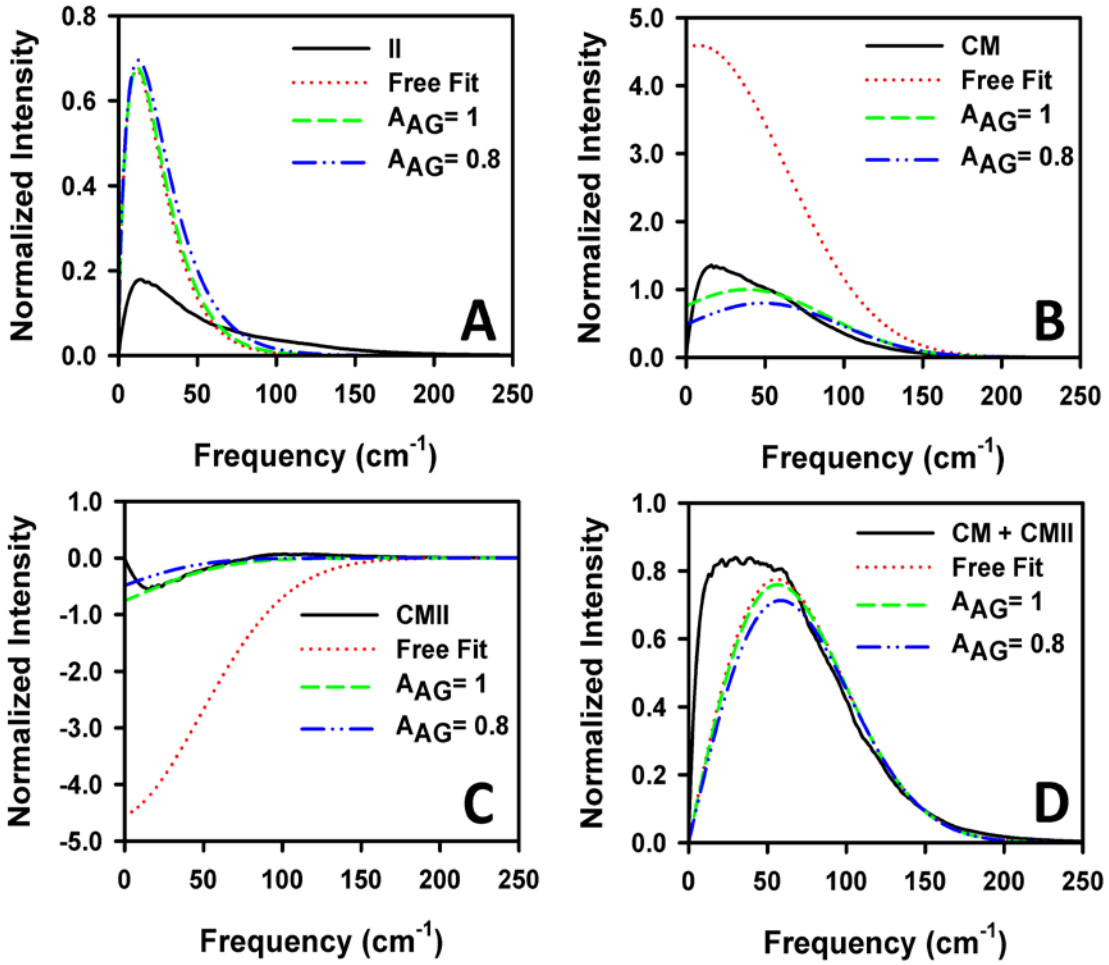

Figure 7.2 Comparisons of the (A) interaction-induced component of the RSD with the BL function, (B) the collective molecular component of the RSD with the positive component of the AG function, (C) the cross term between the interaction-induced and collective molecular components of the RSD with the negative component of the AG function, and (D) the sum of the cross term and the collective molecular components of the RSD with the total AG function.

Figure 7.2B is a comparison of the positive component of the AG function with the CM component of the RSD. The free-fit amplitude of the AG function is quite large

compared to the amplitude of the CM spectrum. This result shows that the amplitude of the AG function can become unrealistic when the fit is not constrained in a physically realistic manner. When the amplitude of the AG function is constrained, the positive component of this function mimics the CM spectrum more closely, especially at high frequencies.

The cross term between II scattering and CM scattering is negative, and it is natural to compare the negative component of the AG function with this cross term (Figure 7.2C). It is again clear from this comparison that the unconstrained fit gives amplitude that is much too large. With a physically realistic constraint of the amplitude of the AG function, the negative component of the AG function again becomes comparable to the CMII spectrum. The CMII spectrum exhibits a peak with negative amplitude at ~22 cm^{-1}. This peak plays a significant role in the shape of the total spectrum by flattening its low-frequency side.

Table 7.1 Fit parameters for simulated benzene spectrum and several values of A_{AG}. The uncertainty in A_{BL}, δ, and ω_{BL} is approximately 5%. Uncertainty in ω_{AG} and σ_{AG} is approximately 2%.

A_{BL}	δ	ω_{BL} (cm^{-1})	A_{AG}	ω_{AG} (cm^{-1})	σ_{AG} (cm^{-1})
0.21	0.78	16.2	0.80	48.74	48.73
0.19	0.84	14.1	1.00	38.39	51.22
0.19	0.87	13.4	1.50	24.55	53.98
0.19	0.88	13.3	2.00	18.15	54.83
0.19	0.88	13.3	3.00	11.98	55.39
0.19	0.88	13.3	4.59	7.79	55.64

Figures 7.2B and 7.2C also show that as the amplitude of the AG function is constrained to smaller values, ω_{AG} shifts to higher frequency and σ_{AG} decreases. The fit parameters to the simulated spectrum for several values of A_{AG} (Table 7.1) show that ω_{AG}

shifts over a much wider range of values than does σ_{AG} for the same range of A_{AG} constraints.

Figure 7.2D shows the sum of the CM and CMII spectra, as well as the total AG function. Even though the amplitude of the AG function is constrained to three different values for the fits, the shape and position of the total function is largely unaffected. This result shows the total function is nearly constant even though the parameter values taken from the fits can vary. The comparison of the calculated spectrum with the AG function shows that the AG function accurately captures the high-frequency side of the spectrum. However, the inability of the AG function to reproduce the low-frequency side of this spectrum is the reason that the BL function overestimates the II scattering amplitude in the total RSD.

The true amplitude of the AG function is modulated both by the amplitude given in eq 7.2 and by the difference of the Gaussian functions comprising the total AG function. These competing effects lead to fit parameters that, in the absence of another constraint, are not unique. It is therefore reasonable to suggest that the amplitude given in eq 7.2 should be constrained to in a physically realistic manner to reduce the number of variables in the total fit and to extract realistic values for the Gaussian peak frequency and width.

7.3.2 *Experimental Spectra*

Figure 7.3 shows the experimental spectrum for 1,3,5-trifluorobenzene at 294 K (from ref. 5) and the individual components of unconstrained and constrained fits to the sum of the BL and AG functions. Figure 7.3A shows the total fits to the spectrum. The total fit is nearly unchanged for three different values of A_{AG}. Figure 7.3B shows the

spectrum along with the BL functions resulting from the three fits. Again, the BL function is relatively unaffected by the constraints on the amplitude of the AG function. Figure 7.3C shows the RSD and the positive and negative components of the AG function. When the fit is unconstrained, the amplitude of these components is unrealistically large. Furthermore, the center frequency of the Gaussian functions is unrealistically low (2.70 cm^{-1}). This function is commonly used to describe librational dynamics, which dominate the high-frequency side of the RSD in van der Waals liquids. As the amplitude is constrained to smaller values, the Gaussian center frequency shifts toward higher values and the actual position of the AG peak.

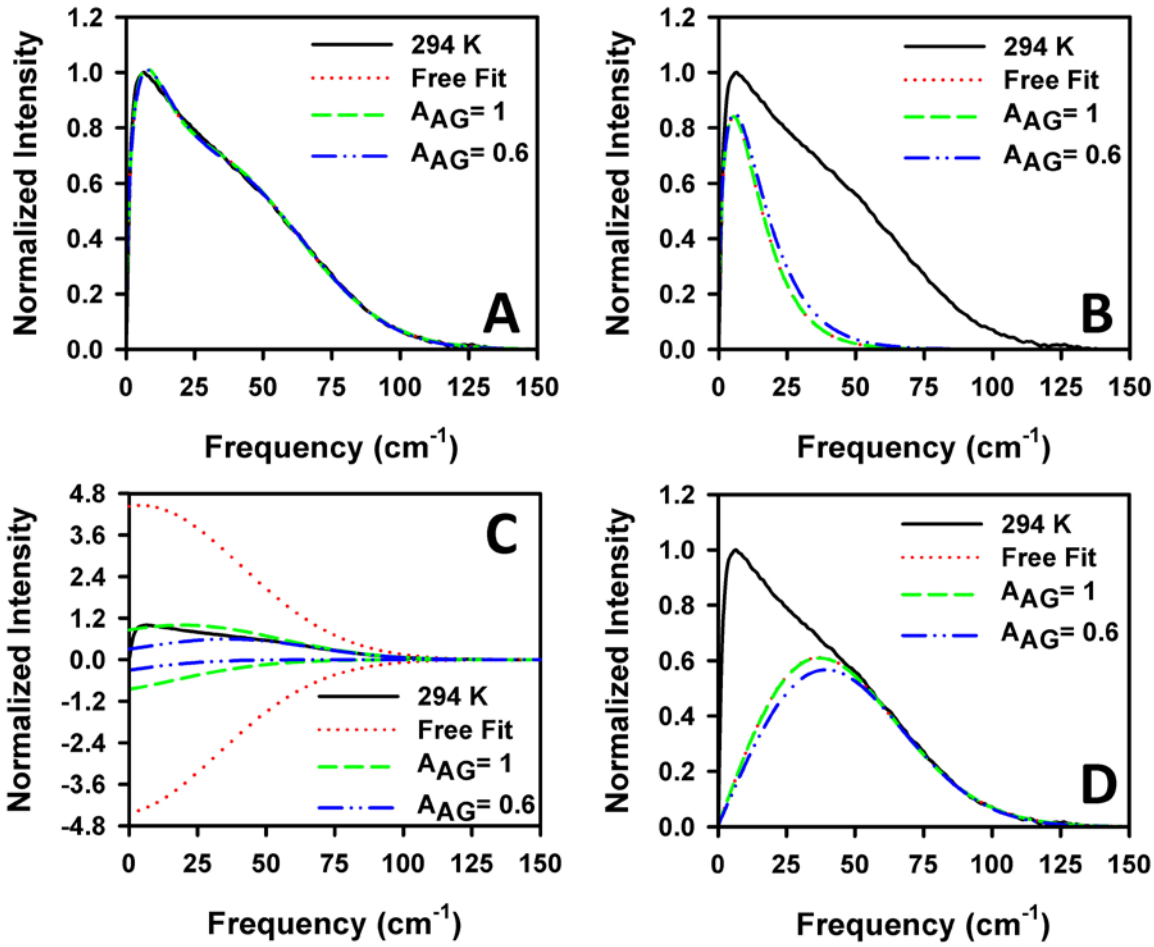

Figure 7.3 Comparison of (A) total fits, (B) the BL functions, (C) the positive and negative components of the AG function, and (D) the total AG function with the experimental spectrum for 1,3,5-trifluorobenzene (black line). The free fit functions are red dotted lines. The constrained fit functions are represented by green dashed lines and blue dash-dot lines for A_{AG} = 1 and A_{AG} = 0.6, respectively.

Figure 7.3D shows the spectrum and the total AG function. The shapes of the total AG functions are nearly independent of the value of the amplitude. The height of the total AG function is approximately 0.6. Additionally, the difference between the center frequency of the Gaussian functions comprising the total AG function and the peak position of the total AG function decreases as the amplitude of the AG function is constrained to smaller values. Therefore, the fit parameters give a more realistic description of the total AG function when the fits are constrained.

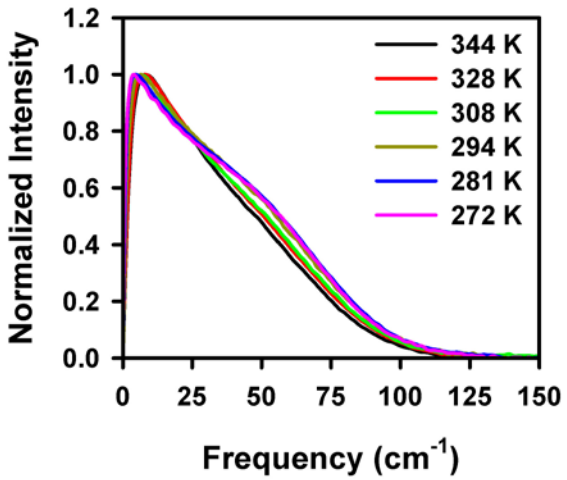

Figure 7.4 Experimental spectra of 1,3,5-trifluorobenzene over a wide range of temperatures.

Constraining the amplitude of the AG function can potentially affect the perceived evolution of the RSDs of liquids with variables such as temperature and pressure. Figure 7.4 shows the RSDs for 1,3,5-trifluorobenzene over a wide range of temperatures. The high-frequency side of the RSD shifts to higher frequency with decreasing temperature. This shift is due to the increase in librational frequencies within the liquid as the molecular potential stiffens with increasing density.[15] In the study conducted by Loughnane *et al.*, unconstrained fits to these data showed a trend in which

ω_{AG} shifts to lower frequency with decreasing temperature, which is the opposite of the apparent behavior.[5]

Figure 7.5 shows the fits to the data for three values of the amplitude of the AG function. The trend shown in the shift of ω_{AG} is reversed as A_{AG} is constrained to be a smaller value. Additionally, the thermal evolution of σ_{AG} is reversed, although σ_{AG} is affected to a lesser extent. As the temperature of the liquid increases, the molecules can access the more anharmonic portion of the molecular potential, resulting in a greater number of librational states in the liquid. Therefore, the width of the function associated with libration would be expected increase. It is important to note that the expected behavior for these parameters is given by the constrained fits. Furthermore, the correlation of ω_{AG} with temperature increases when the amplitude of the AG function is constrained to physically realistic values. The fit parameters are given in Tables 7.2, 7.3 and 7.4.

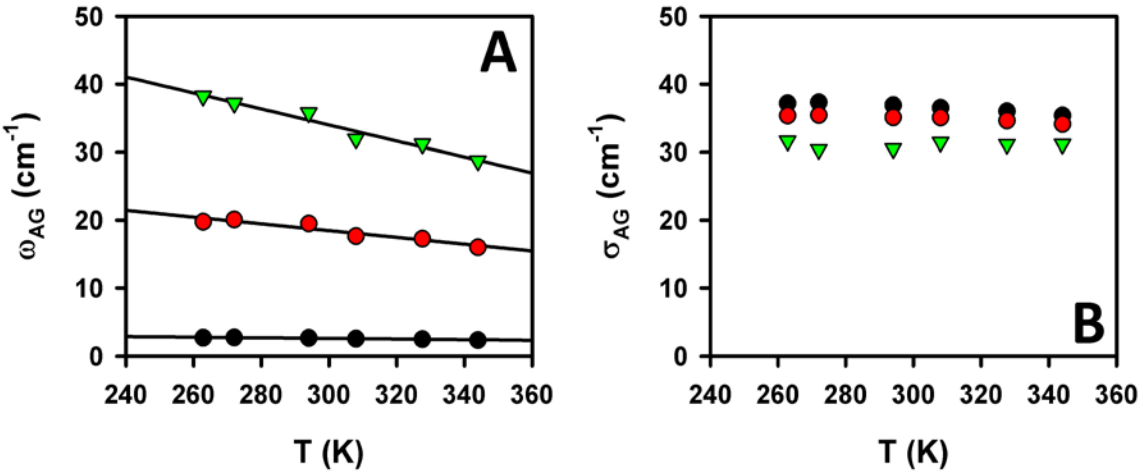

Figure 7.5 Plots of (A) $\boldsymbol{\omega_{AG}}$ and (B) $\boldsymbol{\sigma_{AG}}$ as a function of temperature for 1,3,5-trifluorobenzene. The parameters of the free fits are represented by black circles. Constrained fits for A_{AG} = 1 and A_{AG} = 0.6 are represented by red circles and green triangles, respectively. The black lines are linear regressions of the data.

Table 7.2 Fit parameters for 1,3,5-trifluoroboenzene spectrum. A_{AG} = 0.6. Uncertainty in A_{BL}, δ, and ω_{BL} is approximately 5%. Uncertainty in ω_{AG} and σ_{AG} is approximately 2%.

T (K)	A_{BL}	δ	ω_{BL} (cm^{-1})	A_{AG}	ω_{AG} (cm^{-1})	σ_{AG} (cm^{-1})
263	0.73	0.38	11.7	0.6	38.22	31.62
272	0.68	0.45	10.8	0.6	37.18	30.37
294	0.54	0.59	10.0	0.6	35.76	30.51
308	0.56	0.57	10.0	0.6	31.92	31.44
328	0.43	0.73	9.2	0.6	31.19	31.14
344	0.39	0.79	8.9	0.6	28.70	31.15

Table 7.3 Fit parameters for 1,3,5-trifluoroboenzene spectrum. A_{AG} = 1. Uncertainty in A_{BL}, δ, and ω_{BL} is approximately 5%. Uncertainty in ω_{AG} and σ_{AG} is approximately 2%.

T (K)	A_{BL}	δ	ω_{BL} (cm^{-1})	A_{AG}	ω_{AG} (cm^{-1})	σ_{AG} (cm^{-1})
263	0.74	0.42	9.7	1	19.76	35.37
272	0.67	0.50	9.1	1	20.12	35.45
294	0.53	0.64	8.7	1	19.50	35.12
308	0.56	0.60	9.2	1	17.65	35.08
328	0.42	0.76	8.6	1	17.28	34.63
344	0.39	0.80	8.6	1	16.02	34.14

Table 7.4 Fit parameters for 1,3,5-trifluoroboenzene spectrum. A_{AG} is unconstrained. Uncertainty in A_{BL}, δ, and ω_{BL} is approximately 5%. Uncertainty in ω_{AG} and σ_{AG} is approximately 2%.

T (K)	A_{BL}	δ	ω_{BL} (cm^{-1})	A_{AG}	ω_{AG} (cm^{-1})	σ_{AG} (cm^{-1})
263	0.74	0.42	9.6	6.90	2.73	37.19
272	0.67	0.50	9.1	6.92	2.77	37.32
294	0.53	0.64	8.7	6.90	2.70	36.89
308	0.56	0.60	9.2	6.58	2.58	36.53
328	0.42	0.76	8.6	6.57	2.53	36.03
344	0.39	0.81	8.5	6.51	2.38	35.36

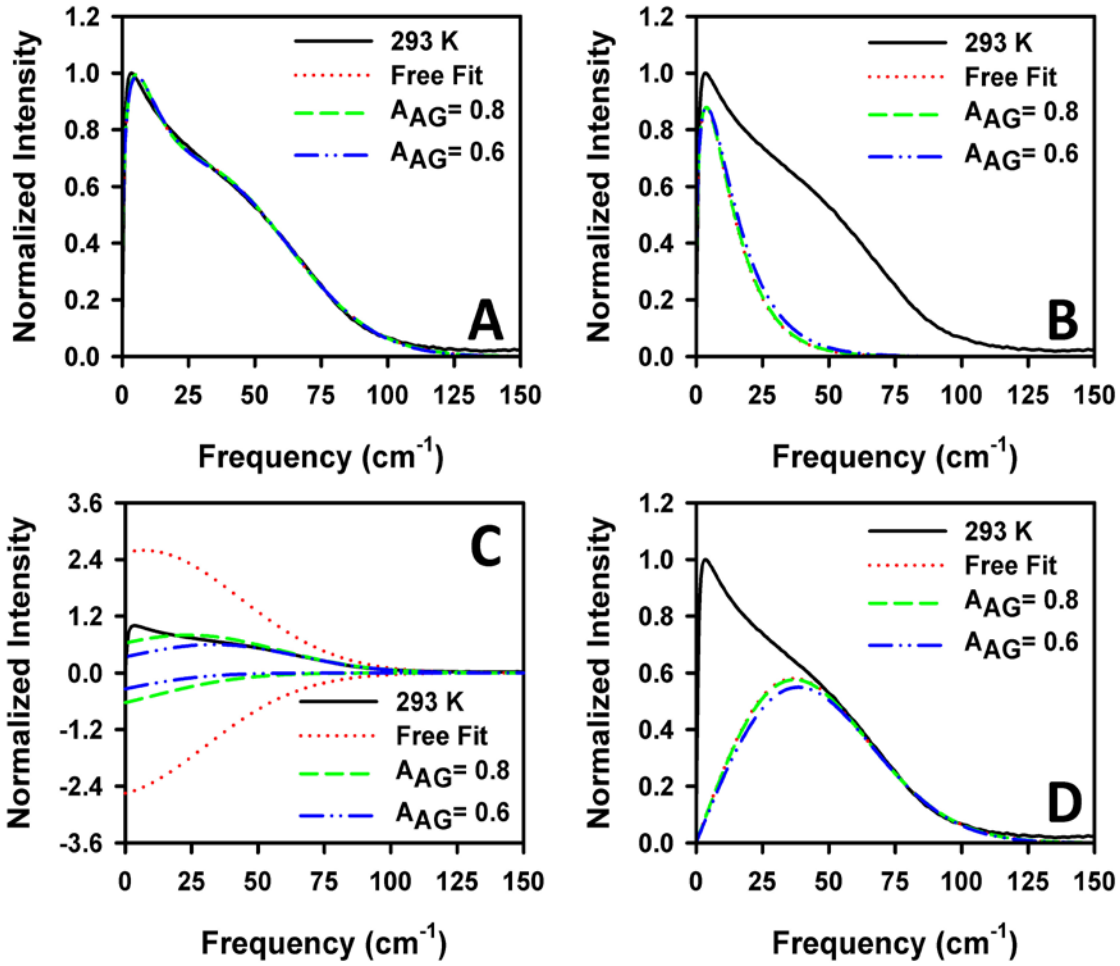

Figure 7.6 Comparison of (A) total fits, (B) the BL functions, (C) the positive and negative components of the AG function, and (D) the total AG function with the experimental spectrum for hexafluorobenzene (black line). The free fit functions are red dotted lines. The constrained fit functions are represented by green dashed lines and blue dash-dot lines for A_{AG} = 0.8 and A_{AG} = 0.6, respectively.

The same analysis can be repeated for hexafluorobenzene. These data are also taken from ref 5. Figure 7.6 shows the comparison between the spectrum for hexafluorobenzene at 293 K and the BL and AG function for three values of A_{AG}. Figure 7.6A shows the spectrum and three fits, all of which are nearly identical. Figure 7.6B shows that the shape of the BL function is nearly unaffected by constraining the amplitude of the AG function. Figure 7.6C shows the positive and negative components of the AG function corresponding to the fits in Figure 7.6A. Again, the free fit amplitude of the AG function is unrealistically large. Figure 7.6D shows that for three different

values of A_{AG}, the total AG functions are nearly constant. These results again demonstrate that although the values extracted from the fits to the spectrum using the BL and AG functions are not mathematically unique, the resultant forms of the functions are nearly identical.

Figure 7.7 shows the spectra for hexafluorobenzene over a wide range of temperatures. The high-frequency edge of the spectrum shifts to higher frequencies with decreasing temperature. However, Loughnane *et al.* showed that ω_{AG} extracted from free fits was nearly constant with respect to temperature.[5] Furthermore, σ_{AG} decreased for these fits with increasing temperature, which is the opposite of the apparent and expected behavior, as the width of the function should increase as the anharmonic portion of the potential well becomes more thermally accessible.

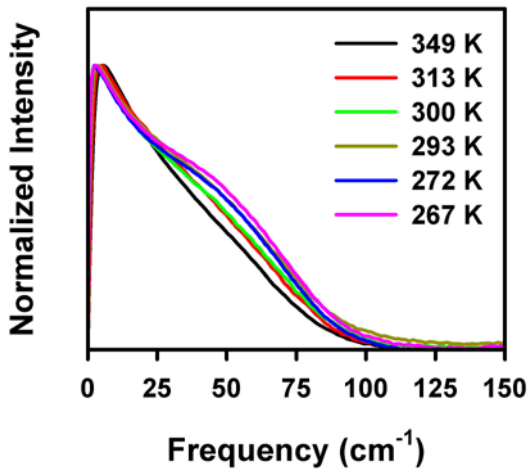

Figure 7.7 Experimental spectra of hexafluorobenzene over a wide range of temperatures.

Figure 7.8 shows the plots of ω_{AG} and σ_{AG} as a function of temperature for hexafluorobenzene for three different values of A_{AG}. Figure 7.8A shows that as A_{AG} is constrained toward values near the actual height (A_{AG} = 0.6; See Figure 7.6D) of the total

AG function, the correlation of ω_{AG} with temperature increases and the shift to lower frequency with increasing temperature becomes more pronounced. This behavior is the result of decreasing the difference between the Gaussian center frequency and the actual peak position of the AG function. Figure 7.8B shows the plots of σ_{AG} as a function of temperature for three values of A_{AG}. This parameter is less affected by constraining the amplitude of the AG function. However, the behavior of the parameter with respect to temperature reverses as the A_{AG} is increasingly constrained. Again, the behavior of this parameter conforms to expectation when A_{AG} is constrained to a reasonable value. The fit parameters are given in Tables 7.5, 7.6, and 7.7.

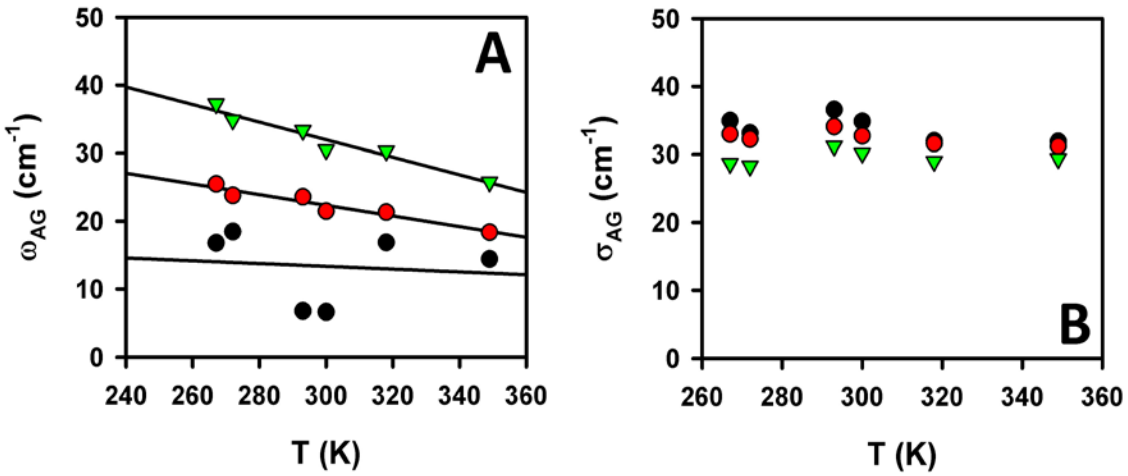

Figure 7.8 Plots of (A) $\boldsymbol{\omega_{AG}}$ and (B) $\boldsymbol{\sigma_{AG}}$ as a function of temperature for hexafluorobenzene. The parameters of the free fits are represented by black circles. Constrained fits for A_{AG} = 0.8 and A_{AG} = 0.6 are represented by red circles and green triangles, respectively. The black lines are linear regressions of the data.

Table 7.5 Fit parameters for hexafluorobenzene spectrum. A_{AG} = 0.6. Uncertainty in A_{BL}, δ, and ω_{BL} is approximately 5%. Uncertainty in ω_{AG} and σ_{AG} is approximately 2%.

T	A_{BL}	δ	ω_{BL} (cm^{-1})	A_{AG}	ω_{AG} (cm^{-1})	σ_{AG} (cm^{-1})
267	0.85	0.30	11.0	0.6	37.24	28.65
272	0.85	0.32	10.2	0.6	34.87	28.27
293	0.76	0.37	10.8	0.6	33.33	31.23
300	0.75	0.41	9.6	0.6	30.49	30.14
318	0.63	0.55	8.8	0.6	30.32	28.97
349	0.54	0.67	8.1	0.6	25.74	29.36

Table 7.6 Fit parameters for hexafluorobenzene spectrum. A_{AG} = 0.8. Uncertainty in A_{BL}, δ, and ω_{BL} is approximately 5%. Uncertainty in ω_{AG} and σ_{AG} is approximately 2%.

T	A_{BL}	δ	ω_{BL} (cm^{-1})	A_{AG}	ω_{AG} (cm^{-1})	σ_{AG} (cm^{-1})
267	0.86	0.34	9.4	0.8	25.49	32.99
272	0.86	0.34	9.1	0.8	23.79	32.26
293	0.76	0.40	9.7	0.8	23.60	34.09
300	0.75	0.43	9.0	0.8	21.50	32.73
318	0.62	0.58	8.2	0.8	21.33	31.61
349	0.54	0.68	7.9	0.8	18.39	31.21

Table 7.7 Fit parameters for hexafluorobenzene spectrum. A_{AG} is unconstrained. Uncertainty in A_{BL}, δ, and ω_{BL} is approximately 5%. Uncertainty in ω_{AG} and σ_{AG} is approximately 2%.

T	A_{BL}	δ	ω_{BL} (cm^{-1})	A_{AG}	ω_{AG} (cm^{-1})	σ_{AG} (cm^{-1})
267	0.86	0.34	9.2	1.15	16.80	34.94
272	0.86	0.35	8.8	1.00	18.48	33.13
293	0.76	0.40	9.6	2.59	6.83	36.58
300	0.75	0.44	8.9	2.44	6.66	34.87
318	0.62	0.61	7.6	1.00	16.89	31.97
349	0.54	0.68	7.8	1.00	14.42	31.89

The implications in the constraint of the amplitude of the AG function can be significant. In their analysis of the experimental spectra presented here, Loughnane *et al.* proposed a model based on the local structure of the liquids to account for the different

shapes of the OKE RSDs for benzene, hexafluorobenzene , and 1,3,5-trifluorobenzene.[5] The basis for this model was that the disparate behavior of the parameters corresponding to the AG function for benzene and hexafluorobenzene/1,3,5,-trifluorobenzene. Given that the three molecules have the same disk-like shape and nearly the same hydrodynamic volume, it was natural to assume that the differing local structures of each liquid may account for the difference in the extracted fit parameters for the temperature dependent spectra. By constraining the amplitude of the AG function, the fit parameters more accurately represent the apparent peak position and width. The temperature evolution of the extracted fit parameters is consistent across the three molecules when A_{AG} is constrained to values to near the height of the total AG function, invalidating the proposed model.

If one chooses to use the BL and AG functions to fit OKE RSDs, these results suggest that the amplitude of the AG function should be constrained to extract values for subsequent analysis. An initial fit should be performed to determine the actual height of the AG function, and a subsequent fit should be performed in which the amplitude of the AG function is constrained to a value near this height. This process ensures that ω_{AG} is close to the value for the peak position of the total AG function, for which there is no analytical form. Correspondingly, by constraining the amplitude of the AG function, σ_{AG} is more representative of the actual width.

7.4 *Conclusions*

We have presented a study in which the Bucaro-Litovitz[13] and antisymmetrized Gaussian[14] functions are compared to the individual polarizability components for the

simulated OKE RSD of benzene. These comparisons suggest that the amplitude of the antisymmetrized Gaussian function should be constrained to a value equal to or less than the height of the total spectrum. By constraining the amplitude of the function, the positive and negative components of the antisymmetrized Gaussian function resemble the librational and cross-correlation components of the polarizability contributions to the total spectrum, respectively. We have also shown that by constraining the amplitude of the antisymmetrized Gaussian function, the thermodynamic evolution of the spectrum for 1,3,5-trifluorobenzene and hexafluorobenzene is accurately captured. These results suggest that by constraining the amplitude of the antisymmetrized Gaussian function when used to fit OKE RSDs, the extracted parameters will be consistent with the actual spectral behavior on the high-frequency side of the spectrum.

7.5 *References*

(1) McMorrow, D.; Lotshaw, W. T. The Frequency Response of Condensed-Phase Media to Femtosecond Optical Pulses: Spectral-Filter Effects. *Chem. Phys. Lett.* **1990**, *174*, 85-94.

(2) McMorrow, D.; Lotshaw, W. T. Intermolecular Dynamics in Acetonitrile Probed with Femtosecond Fourier-Transform Raman-Spectroscopy. *J. Phys. Chem.* **1991**, *95*, 10395-10406.

(3) Zhong, Q.; Fourkas, J. T. Optical Kerr Effect Spectroscopy of Simple Liquids. *J. Phys. Chem. B* **2008**, *112*, 15529-15539.

(4) Hunt, N. T.; Jaye, A. A.; Meech, S. R. Ultrafast Dynamics in Complex Fluids Observed Through the Ultrafast Optically-Heterodyne-Detected Optical-Kerr-Effect (OHD-OKE). *Phys. Chem. Chem. Phys.* **2007**, *9*, 2167-2180.

(5) Loughnane, B. J.; Scodinu, A.; Fourkas, J. T. Temperature-Dependent Optical Kerr Effect Spectroscopy of Aromatic Liquids. *J. Phys. Chem. B* **2006**, *110*, 5708-5720.

(6) Ricci, M.; Bartolini, P.; Chelli, R.; Cardini, G.; Califano, S.; Righini, R. The Fast Dynamics of Benzene in the Liquid Phase - Part I. Optical Kerr Effect Experimental Investigation. *Phys. Chem. Chem. Phys.* **2001**, *3*, 2795-2802.

(7) Shirota, H.; Fujisawa, T.; Fukazawa, H.; Nishikawa, K. Ultrafast Dynamics in Aprotic Molecular Liquids: A Femtosecond Raman-Induced Kerr Effect Spectroscopic Study. *Bull. Chem. Soc. Jpn.* **2009**, *82*, 1347-1366.

(8) Neelakandan, M.; Pant, D.; Quitevis, E. L. Reorientational and Intermolecular Dynamics in Binary Liquid Mixtures of Hexafluorobenzene and Benzene: Femtosecond Optical Kerr Effect Measurements. *Chem. Phys. Lett.* **1997**, *265*, 283-292.

(9) Heisler, I. A.; Meech, S. R. Low-Frequency Isotropic and Anisotropic Raman Spectra of Aromatic Liquids. *J. Chem. Phys.* **2010**, *132*, 174503.

(10) Smith, N. A.; Lin, S. J.; Meech, S. R.; Shirota, H.; Yoshihara, K. Ultrafast Dynamics of Liquid Anilines Studied by the Optical Kerr Effect. *J. Phys. Chem. A* **1997**, *101*, 9578-9586.

(11) Manfred, K.; He, X. X.; Fourkas, J. T. Assessing the Role of Moment of Inertia in Optical Kerr Effect Spectroscopy. *J. Phys. Chem. B* **2010**, *114*, 12096-12103.

(12) Xiao, D.; Rajian, J. R.; Cady, A.; Li, S.; Bartsch, R. A.; Quitevis, E. L. Nanostructural Organization and Anion Effects on the Temperature Dependence of the Optical Kerr Effect Spectra of Ionic Liquids. *J. Phys. Chem. B* **2007**, *111*, 4669-4677.

(13) Bucaro, J. A.; Litovitz, T. A. Rayleigh Scattering: Collisional Motions in Liquids. *J. Chem. Phys.* **1971**, *54*, 3846-3853.

(14) Chang, Y. J.; Castner, E. W. Intermolecular dynamics of substituted benzene and cyclohexane liquids, studied by femtosecond nonlinear-optical polarization spectroscopy. *J. Phys. Chem.* **1996**, *100*, 3330-3343.

(15) Bender, J. S.; Cohen, S. R.; He, X.; Fourkas, J. T.; Coasne, B. Toward *in Situ* Measurement of the Density of Liquid Benzene Using Optical Kerr Effect Spectroscopy. *J. Phys. Chem. B* **2016**, *120*, 9103-9114.

(16) Ryu, S.; Stratt, R. M. A Case Study in the Molecular Interpretation of Optical Kerr Effect Spectra: Instantaneous-Normal-Mode Analysis of the OKE Spectrum of Liquid Benzene. *J. Phys. Chem. B* **2004**, *108*, 6782-6795.

(17) Bender, J. S.; Coasne, B.; Fourkas, J. T. Assessing Polarizability Models for the Simulation of Low-Frequency Raman Spectra of Benzene. *J. Phys. Chem. B* **2015**, *119*, 9345-9358.

(18) Elola, M. D.; Ladanyi, B. M. Polarizability Response in Polar Solvents: Molecular-Dynamics Simulations of Acetonitrile and Chloroform. *J. Chem. Phys.* **2005**, *122*, 224506.

(19) Elola, M. D.; Ladanyi, B. M.; Scodinu, A.; Loughnane, B. J.; Fourkas, J. T. Effects of Molecular Association on Polarizability Relaxation in Liquid Mixtures of Benzene and Hexafluorobenzene. *J. Phys. Chem. B* **2005**, *109*, 24085-24099.

(20) Paolantoni, M.; Ladanyi, B. M. Polarizability Anisotropy Relaxation in Liquid Ethanol: A Molecular Dynamics Study. *J. Chem. Phys.* **2002**, *117*, 3856-3873.

(21) Elola, M. D.; Ladanyi, B. M. Molecular Dynamics Study of Polarizability Anisotropy Relaxation in Aromatic Liquids and Its Connection with Local Structure. *J. Phys. Chem. B* **2006**, *110*, 15525-15541.

Chapter 8: Conclusions

8.1 *Conclusions and Future Work*

Liquid dynamics have been studied using OHD-OKE spectroscopy for decades, and much work has been done to elucidate the microscopic information encoded in the OKE RSD.[1,2] MD simulations have been a valuable tool to explore the individual polarizability components of the RSD and to simulate the RSD as a function of thermodynamic variables. The work contained in this thesis makes use of both OKE spectroscopy and MD simulations to explore the possibility of using this technique to measure the density of liquids.

The accuracy of the simulated OKE RSD depends on the model of the molecular polarizability used in the calculations. Several models of the polarizability of benzene have been studied here.[3] We have shown that the polarizability should be distributed across the molecular geometry to calculate an accurate RSD. A point anisotropic molecular polarizability model overestimates the II components of the RSD because three-body effects are minimized. Many-body effects are more faithfully captured with a distributed polarizability model, resulting in a more accurate total RSD.

The RSD of a liquid is dependent on temperature and density. Using benzene as a representative system, we have shown that density affects the high-frequency components of the RSD to a greater extent than does temperature.[4] We have also shown that the effects of temperature and density are separable in the parameters of the empirical fits to the RSD. These results suggest that OKE spectroscopy can be used to measure the density of a liquid in a variety of thermodynamic states. The local structure

of the simulated liquid also shows behavior corresponding to that of the RSD. This result suggests that the RSD does depend on local structure of the liquid.

The density of confined benzene has been investigated using OKE spectroscopy. The librational dynamics of the confined liquid are consistent with densification. The density is estimated to increase by ~1.5% for benzene confined in the smallest pores studied. This increase corresponds to a 14 K decrease in temperature for the bulk liquid at atmospheric pressure. MD simulations support this conclusion. The vibrational density of states for molecular tumbling shows behavior consistent with densification and is in qualitative agreement with the experimental data. The "bulk-like" molecules in the centers of the pores exhibit spectral behavior in agreement with the experimental RSDs, showing that the polarizability interactions at the surface of the pores are unlikely to be the cause of the shift of the high-frequency components of the RSD with increasing confinement.

Empirical fits are often used to extract information from the RSDs of liquids. By comparing the Bucaro-Litovitz[5] and antisymmetrized Gaussian[6] functions with the polarizability components of the simulated RSD for benzene, a scheme is proposed to ensure the extraction of physically realistic parameters. The amplitude of the antisymmetrized Gaussian function is constrained to a physically realistic value. This scheme is used to reexamine the experimental spectra for 1,3,5-trifluorobenzene and hexafluorobenzene. A previous temperature-dependent study of these liquids showed anomalous behavior based on the fits to these two functions. By constraining the amplitude of the antisymmetrized Gaussian function, the expected behavior is extracted

from the experimental spectra, demonstrating the efficacy of the proposed analysis scheme.

There are several directions in which the research presented in this thesis can be taken in the future. The research in Chapters 4, 5, 6, and 7 can be extended to other liquids to test the generality of the results presented.

Several models of the molecular polarizability for liquids other than benzene may be investigated in connection with the accurate calculation of the simulated OKE RSD. It is likely that distributed models of the molecular polarizability will capture the polarizability dynamics of a liquid more accurately, but more research is needed to determine the degree of distribution needed to calculate an accurate RSD.

MD simulations of the OKE RSD as a function of temperature and density should be conducted for several liquids to test the generality of the separability of these thermodynamic variables in OKE spectra. For van der Waals liquids, the results presented here should be general because the high-frequency components of the RSD are dominated by libration. In addition to MD simulations, high-pressure experiments should be conducted to test the density dependence of the RSD. If the results presented in this thesis hold, the width of the antisymmetrized Gaussian function should remain constant at varying densities.

The density of liquids other than benzene should also be investigated using OKE spectroscopy. The high-frequency components of the RSD of acetonitrile and pyridine shift to the blue upon confinement in silica nanopores, suggesting densification of the liquids.[7] Temperature-dependent studies of these confined liquids may also be performed

to investigate the effects of confinement on the glass transition temperature. The density of the confined liquid will show a sudden and pronounced change at the glass transition temperature. Therefore, the characteristic frequency of the antisymmetrized Gaussian function should exhibit a pronounced change at this temperature. By performing these temperature-dependent studies on confined liquids, the glass transition temperature can be determined as a function of average pore size.

8.2 *References*

(1) Zhong, Q.; Fourkas, J. T. Optical Kerr Effect Spectroscopy of Simple Liquids. *J. Phys. Chem. B* **2008**, *112*, 15529-15539.

(2) Hunt, N. T.; Jaye, A. A.; Meech, S. R. Ultrafast Dynamics in Complex Fluids Observed Through the Ultrafast Optically-Heterodyne-Detected Optical-Kerr-Effect (OHD-OKE). *Phys. Chem. Chem. Phys.* **2007**, *9*, 2167-2180.

(3) Bender, J. S.; Coasne, B.; Fourkas, J. T. Assessing Polarizability Models for the Simulation of Low-Frequency Raman Spectra of Benzene. *J. Phys. Chem. B* **2015**, *119*, 9345-9358.

(4) Bender, J. S.; Cohen, S. R.; He, X.; Fourkas, J. T.; Coasne, B. Toward in Situ Measurement of the Density of Liquid Benzene Using Optical Kerr Effect Spectroscopy. *J. Phys. Chem. B* **2016**, *120*, 9103-9114.

(5) Bucaro, J. A.; Litovitz, T. A. Rayleigh Scattering: Collisional Motions in Liquids. *J. Chem. Phys.* **1971**, *54*, 3846-3853.

(6) Chang, Y. J.; Castner, E. W. Intermolecular Dynamics of Substituted Benzene and Cyclohexane Liquids, Studied by Femtosecond Nonlinear-Optical Polarization Spectroscopy. *J. Phys. Chem.* **1996**, *100*, 3330-3343.

(7) He, X. Studying Liquid Dynamics with Optical Kerr Effect Spectroscopy University of Maryland, 2015.

Appendix A: LabVIEW Program for Simulated OKE Data Analysis

This program was written in LabVIEW to perform the Fourier analysis of the many-body polarizability time correlation functions (TCFs) for simulated optical Kerr effect RSDs. There are two files needed to load the program: a short-time step file and a long-time step file. If there is only one type of file, the user must load that file twice. The file must have two columns: one for the time array and one for the TCF intensity array. The input files must be .txt files. The following is a step-by-step guide to using the software. This program follows the theory given in Chapter 2, Section 2.1, Subsection 2.1.2.

I. Input files

   i. Run software and click folder icons to load files.

   ii. Choose files for each type.

   iii. Click “Start Analysis” when the files are inputted.

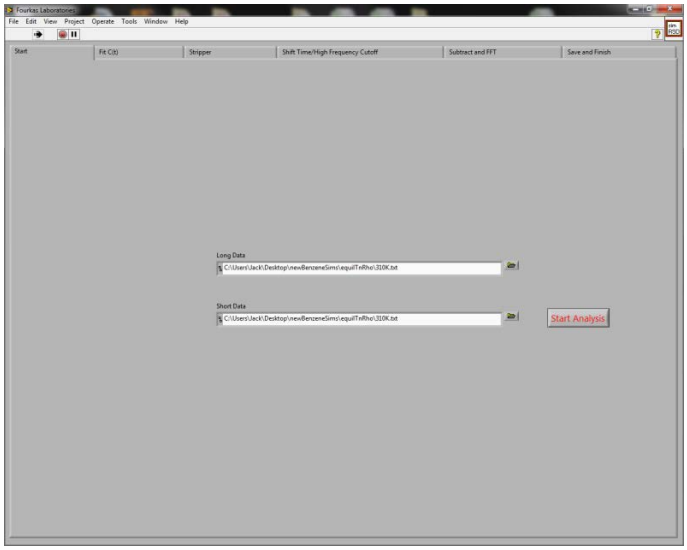

Figure A.1 Load files window of Fourier analysis software.

II. Fit TCFs to exponential function to characterize diffusive dynamics.

i. Use the cursors on the left side of the window to select the appropriate range to fit.

ii. Click “linear” button to view the semi-logarithmic plot of the function.

iii. Input initial guess parameters for fit. It helps to have an idea of the values.

iv. The user may fit the sum of up to three exponential functions and may constrain up to two of those functions. The user must input upper and lower bounds for each constrained parameter.

v. The right side of the window shows the resultant fitted region and gives the fitted parameters and either the 95% C.I. or the standard deviation, depending on the toggle. The goodness of fit parameters are also available.

vi. Click “Let’s Strip” when finished fitting.

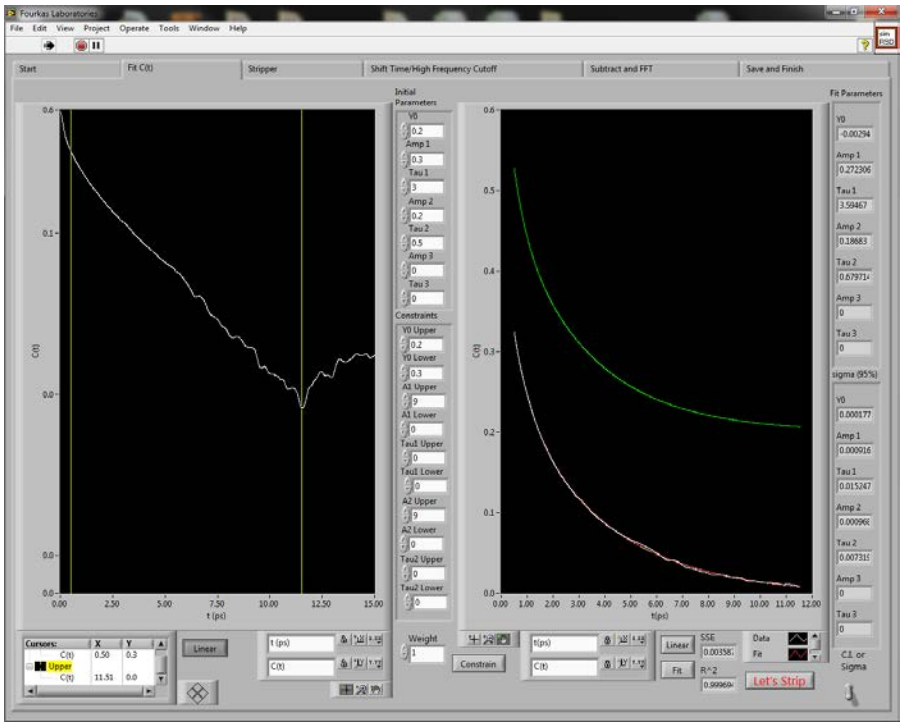

Figure A.2 Exponential fitting window to characterize diffusive dynamics.

III. Splice fitted tail onto the simulated third-order response function.

i. Use the cursor on the left side of the window to choose the appropriate splicing point for the fitted function.

ii. Adjust the gain on the right side of the window to overlap the spliced function with the simulated response function. The SSE should be minimized at the best overlap.

iii. Adjust the array size to the appropriate power of two for the transform.

iv. Choose the assumed rise time for diffusive dynamics. Usually ~200 fs.

v. Click “Let’s RSD” when the overlapping protocol is complete.

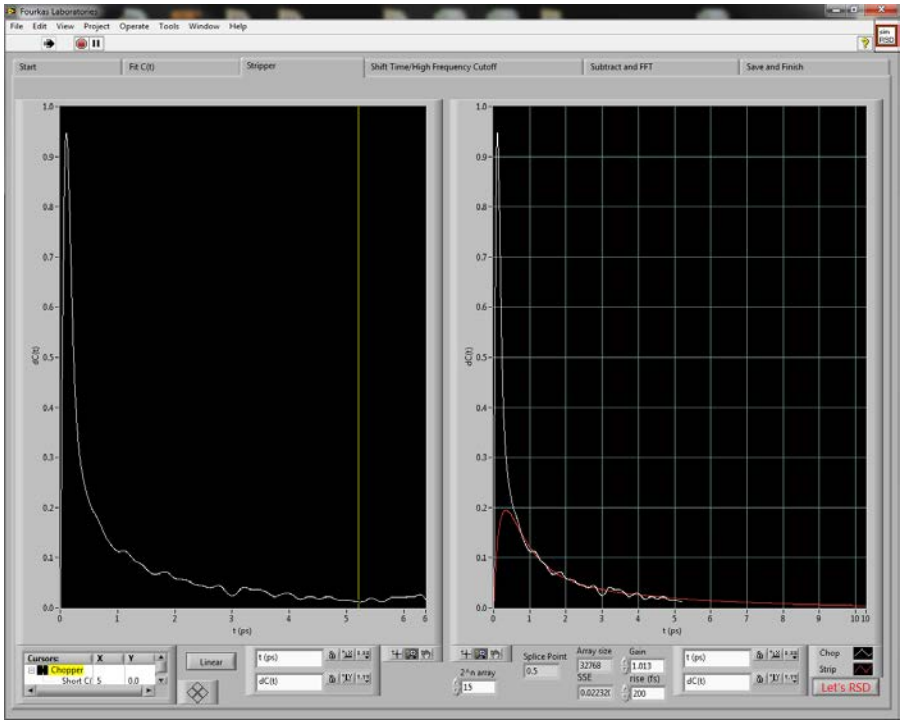

Figure A.3 Strip long-time diffusive tail onto simulated response function.

IV. Spectrally filter the spectral density.

i. Use the red cursor on the left side of the window to select the point at which to spectrally filter the high-frequency components of the Fourier transform of the nuclear response.

ii. Adjust the zero time of the nuclear response with the “Zero” numeric control. The user should not need to do this for data that has been calculated correctly.

iii. Click “Done” to go forward.

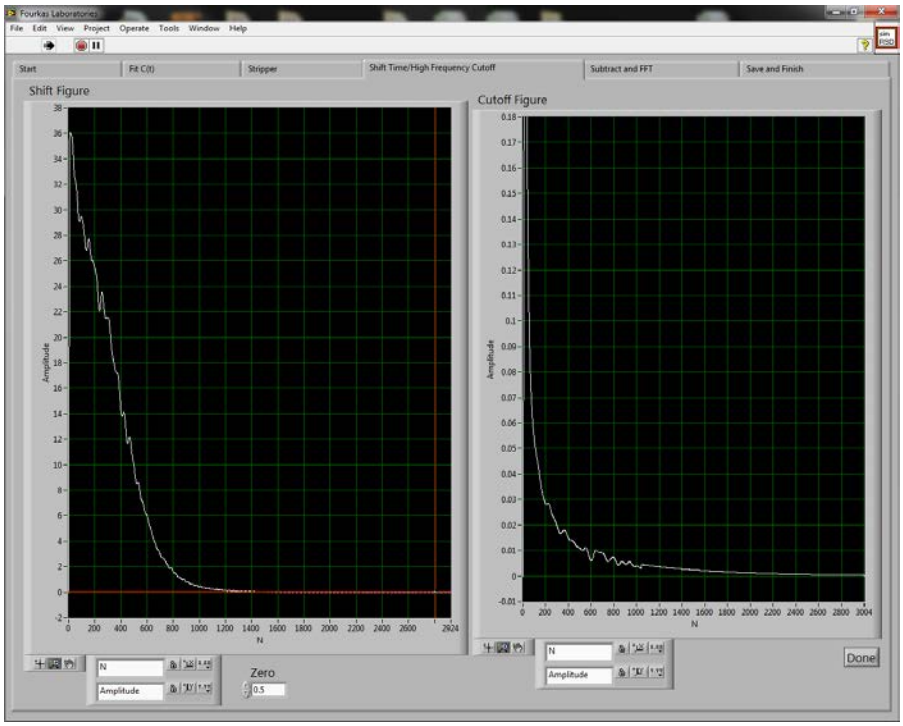

Figure A.4 Spectral density and stripped nuclear response function.

V. Subtract orientational diffusion form the nuclear response and calculate the RSD.

i. The top and bottom plots on the left side of the window show the nuclear response function with and without orientational diffusion, respectively.

ii. The exponential fit parameters for the diffusive dynamics are shown in the middle of the window.

iii. The user may engage a Savitzky-Golay filter by toggling the “Filter I/O” switch. The user may then choose the number of side points to include in the filtration and the order of the polynomial to which the side points will be fitted.

iv. The user may choose the exponential function(s) to be subtracted from the nuclear response function with the “Subtract” and “Which One?” text controls.

v. The RSD can be normalized by toggling the “Normalize” switch.

vi. When finished, click “Let’s Save” to save the transformed data.

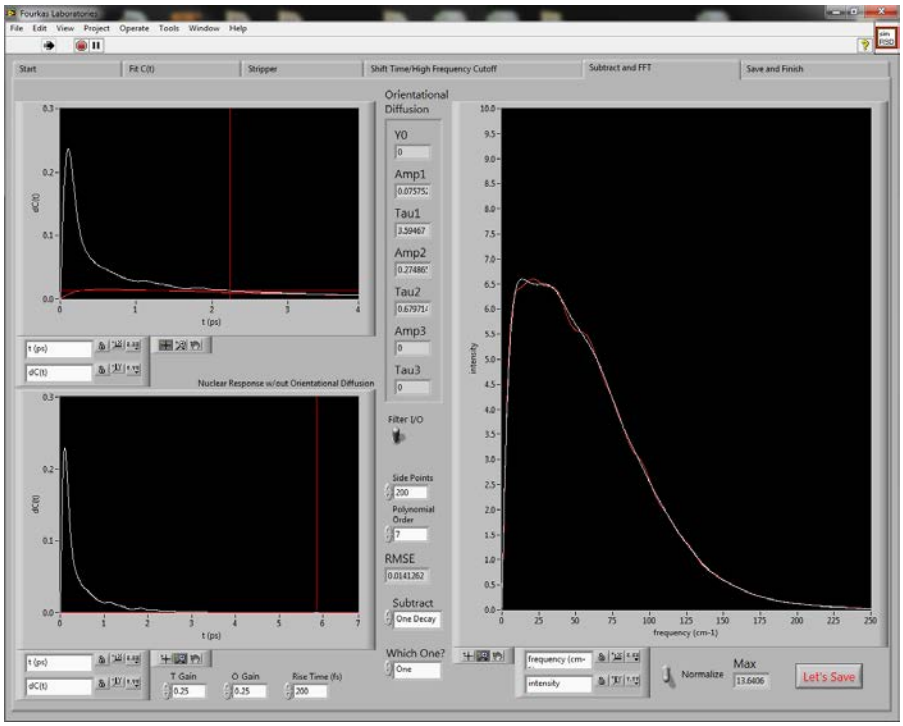

Figure A.5 Nuclear response with and without diffusive orientation and the RSD.

VI. Input date of analysis and notes for analysis.

i. The user may enter the date of analysis for record keeping.

ii. The user may enter notes on the analysis.

iii. Click “Save” to save the data to a formatted spreadsheet.

iv. Click “Done” after the data is saved.

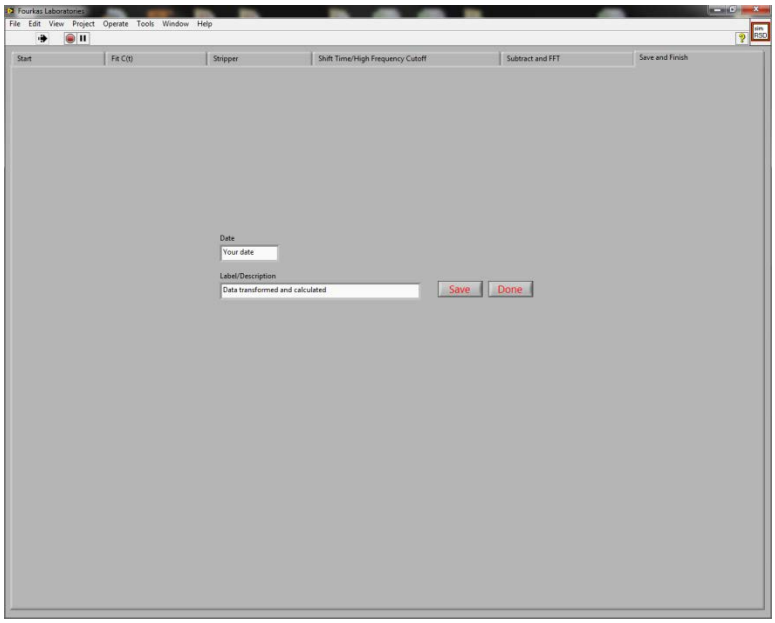

Figure A.6 Enter date and notes.

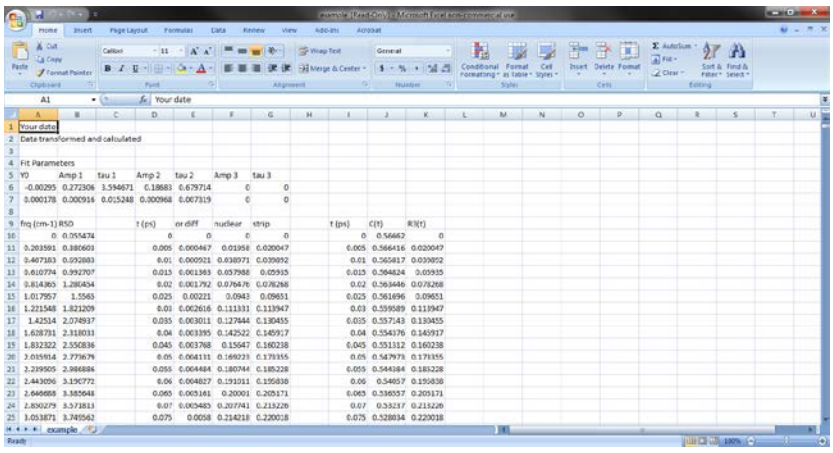

Figure A.7 Example output from Fourier analysis program.

The program allows the user to transform the many-body polarizability time correlation function into the spectral density. The user may also calculate the reduced spectral density. The output of the program is a formatted spreadsheet that contains the fitted time correlation functions and the parameters corresponding to the fits, the spectral density and the reduced spectral density.

Appendix B: LabVIEW Program for Experimental OKE Data Analysis

This LabVIEW program was written to analyze experimental OHD-OKE spectroscopy birefringence decays. The software follows the framework presented by McMorrow and Lotshaw[1,2] to remove the effects of the laser pulse from the data and to calculate the Bose-Einstein-corrected, low-frequency, depolarized Raman spectrum. There are three required input files to successfully perform these calculations: long-time-step, short-time-step, and autocorrelation curves. The long-time-step curve is the birefringence decay that is used to characterize the diffusive dynamics. The short-time-step curve is a high-time-resolution decay taken up to the point of the decay where diffusive dynamics are dominant. The autocorrelation is the laser pulse shape. Each file should be a .txt file with one column, showing the correlation function intensity. The time-step sizes for the decay curves are calculated based on user input. The autocorrelation time step is based on a 0.1 micron delay step size. It is recommended that each analysis be performed multiple times to ensure consistency. The program is not locked with a password, and as such, may be modified by the user easily. This appendix serves as a step-by-step guide to successfully use this software. The program follows the theory presented in Chapter 2, Section 2.2, Subsection 2.2.2.

I. Load Input Files.

i. Run program and click file icons to load data.

ii. Choose files for each curve.

iii. Input delay stage step-size for the long-time-step and short-time-step files.*

iv. Click “Start” to begin data analysis.

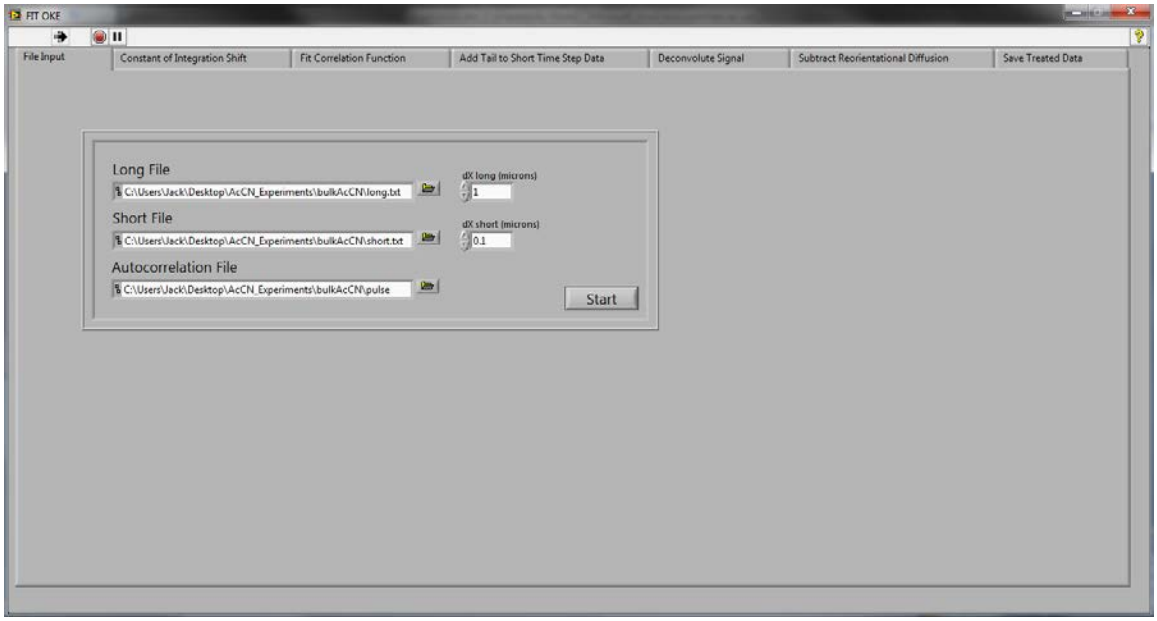

Figure B.1 Load data files for analysis.

*The time-step is calculated from the delay stage displacement.

II. Integrate and fit the long-time-step decay curve.

i. Assuming the decay has an exponential form at long times, the decay curve is integrated using Simpson's Rule. The integrated TCF is shown on the left window of Figure B.2.

ii. Use the green and red cursors to choose the appropriate range of the data to fit. Toggle the "Linear" switch to view the semi-logarithmic plot of the TCF.

iii. Choose appropriate initial guess parameters to fit.

iv. Click "Fit" to fit the curve and shift the data to baseline. The data is fit and shifted iteratively until the floating offset (Y0) is within 10^{-5}.

v. The shifted TCF is shown in the right side window of Figure B.2.

vi. Click "Fit" to move to the next step.

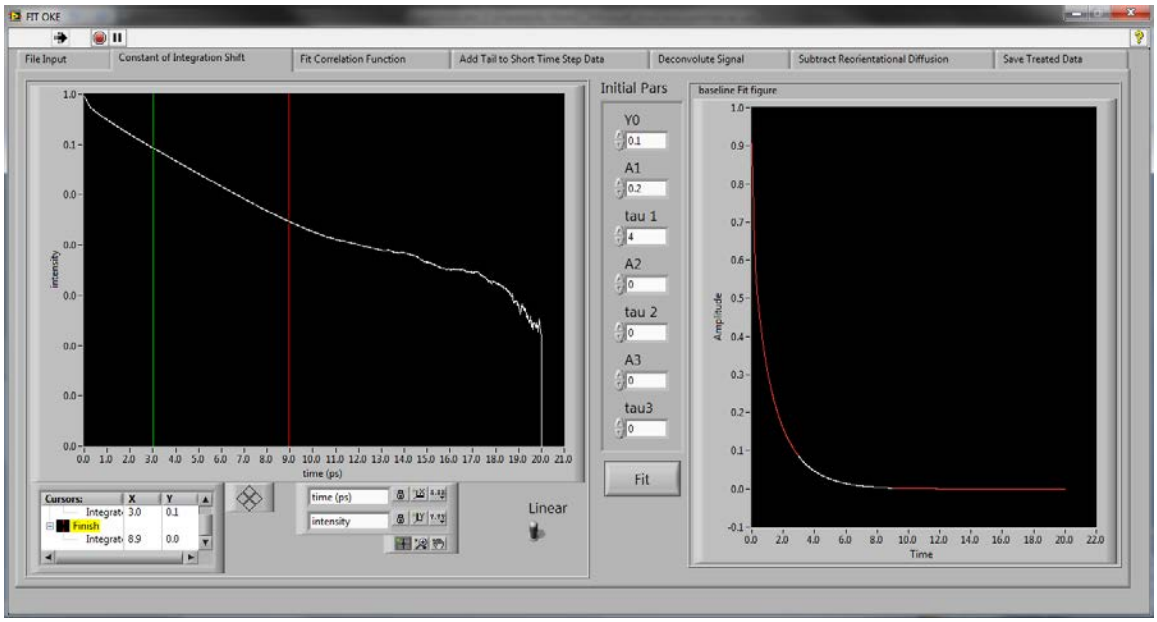

Figure B.2 Integrate and shift the long-time-step decay curve.

III. Fit the integrated and shifted long-time-step birefringence decay.

i. Use the cursors in the left window to choose the appropriate fitting range. If the user is only fitting the long-time diffusive tail, the range should be the same as the one chosen in step II.

ii. Choose the initial guess parameters for fitting. The fit is performed using the Levenberg-Marquardt nonlinear least squares algorithm. The fit is continually looped, and the fit parameters are shown in the center with the standard deviation.

iii. The fit is shown in the right-side window, and the residuals are shown in the inset. The green line is the initial guess. The red line is the fit, the green line is the initial guess, and the white line is the integrated data.

iv. Toggle the “Linear” switches to view the semi-logarithmic plots.

v. The fit can be constrained by toggling the “Constrain” switch. An upper and lower bound must be entered for each parameter.

vi. Click “Done” to move to the next step.

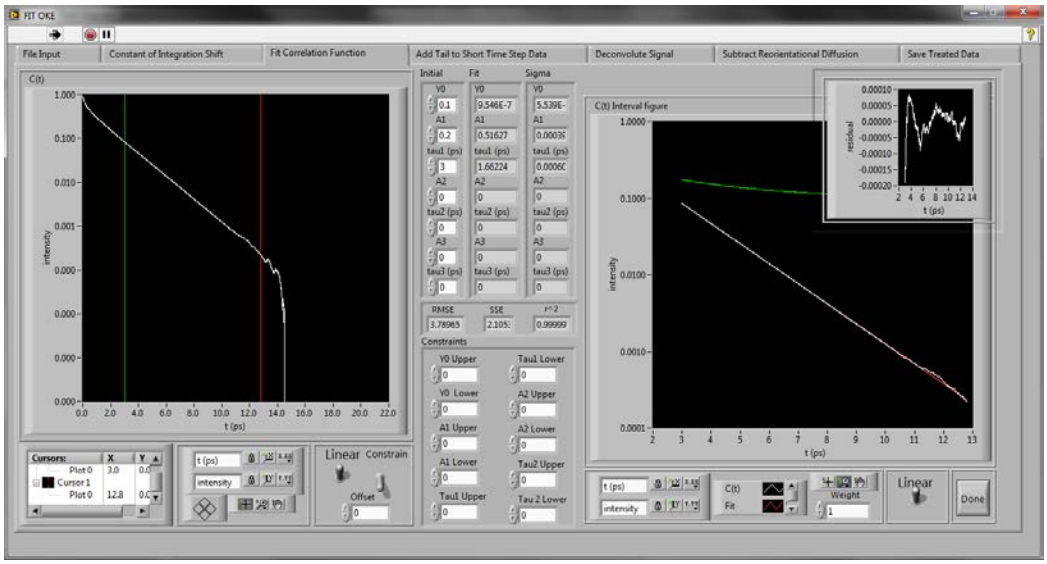

Figure B.3 Fit integrated OKE decays.

IV. Strip long-time tail onto the short-time-step decay curve.

i. The short-time birefringence decay is shown in the lift-side window of Figure B.4. Adjust the gain of the long-time tail to overlap the diffusive curve with the short-time decay. The residuals are shown in the inset.

ii. Choose the pad size. This pad size takes the decay out to $2^{\text{Pad Size}}$ number of points.

iii. The right-side window of Figure B.4 shows the birefringence decay with the pulse autocorrelation. The user can choose to scale the autocorrelation intensity.

iv. Click “Done” to move to the next step.

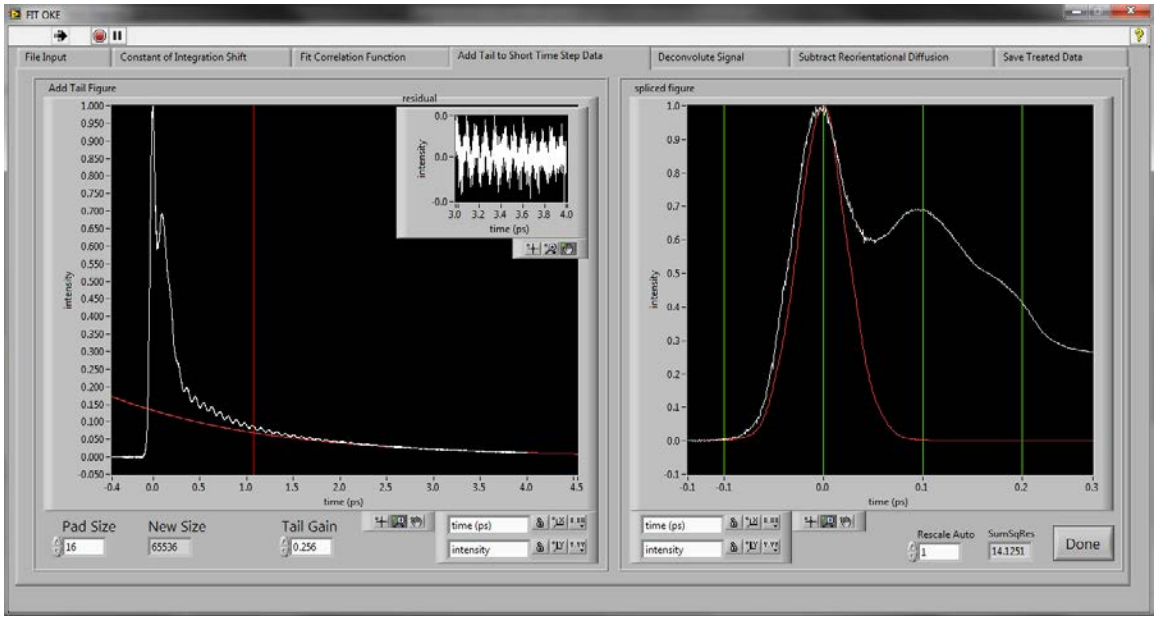

Figure B.4 Strip the long-time tail onto the short-time-step data.

V. Deconvolute the stripped decay: calculate the spectral density and the pure nuclear response.

i. The top left window of Figure B.5 shows the spectral density, which is the imaginary part of the Fourier transform of the stripped birefringence decay. Adjust the signal zero to make fine adjustments to the position of time zero in the decay. The data array can be adjusted fractionally through interpolation. Time zero is where the spectral density approaches zero intensity smoothly. Toggle the “Log” switch to view the semi-logarithmic plot. Set the red cursor to point at which the spectrum is to be spectrally filtered. After the cursor, all data is filtered.

ii. The top middle window in Figure B.5 shows the birefringence decay and the autocorrelation. The user may adjust the intensity of the autocorrelation, though this adjustment makes no mathematical changes.

iii. The top right window of Figure B.5 shows the imaginary component of the Fourier transform of the autocorrelation. Adjust the time zero of the autocorrelation until the plot is minimized. The rising edge of the autocorrelation should trace the rising edge of the birefringence decay.

iv. The bottom left window in Figure B.5 shows the extracted pure nuclear response.

v. The bottom right window in Figure B.5 shows the electronic response (blue line), the nuclear response (white line), autocorrelation (red line), and the raw data (green line). The user can adjust the overlap of the

convoluted nuclear response and the tail to overlap the long-time tail. The ratio of the amplitudes of the electronic and nuclear responses is given as Ael/Anuc.

vi. Click “No More Deconvolving” to move to the next step.

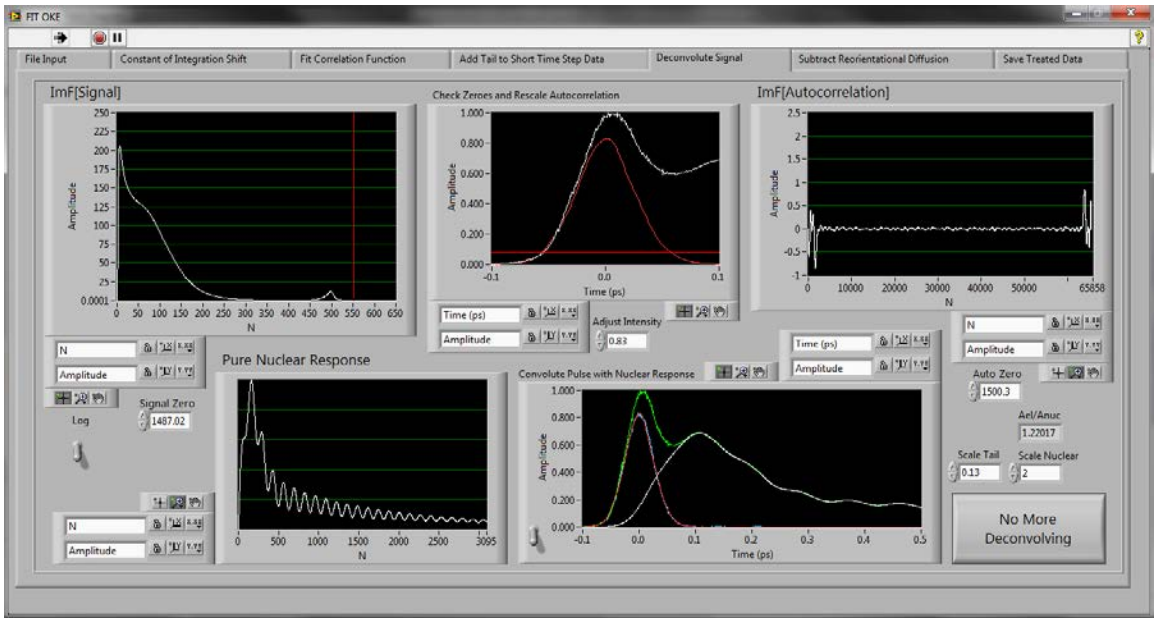

Figure B.5 Deconvolute the birefringence decay and the laser pulse.

VI. Remove orientational diffusion and calculate the RSD.

i. The left side window of Figure B.6 shows the nuclear response (white line) and the orientational diffusion curve (red line).

ii. Adjust the gain (T Gain) of the long-time tail to overlap the tail of the nuclear response with the diffusive tail.

iii. Adjust the gain (O Gain) of the orientational diffusion decay. This value should be the same as the tail gain.

iv. Adjust the rise time of the diffusive dynamics. The default value is 200 fs.

v. Choose the number of exponential decays to remove from the nuclear response by adjusting the “Subtract” control. The user may remove up to three or the number of exponential functions fit to the data, which ever number is smaller.

vi. Choose which function to remove from the nuclear response by adjusting the “Which one?” control. The functions are in the same order as the functions in III.

vii. The right side window of Figure B.6 shows the RSD. The user may normalize the data.

viii. Click “I’m completely done.” to move to the next step.

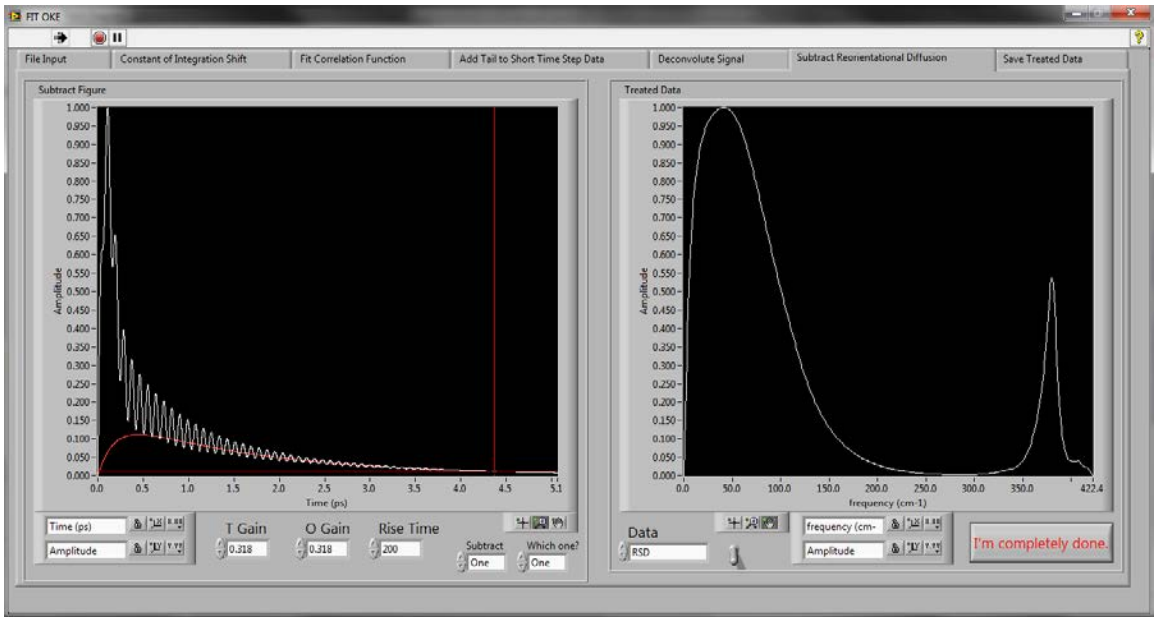

Figure B.6 The nuclear response and the RSD.

VII. Save treated data.

i. Enter date and comments for each of the files.

ii. Click “Save” to finish.

iii. Enter names of files to be saved when the dialog appears for each.

iv. The file ends running after saving the files. An example of the formatted text file of the treated data is shown in Figure B.8.

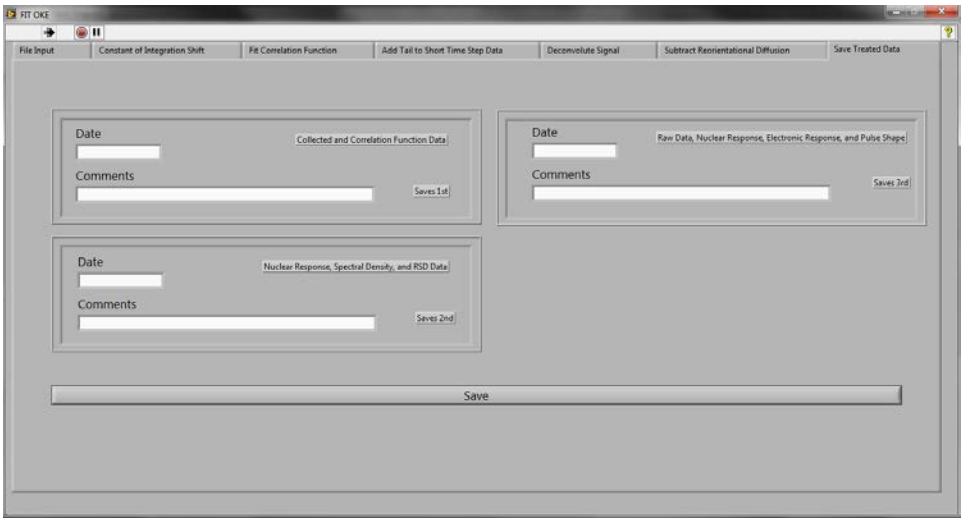

Figure B.7 Save treated Data.

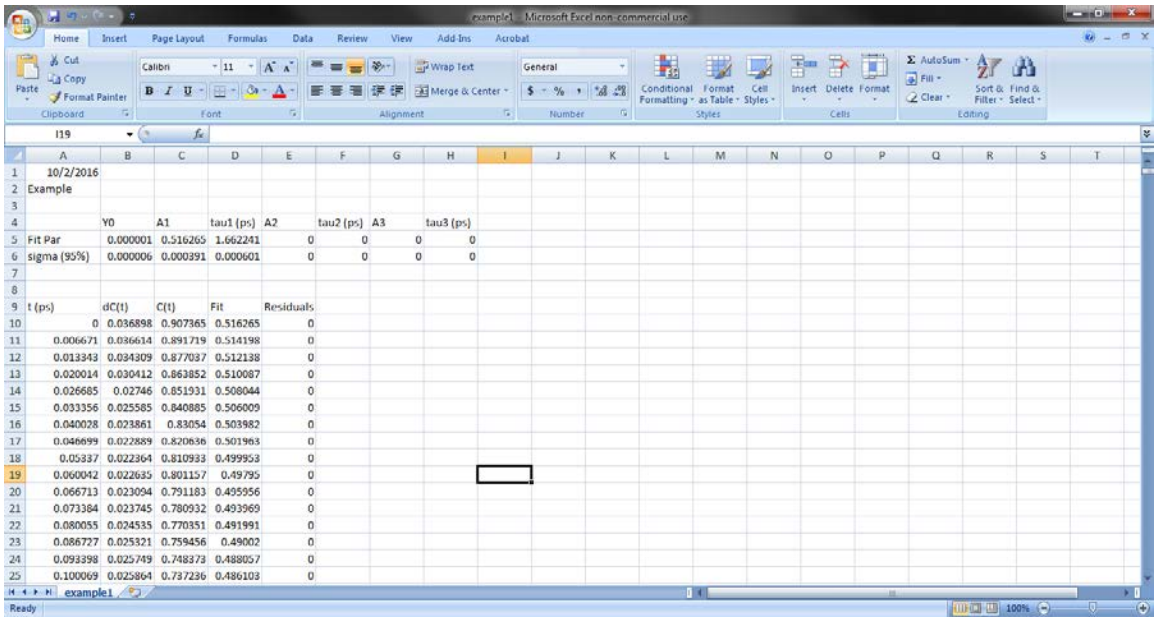

	A	B	C	D	E	F	G	H
1	10/2/2016							
2	Example							
3								
4		Y0	A1	tau1 (ps)	A2	tau2 (ps)	A3	tau3 (ps)
5	Fit Par	0.000001	0.516265	1.662241	0	0	0	0
6	sigma (95%)	0.000006	0.000391	0.000601	0	0	0	0
7								
8								
9	t (ps)	dC(t)	C(t)	Fit	Residuals			
10	0	0.036898	0.907365	0.516265	0			
11	0.006671	0.036614	0.891719	0.514198	0			
12	0.013343	0.034309	0.877037	0.512138	0			
13	0.020014	0.030412	0.863852	0.510087	0			
14	0.026685	0.02746	0.851931	0.508044	0			
15	0.033356	0.025585	0.840885	0.506009	0			
16	0.040028	0.023861	0.83054	0.503982	0			
17	0.046699	0.022889	0.820636	0.501963	0			
18	0.05337	0.022364	0.810933	0.499953	0			
19	0.060042	0.022635	0.801157	0.49795	0			
20	0.066713	0.023094	0.791183	0.495956	0			
21	0.073384	0.023745	0.780932	0.493969	0			
22	0.080055	0.024535	0.770351	0.491991	0			
23	0.086727	0.025321	0.759456	0.49002	0			
24	0.093398	0.025749	0.748373	0.488057	0			
25	0.100069	0.025864	0.737236	0.486103	0			

Figure B.8 Example output from Fourier analysis program.

This program characterizes the diffusive dynamics of OKE birefringence decays. It also removes the effects of a finite laser pulse width. The resultant exponential fits to the long-time dynamics, the spectral density, and the reduced spectral density are all saved in a formatted spreadsheet file for the user.

References

(1) McMorrow, D.; Lotshaw, W. T. Intermolecular Dynamics in Acetonitrile Probed with Femtosecond Fourier-Transform Raman-Spectroscopy. *J. Phys. Chem.* **1991**, *95*, 10395-10406.

(2) McMorrow, D.; Lotshaw, W. T. The Frequency Response of Condensed-Phase Media to Femtosecond Optical Pulses: Spectral-Filter Effects. *Chem. Phys. Lett.* **1990**, *174*, 85-94.

Bibliography

1. **Bender, J.S.**; Cohen, S.R.; He, X.; Coasne, B.; Fourkas, J.T. Optical Probing of the Density of a Confined Liquid. *In preparation*
2. **Bender, J.S.**; Cohen, S.R.; He, X.; Fourkas, J.T.; Coasne, B. Toward *in Situ* Measurement of the Liquid Density of Benzene Using Optical Kerr Effect Spectroscopy. *J. Phys. Chem. B*, **2016**, *120*, 9103-9114.
3. **Bender, J.S.**, Coasne, B., Fourkas, J.T. Assessing Polarizability Models for the Simulation of Low-Frequency Raman Spectra of Benzene *J. Phys. Chem. B*, **2015**, *119*, 9345-9358.
4. Rivera, C.A., Souna, A.J., **Bender, J.S.**, Manfred, K., Fourkas, J.T. Reorientation-Induced Spectral Diffusion in Vibrational Sum-Frequency-Generation Spectroscopy *J. Phys. Chem. B*, **2013**, *117*, 15875-15885.
5. Rivera, C.A., **Bender, J.S.**, Manfred, K., Fourkas, J.T. The Persistence of Acetonitrile Bilayers at the Interface of Acetonitrile/Water Mixtures with Silica *J. Phys. Chem. A*, **2013**, *117*, 12060-12066.
6. Ding, F., Zhong, Q., Manfred, K., He, X., **Bender, J.S.**, Brindza, M. R., Walker, R.A., Fourkas, J.T. Structure of Liquid Propionitrile at Interfaces. 2. Experiment *J. Phys. Chem. C*, **2012**, *116*, 4019-4025.